Characterizing surface wave interactions in finite superlens systems to improve imaging performance

by

Marek Jan Splawinski

B.A.S.c, The University of British Columbia, 2018

A THESIS SUBMITTED IN PARTIAL FULFILLMENT OF

THE REQUIREMENTS FOR THE DEGREE OF

MASTER OF APPLIED SCIENCE

in

THE COLLEGE OF GRADUATE STUDIES

(Electrical Engineering)

The University of British Columbia

(Okanagan)

August, 2021

The following individuals certify that they have read, and recommend to the Faculty of Graduate and Postdoctoral Studies for acceptance, the thesis entitled:

Characterizing surface wave interactions in finite superlens systems to improve imaging performance

Submitted by **Marek J. Splawinski** in partial fulfillment of the requirements for the degree of **Master of Applied Science** in **Electrical Engineering**.

Examining Committee:

Dr. Loïc Markley, School of Engineering

Supervisor

Dr. Kenneth Chau, School of Engineering

Supervisory Committee Member

Dr. Jonathan Holzman, School of Engineering

Supervisory Committee Member

Dr. Rebecca Feldman, I. K. Barber Faculty of Science

University Examiner

Abstract

High resolution lenses have numerous applications in the fields of manufacturing and imaging. Surging industrial demand for increased lensing resolution have pushed conventional imaging techniques to their performance limits. To meet this burgeoning industrial need, a comprehensive selection of super-resolution imaging technologies have been spurred into recent research and development. One of the most promising new technologies under investigation are exotic, super-resolution capable lenses known as superlenses.

Superlenses that are able to generate sub-wavelength resolution images can be realized by flat slabs of double-negative (both $\varepsilon < 0$ and $\mu < 0$) or single-negative (either $\varepsilon < 0$ or $\mu < 0$) media. These negative material slabs restore the amplitudes of fine detail carrying incident evanescent waves to push imaging resolution beyond that which can be achieved by the focusing of propagating waves alone. Amplification of incident evanescent waves through a superlens slab is delicately dependent on the off-resonant excitation of coupled surface plasmons across the slab's extent. These high surface wave amplitudes intensify minor electromagnetic interactions that are otherwise negligible in conventional imaging systems.

In this thesis, we investigate how secondary surface wave interactions introduced by finite transverse-width superlenses and complete superlensing systems can affect lensing performance. By analyzing a simple, 1-D imaging configuration, consisting of a single-negative slab centered between dielectric object and detector half-spaces, we show that inter-component reflections are not necessarily deleterious to imaging performance, but can in fact generate a secondary resonant-amplification mechanism to boost evanescent wave transmission. We then develop simulation and analysis techniques to simultaneously study both the temporal frequency and spatial frequency characteristics of dispersive, finite transverse-width superlenses. Using a full-wave simulation tool provided by COMSOL Multiphysics, we investigate the impact that transverse lens width and lens-corner curvature have on superlens transmission. We

show that the surface plasmon resonances of a finite transverse-width superlens, can be modelled using a one-dimensional cavity response, which can be tuned by modifying lens width and corner curvature radius to suppress resonant mode excitation.

Lay Summary

Light emanating from an object carries with it information about the object's physical features. To form an image, lenses are used to focus this light so that it can be detected at an imaging location. However, the light that carries finer detail information decays to nothing as it travels away from the object. Special lenses known as superlenses seek to amplify this fine-detail carrying light to compensate for its decay. This amplification occurs when light bouncing back and forth within the lens adds together. In our research, we investigate how the light bouncing back and forth within a superlens can interact with both the lens geometry and nearby imaging components. We show that reflections between the object and superlens can also add together and cause amplification, and how changing superlens geometry can be used to modify the lens' amplification characteristics.

Preface

This work has been carried out under the supervision of Dr. Loïc Markley at the School of Engineering in The University of British Columbia. The third chapter of this thesis contains work that has been presented in the publication:

- "Superlens coupling to object and image: A secondary resonance mechanism to improve single-negative imaging of electromagnetic waves." *Journal of Applied Physics* 129.16 (2021): 163102.

and submitted to the conference:

- "Improving single-negative superlensing through object-lens resonance." *2021 IEEE International Symposium on Antennas and Propagation and North American Radio Science Meeting.* IEEE, 2021.

The fourth chapter of this thesis contains work that has been presented at the following conference:

- "Coupled Surface Mode Resonances in Finite Transverse-Width Superlenses." *2020 IEEE International Symposium on Antennas and Propagation and North American Radio Science Meeting.* IEEE, 2020.

Table of Contents

Abstract iii

Lay Summary v

Preface vi

Table of Contents vii

List of Figures ix

List of Acronyms xiv

List of Symbols xv

Acknowledgements xvi

1 Introduction 1
- 1.1 Progression of Imaging 1
- 1.2 Superlensing 3
  - 1.2.1 Focusing Mechanism 4
  - 1.2.2 Evanescent Wave Amplification 4
  - 1.2.3 Imperfect Superlenses 6
- 1.3 Motivation and Goals 7
- 1.4 Organization of this Thesis 8

2 Background 10
- 2.1 Fourier Imaging 10
- 2.2 Negative Material Properties 12
- 2.3 Surface Plasmon Dispersion 13
- 2.4 Surface Plasmons Around a Bend 19

3 Optical Component Interactions 21
- 3.1 Imaging Model 22
- 3.2 Signal Flow 23
- 3.3 Planar Multi-system Analysis 25
- 3.4 Spectral Transmission Comparison 27
- 3.5 External Resonance Investigation 31
- 3.6 Spectral Transmission Comparison Revisited 34
- 3.7 Amplification Comparison 37
- 3.8 Imaging Analysis Results 39

4 Finite Lens Effects 47
4.1 Simulation Model 48
4.1.1 Addressing Evanescent Wave Simulation Challenges 50
4.2 Evaluating Finite Width Superlens Spectral Transmission 50
4.2.1 Simulation and Processing Methods 50
4.2.2 Double-Drude Transmission Response 54
4.2.3 Double-Drude Transmission Performance 59
4.2.4 Single-Drude Lens Geometric Tuning 60
4.3 Finite Width Lens Radiated Power Analysis 66
4.3.1 Radiated Power Methods 66
4.3.2 Radiated Power Response 67

5 Conclusion 72
5.1 Summary of Evanescent Wave Simulation Guidelines 72
5.2 Summary of Research 73
5.3 Future Work 75

Bibliography 77

List of Figures and Illustrations

1.1 Sample ray tracing diagram for a conventional lens. 2

1.2 Diagram of near-field scanning optical microscopy (NSOM). Incident light passes through an aperture to selectively illuminate the object. The object to be imaged is shown here as the blue circle, while a neighbouring object is shown as the red circle. Both the aperture diameter (δ) and operating distance (z) have subwavelength ($< \lambda$) dimensionality. 3

1.3 Sample ray tracing diagram for a Veselago lens. 5

2.1 Calculated field transmission coefficient plots (left) and iso-frequency cut-lines (right) showing resonant intersections and resulting transmission cuts for operation at (a) $\omega_{\rm n} = 1$, (b) $\omega_{\rm n} = 0.96$ and (c) $\omega_{\rm n} = 1.25$. All calculations are for a double-Drude slab superlens of thickness $\lambda_{\rm p}/2\pi$. Note normalized axes $\omega_{\rm n} = \omega/\omega_{\rm op}$ and $\beta_n = \beta/k_{\rm op}$ where $\omega_{\rm op} = \omega_{\rm p}/\sqrt{2}$, and $k_{\rm op} = \omega_{\rm op}/c$. Overlaid red curves indicate the analytic surface plasmon dispersion relations for the resonance condition. 15

2.2 The superposition of off-resonance excited upper (ω^+) and lower (ω^-) surface plasmon branches of a perfect lens ($n = -1$) generates a unity overall transmission response. 16

2.3 Calculated field transmission coefficient plots (left) and iso-frequency cut-lines (right) showing resonant intersections and resulting transmission cuts for operation at (a) $\omega_{\rm n} = 1$, (b) $\omega_{\rm n} = 0.96$ and (c) $\omega_{\rm n} = 1.25$. All calculations are for a single-Drude slab superlens of thickness $\lambda_{\rm p}/2\pi$. Note normalized axes $\omega_{\rm n} = \omega/\omega_{\rm op}$ and $\beta_n = \beta/k_{\rm op}$ where $\omega_{\rm op} = \omega_{\rm p}/\sqrt{2}$, and $k_{\rm op} = \omega_{\rm op}/c$. Overlaid red curves indicate the analytic surface plasmon dispersion relations for the resonance condition. 17

2.4 A diagram of a superlens with a finite thickness d, finite width w, infinite length and circularly curved corners. Wavy arrows illustrate the surface plasmon reflection (E_r, purple), transmission (E_t, green) and free-space coupling (E_c, red) that may occur when an incident surface plasmon (E_i, blue) traverses a lens corner. 20

3.1 A one dimensional model of a superlens-based imaging system. A superlens slab of thickness d is embedded within a dielectric imaging system having dielectric object and detector half-spaces, both of which are defined by a refractive index of $n = 4$, and are separated by a distance D. The black curve sketches the field envelope of a sample wave component with transverse wave number $k_0 \leq \beta \leq nk_0$ transmitted through an SNG superlens. © 23

3.2 Signal flow graph for (a) an isolated superlens and (b) a superlens embedded between dielectric object and detector regions. The symbols t_0 and r_0 represent the field transmission and reflection coefficients of the bare lens while t and r represent the field transmission and reflection coefficients of the complete system. The Fresnel reflection coefficient at the dielectric interface from free-space is given by ρ. 25
3.3 Diagram of an $(M+1)$-layer imaging system showing the interface locations and properties of each region. 26
3.4 Field Transmission (dB) of wave components $\beta = 0.5k_0$, $\beta = 1.5k_0$, and $\beta = 3k_0$ through (a) an SNG lens placed in free-space, (b) an ENG lens placed between dielectric object and image regions, and (c) an MNG lens placed between dielectric object and image regions. Transmission is plotted as a function of relative lens thickness d/D and total imaging distance D. The overlaid white line indicates the slab resonance thickness of equation (3.14). 28
3.5 A one dimensional model of the three-layer free-space resonance geometry. A dielectric half-space is separated from an SNG half-space by a free-space gap of length δ. The black curve sketches a sample field envelope for a wave component with transverse wave vector $k_0 \leq \beta \leq nk_0$ 31
3.6 Transmission (dB) of wave components $\beta = 0.5k_0$, $\beta = 1.5k_0$, and $\beta = 3k_0$ through (a) an SNG lens placed in free-space, (b) an ENG lens placed between dielectric object and image regions, and (c) an MNG lens placed between dielectric object and image regions. Transmission is plotted as a function of relative lens thickness d/D and total imaging distance D. The overlaid white and grey lines indicate the slab resonance thickness of (3.14) and free-space gap resonance of (3.20), respectively. 36
3.7 Transmission of a $\beta_n = 3k_0$ spectral component through a dielectric-embedded ENG lens (left) and dielectric-embedded MNG lens (right). Red markers indicate the imaging distances and lens thicknesses for which field cross-sections through the lensing system are plotted in Fig. 3.8. 37
3.8 Normalized electric and magnetic field magnitude cross-section plots through the five-layer ENG and MNG configurations for spectral component $\beta = 3k_0$. Plots (a) and (c) show ENG and MNG configuration field cross-sections at a sample imaging distance of $D = 0.6\lambda$ and lens thickness of $d/D = 0.2422$ ($d = 0.1453\lambda$). This imaging configuration is chosen to satisfy the resonance condition in (3.14) for an isolated slab in free-space. Plots (b) and (d) show ENG and MNG configuration field cross-sections at a sample imaging distance of $D = 0.32\lambda$ and lens thickness of $d/D = 0.4925$ ($\delta = 0.0812\lambda$). This imaging configuration is chosen to satisfy the resonance condition in (3.20) for the air-gap between the dielectric and SNG lens in a three-layer system. Regions are distinguished by color: dark blue indicates the dielectric regions, light blue the ENG lens, and light red the MNG lens. Each lens configuration in this figure is marked with a red cross on the Fig. 3.6 surface plots. 38

3.9 (The (top) mean and (bottom) normalized standard deviation (stdev) of transmission calculated over $-4k_0 \leq \beta \leq 4k_0$ for (a) the ENG lensing system and (b) the MNG lensing system. The red marker indicates the lens thickness for peak imaging performance at an imaging distance of $D = 0.3\lambda$. This corresponds to a lens thickness of $d = 0.4102D$ for the ENG lens and $d = 0.4202D$ for the MNG lens. 41
3.10 Transmission through an MNG lens ($\mu = -1$) placed between two dielectric regions ($n = 4$) separated by 0.3λ. The real part of the transmission coefficient is plotted as a function of slab thickness and transverse wave vector. The transmission magnitude and phase corresponding to the lens thickness $d/D = 0.421$ (indicated by the dashed white line) is plotted in the cross-sections below. . . . 42
3.11 a) Two point sources with quarter wavelength separation imaged through b) an isolated ENG lens, c) an ENG lens placed between two dielectric half-spaces ($n = 4$), and d) an MNG lens placed between two dielectric half-spaces ($n = 4$). In all three cases the imaging distance is 0.3λ and the lens thickness is optimized to provide the flattest spectral transfer function. 43
3.12 The imaging response of the single-negative lensing systems under conditions of increasing loss. a) Three point sources with an adjacent separation distance of 0.25λ imaged through b) an isolated ENG lens, c) an ENG lens placed between two dielectric half-spaces ($n = 4$) , and d) an MNG lens placed between two dielectric half-spaces ($n = 4$). For each lensing configuration the object and image are separated by a distance of 0.3λ. The imaging response is shown for loss tangents of 0, 0.05, 0.10, and 0.15. 45

4.1 Simulation model of a curved corner, finite transverse width superlens within a free-space simulation region. Perfectly matched layers of width $\lambda_p = \lambda_{op}/\sqrt{2}$ bound the simulation space to absorb scattered radiation. The lens has a width w, thickness d, corner radius r. The object plane is shown as a vertical dashed line that is located at $x = -d$, and the image plane is a vertical, dotted line that is located at $x = d$. A sample scattered field is overlaid as a red and blue surface pattern. 49
4.2 **Top row:** Sample simulation plots of the real (red) and imaginary (blue) components of (a) the transmitted electric field measured at the image plane and (b) an approximation of the transmitted electric field measured at the image plane. **Bottom row:** Sample amplitude spectrum of (c) the simulated electric field as measured at the image plane, and (d) an approximation of the four main spectral peaks of the simulated spectrum. All plots are for a single-Drude lens with a thickness of $d = \lambda_{op}/(2\sqrt{2}\pi)) \approx 0.11\lambda_{op}$, corner radius of $r = 0.45d \approx 0.051\lambda_{op}$. Vertical dashed lines indicate the locations of free-space cut off spatial frequencies $\pm k_0$, as well as the incident spectral component spatial frequency $+\beta_{ni}$ and the negative incident spectral component spatial frequency $-\beta_{ni}$. 52

4.3 Plots in dB of the transmission of spectral components **(a)** $+\beta_{ni}$, **(b)** $-\beta_{ni}$, **(c)** $+k_0$ and **(d)** $-k_0$ through a sample double-Drude lens ($\omega_{p\varepsilon} = \omega_{p\mu}$) with a thickness of $d = \lambda_{op}/(2\sqrt{2}\pi) \approx 0.11\lambda_{op}$, corner radius of $r = 0.45d \approx 0.051\lambda_{op}$, and width of $w = 3\lambda_{op}/\sqrt{2} \approx 2.12\lambda_{op}$. The overlaid black curves present the resonant surface plasmon solutions for an infinitely wide superlens. 55

4.4 Plots in dB of the spectral transmission, $\log(|T_i|)$, through double-Drude lenses ($\omega_{p\varepsilon} = \omega_{p\mu}$) with a thickness of $d = \lambda_{op}/(2\sqrt{2}\pi) \approx 0.11\lambda_{op}$, corner radius of $0.45d \approx 0.051\lambda_{op}$, and a) a width of $w = 3\lambda_{op} \approx 2.12\lambda_{op}$, b) a width of $w = 5\lambda_{op} \approx 3.53\lambda_{op}$. Spectral transmission is calculated using the methods described in Sec. 3.5 over temporal frequency ($\omega_n = \omega/\omega_{op}$) and transverse spatial frequency ($\beta_n = \beta/\beta_{op}$). The overlaid black curves present the resonant surface plasmon solutions for an infinitely wide superlens, while the black and white markers locate the maxima and minima, respectively, of a one-dimensional cavity with a length matching that of the lens width. 56

4.5 Plot in dB of the spectral transmission, $\log(|T_i|)$ of double-Drude lenses ($\omega_{p\varepsilon} = \omega_{p\mu}$) with a thickness of $d = \lambda_{op}/(2\sqrt{2}\pi)$, width of $w = 5\sqrt{2}\lambda_{op} \approx 3.53\lambda_{op}$ and (a) a corner radius of $0.45d \approx 0.051\lambda_{op}$, (b) a corner radius of $0.15d \approx 0.017\lambda_{op}$. Spectral transmission is calculated using the methods described in Sec. 3.5 over both temporal frequency and transverse spatial frequency. The overlaid black curves present the resonant surface plasmon solutions for an infinitely wide superlens, while the black and white markers locate the maxima and minima, respectively, of a one-dimensional cavity matching the lens width. 58

4.6 Spectral electric field transmission, $\log(|T_i|)$ (dB) along the ω_{op} matched frequency for the indicated double-Drude lens geometries. All lenses have thickness of $d = \lambda_{op}/(2\sqrt{2}\pi) \approx 0.11\lambda_{op}$ and differ only by width and corner curvature radius. 60

4.7 Electric field spectral transmission, $\log(|T_i|)$ (dB) along the ω_{op} matched frequency for the indicated double-Drude lens geometries. All lenses have thickness of $d = \lambda_{op}/(2\sqrt{2}\pi) \approx 0.11\lambda_{op}$ and differ only by width and corner curvature radius. 61

4.8 Spectral transmission plots, $\log(|T_i|)$ (dB) for $d = \lambda_{op}/(2\sqrt{2}\pi) \approx 0.11\lambda_{op}$, $w = 3\sqrt{2}\lambda_{op} \approx 2.12\lambda_{op}$ single-Drude lenses with radii of (a) $r = 0.50d \approx 0.056\lambda_{op}$, (b)$r = 0.45d \approx 0.051\lambda_{op}$, (c) $r = 0.40d \approx 0.045\lambda_{op}$, (d) $r = 0.35d \approx 0.039\lambda_{op}$. 63

4.9 Spectral transmission plots (dB) for $d = \lambda_{op}/(2\sqrt{2}\pi) \approx 0.11\lambda_{op}$ single-Drude lenses with (a) a width of $w = 5\sqrt{2}\lambda_{op} \approx 3.53\lambda_{op}$ and corner curvature of $r = 0.15d \approx 0.017\lambda_{op}$, (c) a width of $w = 5\sqrt{2}\lambda_{op} \approx 3.53\lambda_{op}$ and corner curvature of $r = 0.45d \approx 0.051\lambda_{op}$, and (d) a width of $w = 3\sqrt{2}\lambda_{op} \approx 2.12\lambda_{op}$ and corner curvature of $r = 0.45d \approx 0.051\lambda_{op}$. The chosen operating frequency of $\omega_n = 0.974$ is plotted as an overlaid, dashed horizontal line. Spectral transmission along the operating frequency is plotted in (b) for the $w = 5\sqrt{2}\lambda_{op} \approx 3.53\lambda_{op}$, $r = 0.15d \approx 0.017\lambda_{op}$, (d) for the $w = 5\sqrt{2}\lambda_{op} \approx 3.53\lambda_{op}$, $r = 0.45d \approx 0.051\lambda_{op}$ lens, and (f) for the $w = 3\sqrt{2}\lambda_{op} \approx 2.12\lambda_{op}$, $r = 0.45d \approx 0.051\lambda_{op}$ lens. 65

4.10 Finite width lens simulation model showing the fictitious lens-enclosing line (dashed) over which the scattered-field Poynting vector is integrated in order to calculate the power radiated by the lens. 67
4.11 Side by side comparison of the spectral transmission, $\log(|T_i|)$ (dB, left) and radiated power, $\log(|P_{rad}|)$ (dB, right) of finite width, $d = \lambda_{op}/(2\sqrt{2}\pi) \approx 0.11\lambda_{op}$ thick matched double-Drude lenses ($\varepsilon_p = \mu_p$). Three separate lens widths and corner curvature radii combinations are considered: a) $w = 3\sqrt{2}\lambda_{op} \approx 2.12\lambda_{op}$, $r = 0.45d \approx 0.051\lambda_{op}$, b)$w = 5\sqrt{2}\lambda_{op} \approx 3.53\lambda_{op}$, $r = 0.45d \approx 0.051\lambda_{op}$ and c) $w = 5\sqrt{2}\lambda_{op} \approx 3.53\lambda_{op}$, $r = 0.15d \approx 0.017$ 68
4.12 Side by side comparison of the spectral transmission, $\log(|T_i|)$ (dB, left) and radiated power, $\log(|P_{rad}|)$ (dB, right) of finite width, $d = \lambda_{op}/(2\sqrt{2}\pi) \approx 0.11\lambda_{op}$, $w = 3\sqrt{2}\lambda_{op} \approx 2.12\lambda_{op}$ single-Drude superlenses. From top to bottom results are plotted for corner radii of (a) $r = 0.45d \approx 0.051\lambda_{op}$, (b) $r = 0.40d \approx 0.045\lambda_{op}$, (c)$r = 0.35d \approx 0.039\lambda_{op}$. 70
4.13 Side by side comparison of positive free-space cut-off transmission, $\log(|T_{k0}|)$ (dB, left) and radiated power, $\log(|P_{rad}|)$ (dB, right) of finite width, $d = \lambda_{op}/(2\sqrt{2}\pi) \approx 0.11\lambda_{op}$, $w = 3\sqrt{2}\lambda_{op} \approx 2.12\lambda_{op}$, $r = 0.45d \approx 0.051\lambda_{op}$ double-Drude superlenses. 71

List of Acronyms

Acronym	Definition
DNG	Double Negative
ENG	ε-Negative
FDTD	Finite-Difference Time-Domain
FEM	Finite Element Method
FFT	Fast Fourier Transform
FWHM	Full-Width Half-Maximum
MNG	μ-Negative
NSOM	Near-Field Scanning Optical Microscopy
PML	Perfectly Matched Layer
SNG	Single Negative

List of Symbols

Symbol	Definition
β	Transverse Spatial Frequency
β_n	Normalized Transverse Spatial Frequency
ε	Permittivity
ε_{r}	Relative Permittivity
λ_{op}	Operating Wavelength
λ_p	Plasma Wavelength
μ	Permeability
μ_{r}	Relative Permeability
ω	Angular Temporal Frequency
ω_n	Normalized Angular Temporal Frequency
ω_{op}	Operating Angular Temporal Frequency
ω_{p}	Plasma Angular Temporal Frequency
c	Speed of Light in Vacuum
j	Imaginary Unit
k_0	Free-Space Wavenumber
k_{op}	Operating Wavenumber
k_x	Longitudinal Spatial Frequency
n	Refractive Index

Acknowledgements

First, I would like to thank my supervisor, Dr. Loïc Markley. I am immensely grateful for the many hours that you have spent guiding my research, explaining difficult concepts, troubleshooting simulations, and editing my flailing attempts at writing. I hope to one day emulate your standard of work, and count myself extremely lucky to have had you as both a teacher and a supervisor.

I would also like to thank my academic committee members, Dr. Kenneth Chau and Dr. Jonathan Holzman. Thank you for all the assistance and advice that you provided me with over these past years. UBCO has an incredible electromagnetics faculty, and it is your contagious enthusiasm for the subject that made me choose my major.

Finally, I would like to thank my parents. To my father, Mr. Dr. Jan Splawinski; thank you for supporting me throughout my education, and for your boundless confidence in me. Your strong belief in the benefits of pursuing a higher education is what convinced me to pursue this Master's degree. And to my mother, Joan Croft, who has fed me nearly every day of life; were you a fan of praise I would fill a page for you here, but I will spare you that melodrama. Thank you so much for all that you do for me.

Chapter 1

Introduction

"...And on the pedestal, these words appear:

My name is Ozymandias, King of Kings;

Look on my Works, ye Mighty, and despair!...

– Percy Bysshe Shelley

1.1 Progression of Imaging

Lenses are passive electromagnetic devices whose material parameters and geometry are designed to image a radiative source by recreating its electromagnetic field distribution at an observation plane. In its most basic form, a conventional lens comprises a solid piece of transparent, curved material with a refractive index that is greater than the surrounding medium. Lens characteristics are designed to redirect incident light to compensate for natural radiative divergence from a source. The focusing of a source distribution, illustrated in the Fig. 1.1 ray diagram, restores the relative phase of each wave-front at the observation plane to form an image.

The first glass lenses appeared in the 11^{th} century and were primarily used for applications such as fire starting and object magnification [1]. By the 13^{th} century Italian lens-makers were designing spectacles for vision correction [2]. This progressive improvement of lens design soon led to microscopic imaging in the 16^{th} century, where early optical microscopy was able to yield over 200% magnification, enabling the observation of single cell organisms including bacteria and erythrocytes [1]

The imaging resolution of optical microscopy was however soon shown to have its limi-

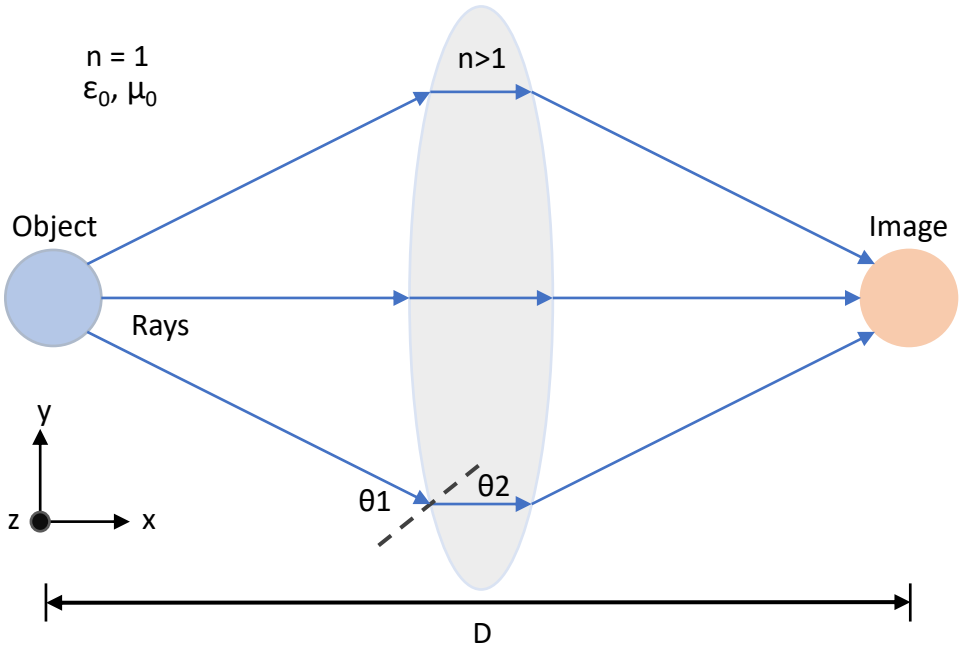

Figure 1.1: Sample ray tracing diagram for a conventional lens.

tations. In 1835, George Biddell Airy found that when light passes through the aperture of a lens it is diffracted, creating a blurry pattern known as the 'Airy disc' [3]. This image-field blurring would later be shown by Ernst Abbe to limit the minimum resolvable object feature size to approximately half the wavelength of incident light. A landmark discovery of the time, Abbe's diffraction limit designated that higher imaging resolution could only be achieved by increasing operation frequency [4].

Abbe's work on the diffraction limit was so influential and widespread that for years following its publication there were few attempts to surpass it. It was not until 1928 that Physicist Edward Hutchinson Synge suggested that observation through a subwavelength aperture could enable so called super-resolution imaging [5]. In Synge's seminal work, he set the theoretical framework for what would later become known as near-field scanning optical microscopy (NSOM) [6]. Synge proposed that sub-diffractive imaging by could be achieved by using a small aperture as a subwavelength window to selectively illuminate the finer features of an object (Fig. 1.2). By constraining the field of view to a subwavelength region, interference from

neighbouring object features that would otherwise obscure the finer detail information could be effectively blocked from detection. Scanning such an aperture over the extent of an object would then allow for a complete image with resolution surpassing the diffraction limit to be formed.

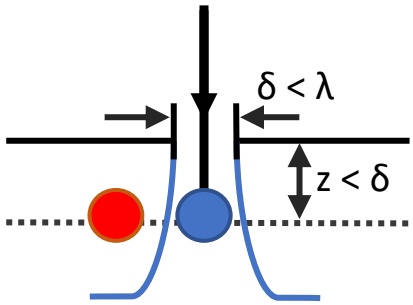

Figure 1.2: Diagram of near-field scanning optical microscopy (NSOM). Incident light passes through an aperture to selectively illuminate the object. The object to be imaged is shown here as the blue circle, while a neighbouring object is shown as the red circle. Both the aperture diameter (δ) and operating distance (z) have subwavelength ($< \lambda$) dimensionality.

1.2 Superlensing

The super-resolution imaging capabilities of NSOM rely on the detection of fine-detail carrying near-field waves. When incident light passes through a subwavelength aperture, the resulting diffraction generates near-field, or evanescent waves. These evanescent waves have the ability to carry subwavelength object feature information, but undergo exponential amplitude decay as they travel away from their source (*i.e.* the aperture). The detection of evanescent waves enables subwavelength resolution imaging. However, as evanescent waves are localized to only a short distance surrounding the aperture, near-field placement of both the object and image detector is required. Still, even when operated within this extreme near-field region ($\lambda < 10$), the rapid decay of evanescent waves makes can make them difficult to impossible to detect [7, 8].

Fortunately, evanescent wave detection can be greatly improved using recently developed

superlens technology. Superlenses are lenses that are capable of generating super-resolution images by boosting the amplitudes of incident evanescent waves to compensate for their natural free-space decay. This superlensing phenomenon was first demonstrated by J. B. Pendry in 2000 [9]. Pendry showed that when a flat slab of double-negative (DNG) medium with both $\varepsilon_r = -1$ and $\mu_r = -1$ is immersed in free-space, and placed between an object and detector that are in turn separated by a distance equal to twice that of the lens thickness, a perfect image with infinite resolution is achieved. Operated in this specific configuration, Pendry's perfect lens is able to both focus all incident propagating waves, and restore the amplitudes of all incident evanescent waves, to generate an exact replica of the source distribution at the imaging location.

1.2.1 Focusing Mechanism

The focusing capabilities of a flat DNG slab were first theoretically demonstrated by Victor Veselago in 1968 [10]. Simultaneous negative ε and μ results in a negative refractive index, $n = -\sqrt{\varepsilon_r \mu_r}$. Light rays incident to an interface separating positive and negative refractive index media are refracted to the opposite side of the interface normal at an angle dictated by Snell's law, $n_1 \sin(\theta_1) = n_2 \sin(\theta_2)$. This exotic property of negative refraction enables flat slab focusing. Consider the DNG slab superlens shown in Fig. 1.3. Light incident onto the first slab interface undergoes negative refraction and is bent towards the optical axis. These rays then converge within the lens, creating an internal focal spot before reaching the second interface. At the second interface, the rays again undergo negative refraction, and are redirected to form another focal spot, now outside the lens at the imaging location.

1.2.2 Evanescent Wave Amplification

The focusing of propagating waves alone does not make a superlens. Distinguishing subwavelength object features requires the detection of fine detail carrying evanescent waves. J. B. Pendry's discovery that the Veselago lens could not only focus propagating waves, but also

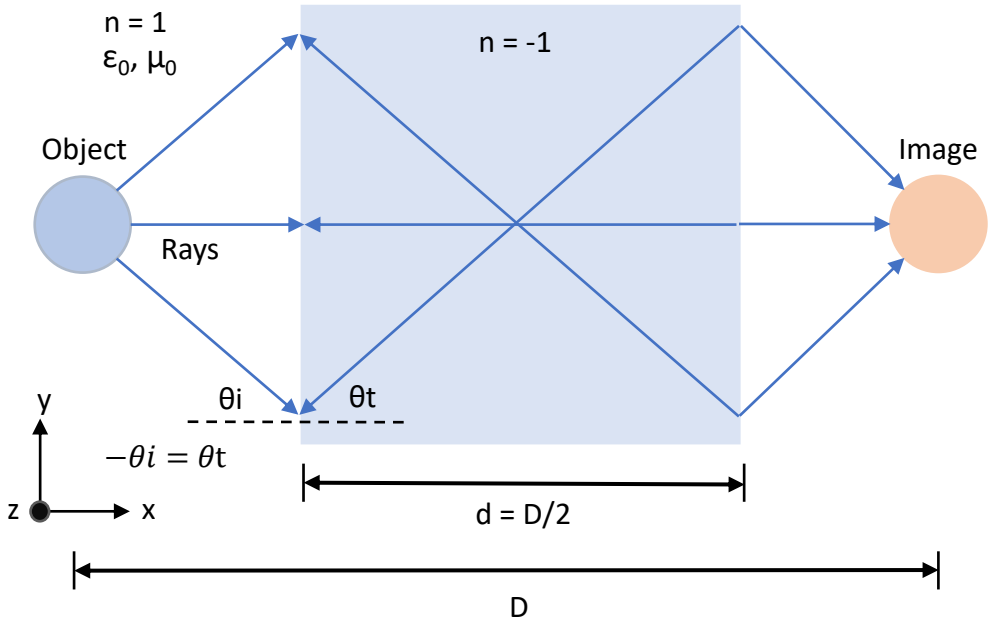

Figure 1.3: Sample ray tracing diagram for a Veselago lens.

amplify incident evanescent waves, was the first ever report of evanescent wave growth, and lead to widespread research into superlenses with negative refractive indices [9]. The mechanism behind evanescent wave amplification through a DNG slab lens is the internal coherent superposition of multiple reflected evanescent waves that arises from surface plasmon wave coupling across the slab's extent. [11]. Surface plasmons are both the collective oscillation of electrons along an interface, and the evanescent electromagnetic fields that they generate. When an incident evanescent wave strikes an interface separating two media with corresponding positive and negative material parameters (*i.e.* a positive and negative ε interface, or positive and negative μ interface), a surface plasmon may be excited. The evanescent fields of a surface plasmon are confined to the interface, meaning that they propagate along it, but decay on either side as they travel away from it. Flat DNG slabs can simultaneously support two surface plasmons, one occurring on each of its interfaces. The evanescent fields of these surface plasmons extend into the slab, coupling across its extent. When excited under the correct conditions, interference between strong, coupled surface waves acts to boosts the amplitudes

of incident evanescent waves over the slab's extent

1.2.3 Imperfect Superlenses

Due to the existence of losses in all materials, perfect lensing cannot be achieved in practice. The strong surface waves that are required for evanescent wave amplification are highly susceptible to absorption from material loss [12]. Sub-diffractive imaging can still be accomplished using lossy materials, but with finite resolution [13]. This challenge of superlens loss mitigation has been widely researched. Low loss superlens material design [14, 15, 16, 17], active gain integration [18, 19, 20, 21], and plasmon injection techniques [22, 23, 24] have been developed.

Alternatively, superlensing can be accomplished using single-negative (SNG) slabs. Flat SNG slabs characterized by having only a single negative parameter (*i.e.* either negative μ (MNG) or negative ε (ENG)) make an attractive alternative to their DNG counterparts as they are much easier to manufacture, and can operate over a wider temporal frequency range [9, 7, 8]. These two major benefits are most pronounced for ENG lenses which are not reliant on a magnetic material response. MNG material responses are extremely frequency sensitive and weak at higher temporal frequencies [25]. ENG superlensing, on the other hand, can be experimentally realized at optical frequencies using a simple flat silver slab [26].

SNG superlensing does however have some constraints. Evanescent wave amplification through an SNG slab relies on the static decoupling of radiative electric and magnetic fields. This decoupling can be assumed only if the lens' dimensions are electrically small [9]. When this is the case, p-polarized radiation is dependent only on the lens' electric permittivity, and s-polarization on the lens' magnetic permeability. This means that if operated within the quasi-static regime, and under the correct polarization, a thin SNG slab lens will exhibit similar evanescent wave amplification behaviour to a DNG superlens. These conditions for SNG superlensing restrict the lens' thickness and operation range, as well as the polarization direction of incident radiation.

1.3 Motivation and Goals

Super-resolution lenses have seen an increase in demand from the many industrial applications that desire fine detail images and subwavelength focal spots. Contemporary integrated circuit manufacturing, for example, relies primarily on light-based photolithography techniques to etch traces onto silicon wafers. The minimum geometric feature size that can be achieved by this process is dependent on the focal spot diameter of the lens that is used. A smaller focal spot enables smaller electronic device designs that are not only faster, denser, and more efficient, but whose reduced size would enable new applications [27]. In medicine, super-resolution lenses have the potential to greatly improve diagnostics. Non-invasive, real-time microscopic imaging of morphological and chemical cellular functions would allow for earlier detection of health related problems [28, 29]. Lenses are also commonly used for industrial inspection. Here, higher resolution lenses allow for better quality control by enabling closer, faster inspection of material flaws [30, 31].

Superlensing relies on strong surface wave interactions to amplify incident evanescent components. These necessarily high fields have their complications. In addition to being vulnerable to material loss, strong surface wave amplitudes exacerbate any minor interactions within an imaging system. Surface wave interactions between neighbouring optical components and the lens geometry itself have the potential to disrupt superlensing performance in unexplored ways. Conventional superlensing analysis techniques typically avoid having to account for these interactions by considering both flat, planar superlens slabs that extend to infinity in both transverse directions, and source-objects and image-detectors that are themselves virtual, reflectionless components. While these simplifications are useful tools for superlens performance evaluation, they are non-realistic optical component models that neglect the impact of unavoidable surface wave interactions.

In this thesis, we study how surface wave interactions with finite superlens geometry and external optical components can impact imaging performance. Realistically, any complete

superlensing system requires a superlens with finite-transverse width, and an object and detector that are both non-transparent, band-limited, physical components. Due to the strong surface wave amplitudes surrounding a superlens, such an imaging model will necessarily introduce unavoidable surface wave interactions with both the superlens geometry itself, and neighbouring optical components that are placed in near-field proximity to the lens. To evaluate the impact of external optical component interactions, we investigate a full, 1-D superlens imaging system, complete with a physical object and detector. In the process, we challenge conventional superlens performance benchmarking, and reveal new physics in the form of a secondary resonant amplification mechanism. We then perform full-wave simulations of a two-dimensional superlens with finite transverse width to examine its temporal frequency and spatial frequency characteristics. While the impact of finite transverse width on superlensing performance has been previously studied [32, 33, 34], a simultaneous investigation of both the temporal frequency and spatial frequency characteristics of dispersive, finite width superlenses has not been performed. Through our study, we show how both the transverse width and corner sharpness of a superlens become geometric variables that complicate the superlens response by adding reflections and radiation to the system. Expanding on previous finite-width superlens work, we develop simulation and analysis techniques to explore the impact of lens geometry on the resonances of homogeneous, dispersive, finite transverse-width superlenses.

1.4 Organization of this Thesis

The remainder of the thesis is organized as follows.

In Chapter 2 we provide background information on the superlensing phenomena and analysis techniques used in our research. First, we perform a quick overview of Fourier imaging techniques to establish the mathematical forms used in our analysis. Next, we discuss negative material parameters, and introduce the dispersive material models. Third, we summarize surface plasmon dispersion characteristics and their impact on superlensing performance. And

last, we discuss how surface plasmon waves travel around bends.

In Chapter 3 we investigate the effects of near-field interactions between single-negative superlenses and dielectric object and detector regions. We perform a joint simulation and analytic study to examine how reflections external to the lens impact imaging performance.

In Chapter 4 we develop simulation and analysis techniques to study the temporal and spatial characteristics of finite transverse-width superlens dispersion. We use finite-element method simulation tools to investigate how finite width lens geometry affects transmission and radiation.

In Chapter 5 we conclude our work, noting the major contributions of our research and recommending future work.

Chapter 2

Background

2.1 Fourier Imaging

Explication of how imaging resolution beyond the diffraction limit is achieved is best accomplished using spatial frequency Fourier analysis concepts. Any electromagnetic field distribution can be decomposed into a set of plane waves,

$$f_{\text{obj}}(\beta) = \int_{-\infty}^{\infty} E_{\text{obj}}(y) e^{-j\beta y} dy, \tag{2.1}$$

where $f_{\text{obj}}(\beta)$ is the object field spectrum, β is the wave vector transverse to the object plane for a two-dimensional system, and $E_{\text{obj}}(y)$ is the object field. Individual Fourier components within this plane wave set are defined by a unique spatial and temporal frequency combination. By superimposing individual weighted Fourier components, any field distribution can be generated.

Consider the two-dimensional ray diagram of a slab lens with interfaces normal to the x-axis shown in Fig. 1.3. Monochromatic plane waves within this lensing system propagate from the object to the image following the mathematical forms

$$\vec{E}_{\text{S}} = (E_x \hat{x} + E_y \hat{y}) e^{-jk_{\text{x}}x - j\beta y} \quad \text{and} \tag{2.2}$$

$$\vec{E}_{\text{P}} = E_z \hat{z} e^{-jk_{\text{x}}x - j\beta y}, \tag{2.3}$$

where E_S is the s-polarized electric field (in plane), E_P is the p-polarized electric field (out of plane), and k_{x} is the longitudinal wave vector. Source feature information is carried through the system by a superposition of such plane waves. Each plane wave can be understood as a

single Fourier component that is characterized by a unique longitudinal and transverse spatial frequency combination. The tranverse spatial frequency of a component determines the relative object feature size information that it can carry. Higher spatial frequency Fourier components, having greater transverse spatial frequencies, carry finer object detail information.

Abbe's Diffraction limit arises from the fact that propagating waves are physically restricted to have a maximum attainable transverse spatial frequency. In the two dimensional plane, the wavenumber of all free-space travelling electromagnetic plane-waves are constrained by the consistency equation

$$k_0^2 = \frac{\omega^2}{c^2} = k_{\mathrm{x}}^2 + \beta^2, \tag{2.4}$$

where ω is the angular frequency and c is the speed of light in vacuum. Following equation (2.4), propagating waves only exist when both k_{x} and β are real, that is to say $|k_{\mathrm{x}}|, |\beta| \leq k_0$. If the magnitude of the transverse wave-vector is greater than the wavenumber ($|\beta| > k_0$), then the consistency equation $k_0^2 = k_{\mathrm{x}}^2 + \beta^2$ requires that k_{x} become imaginary; $k_{\mathrm{x}} = -j\sqrt{\beta^2 - k_0^2}$. Under this circumstance, the electromagnetic wave is no longer propagating, but evanescent, and can be described by the electric fields

$$\vec{E}_{\mathrm{S}} = (E_x\hat{x} + E_y\hat{y})e^{-\sqrt{\beta^2 - k_0^2}x}e^{-j\beta y} \quad \text{and} \tag{2.5}$$

$$\vec{E}_{\mathrm{P}} = E_z\hat{z}e^{-\sqrt{\beta^2 - k_0^2}x}e^{-j\beta y}, \tag{2.6}$$

These evanescent plane wave components propagate transverse to the source plane ($\pm\hat{y}$, and decay exponentially with longitudinal distance from the source plane ($+\hat{x}$). Note that evanescent wave definition assumes only positive x values, and a source placed at $x = 0$. For negative x values (*i.e.* on the opposite side of the source), the sign of the longitudinal wave-vector must become positive so that the wave decays with longitudinal decay in the $-\hat{x}$ direction. The high transverse spatial frequencies of evanescent Fourier components allows them to carry the finer object detail information. However, rapid evanescent wave amplitude decay makes these components difficult or impossible to detect at the image plane. Note here that the fields decay

exponentially with both $\mathrm{Im}(k_y)$ and d. As a consequence, plane waves with higher β decay more quickly, and have negligible amplitudes at larger distances from the source plane.

2.2 Negative Material Properties

The ability to both focus propagating waves and amplify evanescent waves requires a simultaneous negative ε and μ material, where

$$\varepsilon = \varepsilon_{\mathrm{r}}\varepsilon_0 \quad \text{and} \tag{2.7}$$

$$\mu = \mu_{\mathrm{r}}\mu_0 \tag{2.8}$$

While negative ε materials and negative μ materials both naturally occur, materials with simultaneously negative ε and μ do not, and must instead be generated using metamaterials. Metamaterials are artificial materials engineered to exhibit specific, often exotic properties. Such materials can be constructed by building a periodic lattice array structure out of base unit cells. These unit cells are designed to have a precise electric or magnetic dipole response at a specific wavelength. When stacked together, wave interactions with the lattice structure produce an overall effective material permittivity and permeability.

Double-negative metamaterials can be manufactured by building lattices from unit cells containing both conductive loops and wire rods [35]. When operated in the gigahertz regime, wire rods with millimeter spacing can be modelled as an electric plasma [36]. Similarly spaced conductive loops have a magnetic response that is resonant in nature [37] that can also be modelled as plasmonic to simplify analysis. Dispersive plasmonic material responses can be mathematically represented using the Drude model,

$$\varepsilon_r = 1 - \frac{\omega_{\mathrm{p}\varepsilon}^2}{\omega^2}, \tag{2.9}$$

$$\mu_r = 1 - \frac{\omega_{\mathrm{p}\mu}^2}{\omega^2}, \tag{2.10}$$

where, $\omega_{p\varepsilon}$ is the electric plasma frequency, below which the permittivity is negative, $\omega_{p\mu}$ is the magnetic plasma frequency, below which the permeability is negative, and ω is the operation frequency. Operating a double-Drude modelled material below both $\omega_{p\varepsilon}$ and $\omega_{p\mu}$ generates a DNG response. Note that while metamaterials are lossy, loss has not been included in our simplified Drude models. When modeling DNG metamaterials, material loss is often added as an additional imaginary term to better enable the tailoring of loss conditions.

2.3 Surface Plasmon Dispersion

The amplification of evanescent Fourier components is delicately dependent on the off-resonant excitation of coupled surface plasmons across a superlens. Consider a double-Drude slab lens of thickness d that is immersed in free-space as shown in Fig. 1.3. This slab, defined by $\varepsilon_r = 1 - \omega_{p\varepsilon}^2/\omega^2$ and $\mu = 1 - \omega_{p\mu}^2/\omega^2$, can support up to four distinct resonant coupled surface plasmon branches with degenerate pair solutions when $\varepsilon = \mu$. These four distinct resonances manifest as upper (ω^+) and lower (ω^-) temporal frequency branches for both S and P polarizations. The dispersion relations that map the resonant temporal and spatial frequencies of these branches can be determined by solving Maxwell's equations for the slab's surface wave eigensolutions. These relations [38] can be derived as

$$\varepsilon(\omega^+) = -\varepsilon_0 \frac{k_x}{k_0} \coth(k_x d/2) \quad \text{and} \tag{2.11}$$

$$\varepsilon(\omega^-) = -\varepsilon_0 \frac{k_x}{k_0} \tanh(k_x d/2) \tag{2.12}$$

for p-polarized radiation, and

$$\mu(\omega^+) = -\mu_0 \frac{k_x}{k_0} \tanh(k_x d/2) \quad \text{and} \tag{2.13}$$

$$\mu(\omega^-) = -\mu_0 \frac{k_x}{k_0} \coth(k_x d/2) \tag{2.14}$$

for s-polarized radiation, where

$$k_{\mathrm{x}} = \sqrt{\frac{\omega^2}{v_p^2} - \beta^2} \tag{2.15}$$

and v_p is the phase velocity of the wave.

Such surface plasmon dispersion relations are useful tools for evaluating the viability of superlens designs. To illustrate this, consider the slab lens shown in Fig. 1.3 to be a double-Drude lens, with $\omega_{\mathrm{p}\varepsilon} = \omega_{\mathrm{p}\mu} = \omega_{\mathrm{p}}$, that is immersed in free-space, with a thickness, d, equal to half that of the imaging distance, D. In the left column of Fig. 2.1 we plot this lens's field transmission coefficient against both spatial and temporal frequency, with overlaid red curves indicating the location of the surface plasmon resonance branches. In the right column, we plot a cross-section of lens transmission along the chosen operation frequency, which is shown as a black horizontal line plotted on each transmission surface.

For this specific double-Drude lens, perfect lensing is achieved only when $\omega = \omega_{\mathrm{op}} = \omega_{\mathrm{p}}/\sqrt{2}$, the operating point at which $\varepsilon_{\mathrm{r}} = \mu_{\mathrm{r}} = -1$. Observing Fig. 2.1 (a), we see that this operation frequency is directly centered between the upper and lower surface plasmon branches (note that only two of the four surface plasmon branches are visible for this lens due to directly overlapping degenerate solutions from the matched μ_r and ε_r). In fact, the resonant branches of the matched double-Drude lens asymptotically approach ω_{op}, which ensures that the operating point will never intersect a resonance.

The perfect amplification of incident evanescent waves through a double-Drude operated at $\omega = \omega_{\mathrm{op}} = \omega_{\mathrm{p}}/\sqrt{2}$ is a result of the equal, off-resonant excitation of both the upper and lower surface plasmon resonances [11]. As illustrated in Fig. 2.2, the upper and lower surface plasmon branches have distinct field profiles. The upper branch has an asymmetric field profile with respect to the center of the lens, while the lower branch has a symmetric field profile with respect to the center of the lens. When these two branches are perfectly excited, the superposition of their respective fields results in the unity overall amplification of the incident evanescent wave.

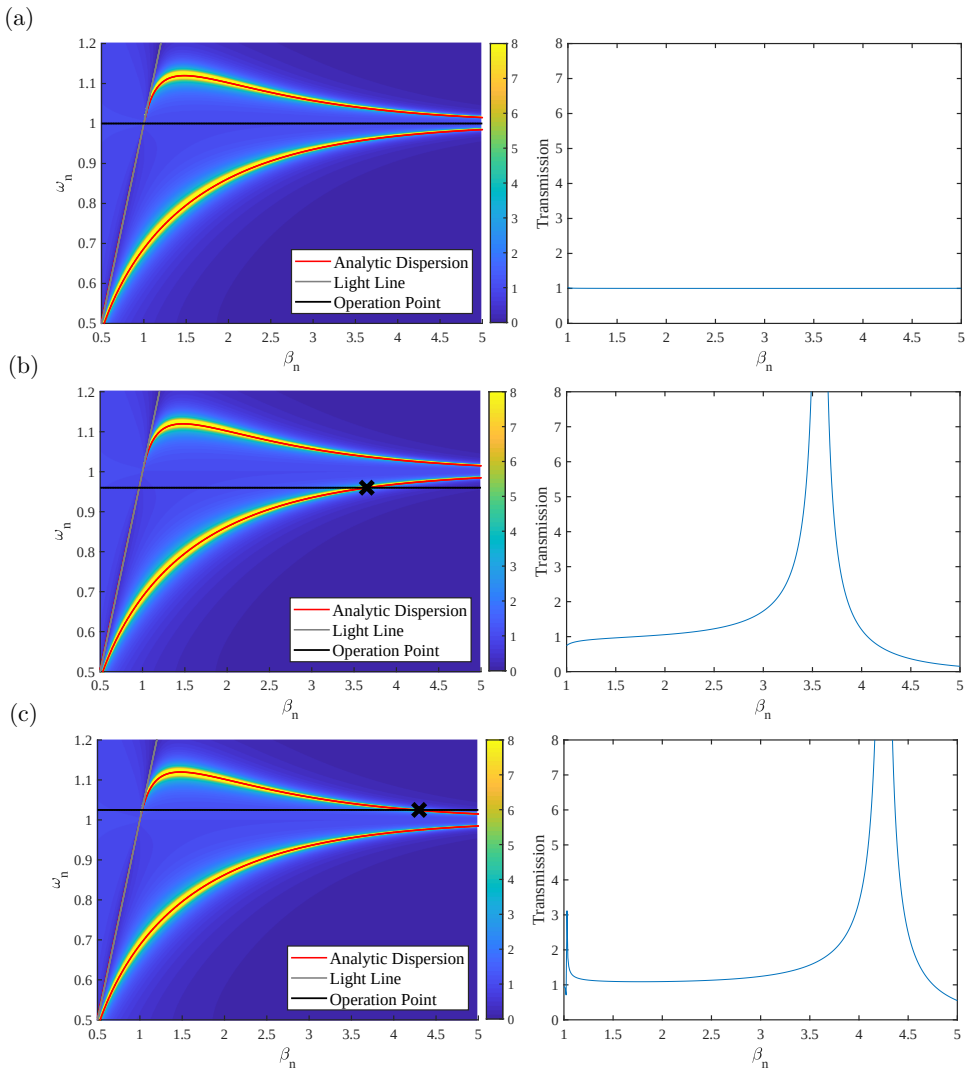

Figure 2.1: Calculated field transmission coefficient plots (left) and iso-frequency cut-lines (right) showing resonant intersections and resulting transmission cuts for operation at (a) $\omega_n = 1$, (b) $\omega_n = 0.96$ and (c) $\omega_n = 1.25$. All calculations are for a double-Drude slab superlens of thickness $\lambda_p/2\pi$. Note normalized axes $\omega_n = \omega/\omega_{op}$ and $\beta_n = \beta/k_{op}$ where $\omega_{op} = \omega_p/\sqrt{2}$, and $k_{op} = \omega_{op}/c$. Overlaid red curves indicate the analytic surface plasmon dispersion relations for the resonance condition.

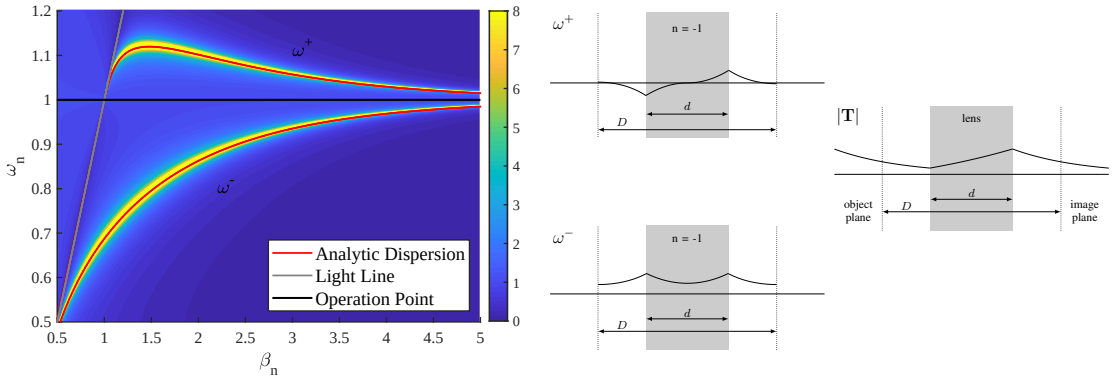

Figure 2.2: The superposition of off-resonance excited upper (ω^+) and lower (ω^-) surface plasmon branches of a perfect lens ($n = -1$) generates a unity overall transmission response.

Perfect lensing through a double-Drude lens requires operation at ω_{op}. An even slightly detuned operation frequency will necessarily intersect with either the upper or lower dispersion curve resonance. These intersections lead to resonant surface plasmon excitation that is detrimental to imaging in two ways. First, surface plasmon over-amplification that occurs near resonance can generate unwanted artefacts in the form of spectral side-lobes that obscure the image [39] (see Figs. 2.1(b) and 2.1(c)). Second, the off-resonant excitation of coupled surface plasmons that drives incident evanescent wave amplification is not maintained at spatial frequencies above the resonance crossing. Amplification of higher Fourier components rapidly deteriorates, and the lens' transmission response quickly approaches zero (again shown in Figs. 2.1(b) and 2.1(c)).

Unlike the DNG lens, an SNG slab only supports two surface plasmon branches: upper and lower frequency branches of polarization corresponding to the slab's single negative parameter. The location of these two branches also differs between single-Drude and double-Drude lenses. Because of this change in branch placement, any chosen single-Drude lens operation frequency, including ω_{op}, will necessarily intersect with a resonant branch. To illustrate this, in Fig. 2.3 we plot three transmission surfaces (left column) and their corresponding cross-sections (right column) for a slab single-Drude lens of thickness $d = D/2$. As the single-Drude lens' operating point nears a necessary resonance intersection, irregular spectral amplification deteriorates

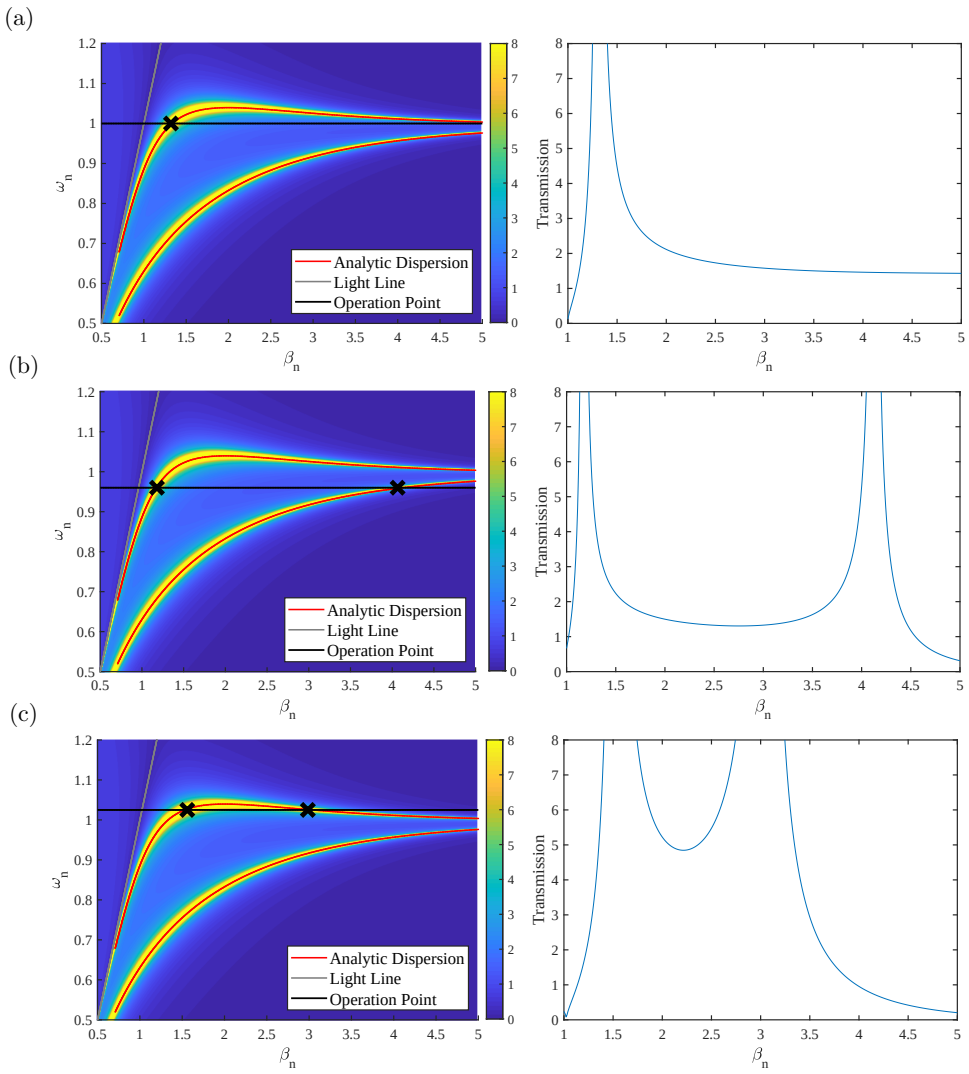

Figure 2.3: Calculated field transmission coefficient plots (left) and iso-frequency cut-lines (right) showing resonant intersections and resulting transmission cuts for operation at (a) $\omega_n = 1$, (b) $\omega_n = 0.96$ and (c) $\omega_n = 1.25$. All calculations are for a single-Drude slab superlens of thickness $\lambda_p/2\pi$. Note normalized axes $\omega_n = \omega/\omega_{op}$ and $\beta_n = \beta/k_{op}$ where $\omega_{op} = \omega_p/\sqrt{2}$, and $k_{op} = \omega_{op}/c$. Overlaid red curves indicate the analytic surface plasmon dispersion relations for the resonance condition.

the transmission response. The uniformity of the transmission response can be improved by reducing the lens' thickness. Reducing lens thickness separates the upper and lower resonance branches, providing a wider operation frequency window at a given transverse spatial frequency, and pushing resonant intersection points to higher spectral components. However, thinner lenses are more difficult to manufacture, and have a shorter, more sensitive operation distance.

2.4 Surface Plasmons Around a Bend

When a surface plasmon wave travels around a bend, it undergoes reflection, transmission, and radiation. Consider the Fig. 2.4 diagram of a DNG slab with a finite cross-section. With its transverse width constrained in this manner, any lens-traversing surface waves that would otherwise continuously propagate along a lens face will now necessarily intersect with one of its corners. The solutions to Maxwell's equations for a surface wave travelling along a curved geometry differ from those for a flat interface. As a result, the incident surface wave must undergo partial transmission and reflection at the lens corner. The portions of surface wave power that are reflected (indicated by the green path, E_r, in Fig. 2.4) and transmitted (indicated by the purple path, E_t, in Fig. 2.4) can be determined by summing the infinite number of wave solutions that exist over the extent of a lens corner [40].

The free-space coupling of surface plasmons that occurs at a lens corner can be attributed to the radial dependence of the surface wave's phase velocity [41]. The electromagnetic fields of a surface plasmon extend outward from the interface, decaying into both the lens and free-space regions. These electromagnetic fields pick up a radially dependent transverse phase velocity as the surface plasmon travels around the lens corner. Electromagnetic fields that extend further into the free-space region away from the lens interface attain a higher transverse phase velocity. When this phase velocity surpasses the free-space speed of light, said electromagnetic energy becomes radiative, and couple to free-space as propagating waves. This bend-induced radiation (shown as the red path, E_c, in Fig. 2.4) is an intrinsic source of loss for finite transverse-width superlenses.

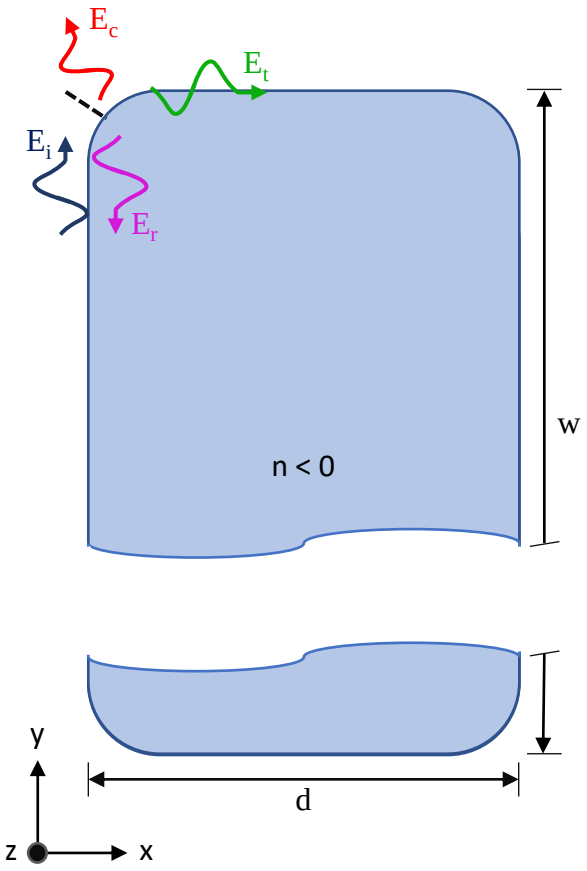

Figure 2.4: A diagram of a superlens with a finite thickness d, finite width w, infinite length and circularly curved corners. Wavy arrows illustrate the surface plasmon reflection (E_r, purple), transmission (E_t, green) and free-space coupling (E_c, red) that may occur when an incident surface plasmon (E_i, blue) traverses a lens corner.

Chapter 3

Optical Component Interactions

In this Chapter we present a study of the effects that interactions between a superlens and the external optical components that form a complete imaging system can have on lensing performance. In its simplest form, an imaging system requires three optical components. First, there is a source object that generates the electromagnetic field distribution to be imaged. Next, there is an image detector that is placed opposite the object, whose role is to convert the transmitted electromagnetic field into a real-power carrying signal. And finally, there is a lens that is placed between the object and the detector, whose role is to restore the source electromagnetic field distribution at the imaging location.

When interactions between the source, lens, and detector occur in the far-field, as is the case for conventional lenses, their resulting impact on imaging performance can often be considered negligible. Unlike conventional lenses, superlenses require near-field operation. This short operating distance combined with the strong surface waves that are necessary for incident evanescent wave amplification can generate significant interactions between the lens and neighbouring optical components. The impact that strong near-field reflections between optical components can have on superlensing performance should be considered.

Typically, superlensing studies focus primarily on lens design, isolating the response of the lens from the rest of the imaging system [9, 12, 31, 33]. However, when moving from simulation to experiment, the requirement of a source-object and image-detector introduces external interactions that can perturb lens transmission, and introduce coupling between optical components. The coupling of surface waves between superlensing components was previously noted in a 2011 experimental study of an NSOM based imaging system, where a scanning probe was used in combination with an SNG slab superlens in an attempt to boost imaging

performance [7]. Evanescent wave transmission through the imaging system was found to improve when the scanning probe was placed at specific distances from the SNG lens. It was hypothesized that surface wave coupling between the lens-face and probe-tip boosted incident evanescent wave amplification to improve the transmission response. While such evanescent wave amplification over free-space has been used before in multi-layer superlens design [42, 43, 44, 45], inter-component coupling of surface waves within a complete superlensing system has been otherwise unexplored.

In our research, we look to investigate how surface-wave coupling between the necessary optical components that form a complete imaging system impact superlensing performance. By examining field transmission through a simple, 1-D imaging system, we reveal a novel external resonance that acts as a secondary mechanism for incident evanescent wave amplification. Focusing on this secondary resonance, we derive analytic expressions to describe its impact on lens transmission, and perform simulation studies to observe its influence on imaging performance. Our findings reveal that this external resonance condition can greatly boost evanescent wave amplification through an MNG superlens, increasing the lens' operation range, and ameliorating absorption effects introduced by lens loss.

3.1 Imaging Model

To facilitate the analysis of interactions between optical components, we examine a one-dimensional superlensing system consisting of a flat, planar SNG superlens slab that is immersed in free-space, and centered between matched dielectric half-spaces (see Fig. 3.1). To observe the effects that different negative material parameters have on imaging performance, we separately consider two well-defined SNG lens types; a homogeneous ε-negative lens with $\varepsilon_r = -1$, $\mu_r = 1$, and a homogeneous μ-negative lens with $\varepsilon_r = 1$, $\mu_r = -1$. These SNG lenses make ideal candidates for our analysis as they have been widely investigated theoretically [9, 46, 47, 48, 49], and experimentally realized across the electromagnetic spectrum

[50, 51, 16, 52, 53, 54]. Furthermore, SNG lenses have a high reflection coefficient, which, when combined with near-field operation, results in a strong potential for interactions with adjacent optical components.

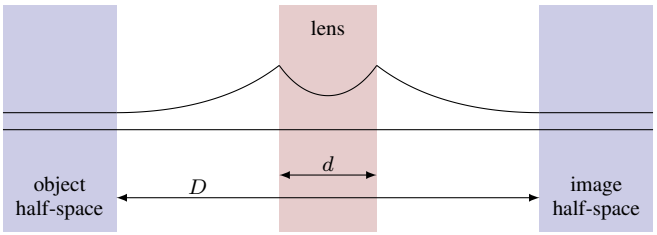

Figure 3.1: A one dimensional model of a superlens-based imaging system. A superlens slab of thickness d is embedded within a dielectric imaging system having dielectric object and detector half-spaces, both of which are defined by a refractive index of $n = 4$, and are separated by a distance D. The black curve sketches the field envelope of a sample wave component with transverse wave number $k_0 \leq \beta \leq nk_0$ transmitted through an SNG superlens. ©

The dielectric half-spaces used in our simulation model represent object and detector regions with refractive indices of $n = 4$. This decision to model the source-object and image-detector as dielectric half-spaces carries significance beyond simply selecting a well-defined material to enable partial reflections from both components. Any source-object or image-detector implemented in a real-world imaging system would necessarily have its own band limitations. By modelling our object and detector as dielectric half-spaces, we simulate these external component band limitations, and in doing so restrict our analysis to an upper spatial frequency maximum of nk_0.

3.2 Signal Flow

Transmission through our five-layer imaging system is dependent on multiple-reflections between material layers. The impact that these reflections have on overall system transmission and reflection can be both illustrated and quantified using a signal flow graph. Let us first consider an SNG slab lens that is bounded on either side by a semi-infinite region of free-space. In this scenario, the waves scattered by the lens extend out to infinity, and there is no reflection

from either the object or detector. Figure 3.2(a) shows the signal flow for such an isolated lens. Total field transmission, t, and reflection, r, through this system can be seen to depend entirely on the lens itself (i.e. $r = r_0$ and $t = t_0$, where r_0 and t_0 are the field reflection and transmission coefficients for the slab lens).

Placing the SNG lens between dielectric object and detector regions (Fig. 3.2(b)) introduces additional reflections to the system. These multiple reflections between adjacent imaging components affect overall field transmission and reflection, generating feedback loops within the free-space regions that separate the lens from the object and detector. Invoking Mason's rule [55], we can derive expressions for the field transmission and reflection coefficients of this five-layer system,

$$t = \frac{(1-\rho)t_0(1+\rho)}{1-\rho r_0-\rho r_0-\rho^2 t_0^2+\rho^2 r_0^2}, \tag{3.1}$$

$$r = -\rho + \frac{(1-\rho)r_0(1+\rho)(1-r_0\rho)+(1-\rho)t_0\rho t_0(1+\rho)}{1-\rho r_0-\rho r_0-\rho^2 t_0^2+\rho^2 r_0^2}, \tag{3.2}$$

which can be simplified to

$$t = \frac{(1-\rho^2)t_0}{(1-r_0\rho)^2-(t_0\rho)^2}, \tag{3.3}$$

$$r = \frac{(r_0\rho-1)(\rho-r_0)+\rho t_0^2}{(1-r_0\rho)^2-(t_0\rho)^2}, \tag{3.4}$$

where ρ is the reflection coefficient for the air-dielectric interface.

These equations show that lens performance is strongly dependent on ρ. Multiple reflections that occur between material layers generate resonant paths external to the lens whose impact on field reflection and transmission can be observed by the denominator of equations (3.3) and (3.4), respectively. Over the free-space evanescent regime, where $k_0 \leq |\beta| \leq nk_0$, the magnitude of the air-dielectric field reflection coefficient becomes unity, allowing the denominator of equations (3.3) and (3.4) to attain small values. When this is the case, overall field

reflection and transmission through the lensing system can surge, and impact imaging in yet unexplored ways.

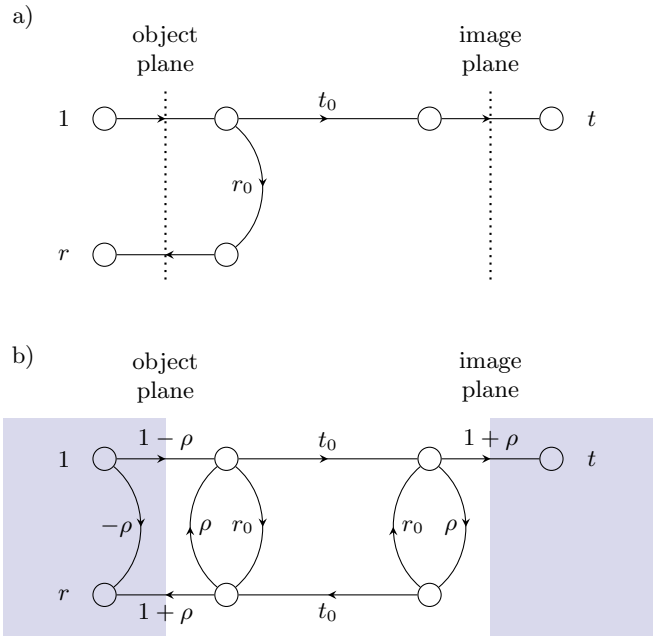

Figure 3.2: Signal flow graph for (a) an isolated superlens and (b) a superlens embedded between dielectric object and detector regions. The symbols t_0 and r_0 represent the field transmission and reflection coefficients of the bare lens while t and r represent the field transmission and reflection coefficients of the complete system. The Fresnel reflection coefficient at the dielectric interface from free-space is given by ρ.

3.3 Planar Multi-system Analysis

To evaluate the impact of optical component reflections on imaging performance, we seek to calculate field transmission through a five-layer imaging system over a range of lens thicknesses and imaging distances. In this section, we describe the numerical method used to solve for the forward and backward propagating waves in each region of a general planar multi-layered system under plane-wave incidence. Once the electromagnetic waves have been determined, the overall spectral response of the imaging system can then be found by calculating the transfer function for each spatial frequency plane-wave component.

Consider the multi-layer system shown in Fig. 3.3. Here, M interfaces, aligned normal to

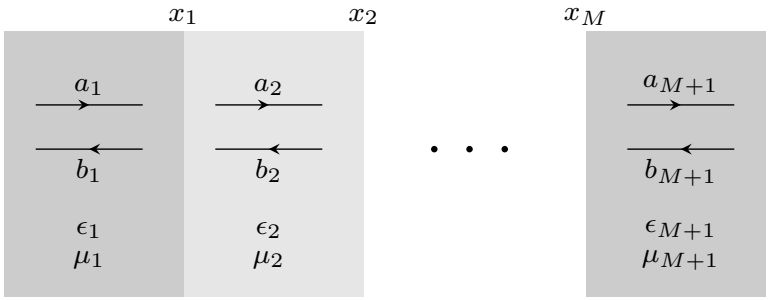

Figure 3.3: Diagram of an $(M+1)$-layer imaging system showing the interface locations and properties of each region.

the x-axis, separate $M+1$ layers that have a relative permittivity of ε_i and relative permeability of μ_i. The fields in each region can be expressed as

$$E_{\mathrm{s}\|} = a_{\mathrm{i}} e^{-jk_i x_i} + b_i e^{jk_i x_i}, \quad \text{or} \tag{3.5}$$

$$H_{\mathrm{p}\|} = a_{\mathrm{i}} e^{-jk_i x_i} + b_i e^{jk_i x_i} \tag{3.6}$$

where a_{i} and b_{i} represent the forward and backward wave coefficients for the transverse electric fields of s-polarized waves (denoted as E_{s}) or the transverse magnetic fields of p-polarized waves (denoted as H_{p}). The fundamental electromagnetic boundary conditions for an interface free of surface current require that

$$E_{\|1} = E_{\|2} \quad \text{and} \tag{3.7}$$

$$H_{\|1} = H_{\|2}, \tag{3.8}$$

where $E_{\|}$ and $H_{\|}$ are the transverse electric and magnetic fields, respectively. Here, x_i is the interface location, and the longitudinal wave vector in each region, denoted as k_i, can be expressed as

$$k_i = \begin{cases} \sqrt{\varepsilon_i \mu_i k_0^2 - \beta^2}, \text{when } \varepsilon_i \mu_i k_0^2 > \beta^2 \\ \\ -j\sqrt{\beta^2 - \varepsilon_i \mu_i k_0^2}, \text{when } \varepsilon_i \mu_i k_0^2 < \beta^2, \end{cases} \tag{3.9}$$

where β is the transverse spatial frequency of the incident plane wave. Applying these boundary conditions to our multi-layer system, we match the transverse fields at each interface

$$a_i e^{-jk_i x_i} + b_i e^{jk_i x_i} = a_{\mathrm{i+1}} e^{-jk_{\mathrm{i+1}} x_i} + b_{\mathrm{i+1}} e^{jk_{\mathrm{i+1}} x_i}, \tag{3.10}$$

$$\frac{a_i}{g_i} e^{-jk_i x_i} - \frac{b_i}{g_i} e^{jk_i x_i} = \frac{a_{\mathrm{i+1}}}{g_{\mathrm{i+1}}} e^{-jk_{\mathrm{i+1}} x_i} - \frac{b_{\mathrm{i+1}}}{g_{\mathrm{i+1}}} e^{jk_{\mathrm{i+1}} x_i}, \tag{3.11}$$

where $i = 1, ..., M$, and the conversion factor between electric and magnetic field coefficients, g_i, can be expressed as

$$g_i = \begin{cases} \eta_0 k_0 \mu_i / k_i, & \text{for s-polarized waves,} \\ \\ k_0 \varepsilon_i / \eta_0 k_i, & \text{for p-polarized waves,} \end{cases} \tag{3.12}$$

where η_0 is the free-space impedance. The unknown wave coefficients are calculated by setting $b_{M+1} = 0$ and solving the $2M$ boundary condition equations in terms of the incident wave coefficient a_1. The total field transmission and reflection is then calculated as the ratio of the transmitted and reflected field to incident field using

$$t = \frac{a_{M+1}(x_M)}{a_1(x_1)} \qquad \text{and} \qquad r = \frac{b_1(x_1)}{a_1(x_1)}. \tag{3.13}$$

3.4 Spectral Transmission Comparison

Next, using results from the methods described in section 3.3, we compare the spectral transmission of an isolated SNG lens to that of ENG and MNG lenses that are embedded within

dielectric imaging systems. This comparison is made complicated by our three degrees of freedom; transmission through each imaging system is dependent on the lens thickness, the distance separating the object and detector, and the transverse spatial frequency of the incident wave. To enable comparison over all of these variables, we plot spectral transmission through each lensing system against both imaging distance, D, and lens thickness, d. In these plots, imaging distance is varied from zero to λ, and lens thickness from zero to D (see Fig. 3.4). This comparison provides a limited view of the spatial-frequency spectrum, but allows us to observe transmission over a range of lens thicknesses and imaging distances.

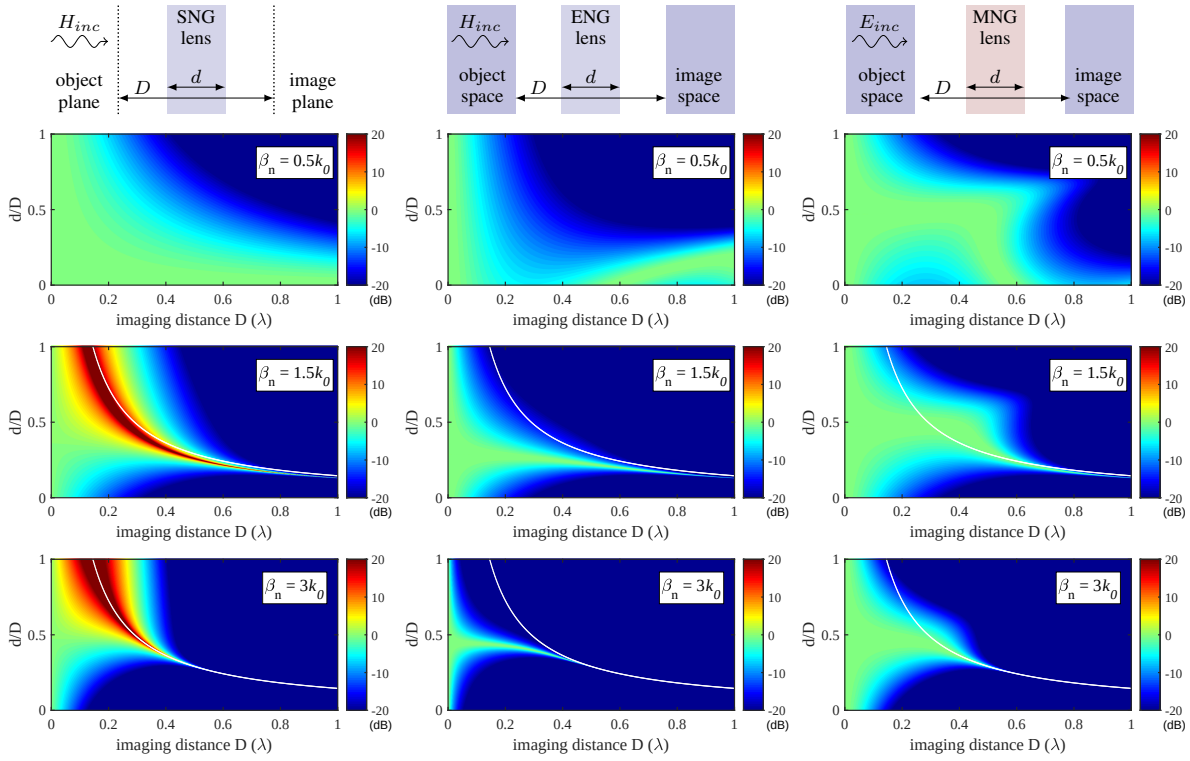

(a) (b) (c)

Figure 3.4: Field Transmission (dB) of wave components $\beta = 0.5k_0$, $\beta = 1.5k_0$, and $\beta = 3k_0$ through (a) an SNG lens placed in free-space, (b) an ENG lens placed between dielectric object and image regions, and (c) an MNG lens placed between dielectric object and image regions. Transmission is plotted as a function of relative lens thickness d/D and total imaging distance D. The overlaid white line indicates the slab resonance thickness of equation (3.14).

Figure 3.4 presents the spectral transmission response of the following three cases: (a) an ENG lens in free-space (*i.e.* with virtual object and image planes), (b) an ENG lens within

a dielectric imaging system, and (c) an MNG lens within a dielectric imaging system. The diagrams at the top of the figure indicate which corresponding imaging system plots are shown in each column. The ENG lenses used in (a) and (b) are lossless with $\varepsilon_r = -1$ and $\mu_r = 1$ and are illuminated by p-polarized waves. The MNG lens used in (c) is lossless with $\varepsilon_r = 1$ and $\mu_r = -1$ and is illuminated by s-polarized waves. All dielectric regions are lossless and non-magnetic, with refractive indices of $n = 4$. Three separate spectral component sample cases are plotted; one component below the free-space cutoff ($\beta = 0.5k_0$, top row), one component above and near the free-space cutoff ($\beta = 1.5k_0$, middle row), and one component below and near the dielectric region cutoff ($\beta = 3k_0$), bottom row.

Comparing the spectral transmission responses of the three imaging configurations in Fig. 3.4, we first note how the introduction of dielectric object and image regions in (b) and (c) limits its maximum transmission. For an SNG lens isolated in free-space, shown in (a), all incident and transmitted waves beyond the free-space cut-off are evanescent and carry no longitudinal power (*i.e.* normal to the layers). There is therefore no restriction placed on the magnitude of the transmission coefficient, as seen by the red shaded regions indicating > 20 dB amplification in the $\beta = 1.5k_0$ and $\beta = 3k_0$ plots. In contrast to the free-space SNG lens system, when a dielectric imaging system is used, incident waves below the dielectric region cut-off are propagating, and carry real power that must be conserved. This conservation of real power constrains the transmission coefficient in Figs. 3.4(b) and 3.4(c) to unity (corresponding to 0 dB, visible as green in Fig. 3.4). In these systems, incident propagating waves within the dielectric regions undergo partial reflection and transmission at the dielectric-free-space interfaces, coupling to evanescent waves for $k_0 \leq |\beta| \leq 4k_0$. Real power is carried through the intermediate layers of the system that separate the object and detector by the superposition of incident and reflected evanescent waves that decay in opposite directions.

As discussed in Chapter 2, an isolated SNG slab lens provides above-unity spectral amplification to incident evanescent waves when excited near the coupled surface plasmon resonance

condition (also known as slab resonance). For an SNG slab, this resonance occurs when the condition

$$e^{(\beta^2+k_0^2)^{1/2}d} = \frac{\beta^2}{k_0^2} + \sqrt{\frac{\beta^4}{k_0^4} - 1} \tag{3.14}$$

is satisfied [56]. The lens thickness corresponding to this slab resonance is plotted as an overlaid white line for all $\beta = 1.5k_0$ and $\beta = 3k_0$ components of Fig. 3.4. Examining first evanescent wave transmission through the isolated SNG lens shown in Fig. 3.4(a), we see that the regions of high transmission closely follow the slab resonance condition, converging to it as the imaging distance is increased to lengths that require such strong amplification that can only be supplied at resonance. Comparing this response to the transmission response of the $\beta = 1.5k_0$ and $\beta = 3k_0$ components of the Fig. 3.4(b) ENG lens embedded within a dielectric imaging system, we see a similar converging of the high transmission regions (which are in this case the 0 dB regions) to the slab resonance thickness at higher imaging distances. However, at shorter imaging distances the high transmission regions appear slightly perturbed from the slab-resonance thickness, following a more horizontal path that extends outwards from the left to the right of the plot. The Fig. 3.4(c) transmission response of an MNG lens within a dielectric imaging system is significantly different from that of both prior discussed imaging systems. While once again we observe that the high transmission regions converge to slab resonance at longer imaging distances, at shorter imaging distances these regions are much more expansive, visibly bulging out from the resonance thickness upwards, to the right of each plot.

This bulging of the $\beta = 1.5k_0$ and $\beta = 3k_0$ high transmission regions indicates that interactions between the MNG lens and dielectric object and detector half-spaces introduce an additional mechanism for evanescent wave amplification. Recall from earlier discussion that evanescent wave amplification through an isolated SNG lens relies entirely on multiply reflected surface plasmon waves that couple between slab interfaces. We have also seen that the addition of dielectric object and image regions introduces external reflections to the imaging system that can strongly impact wave transmission over the evanescent regime. Here, it ap-

pears that similar to slab resonance, which is responsible for evanescent wave amplification within the lens, external resonances could act as a secondary mechanism for evanescent wave amplification outside the lens.

3.5 External Resonance Investigation

To investigate the impact of external resonances, let us consider a simplified three-layer system comprising a dielectric half-space and SNG half-space that are separated by a free-space gap of length δ (see Fig. 3.5). Again, we consider the SNG region to be either an ENG ($\varepsilon_r = -1$) medium under p-polarization or an MNG ($\mu_r = -1$) medium under s-polarization. While a propagating wave incident from the dielectric region will not transmit power into the SNG half-space, partial reflection and transmission from each layer will establish a surface plasmon on the SNG region interface. The strength of the excited surface plasmon is determined by the coherent superposition of multiple reflected waves within the free-space cavity. To investigate potential evanescent wave amplification by this mechanism, we are interested in calculating the peak field intensity of the surface mode at the SNG interface given a unity magnitude propagating wave incident from the dielectric medium. This corresponds to the transmission coefficient calculated from (3.13) with $M = 2$ with transverse wave-vectors within the range $k_0 \leq \beta \leq nk_0$.

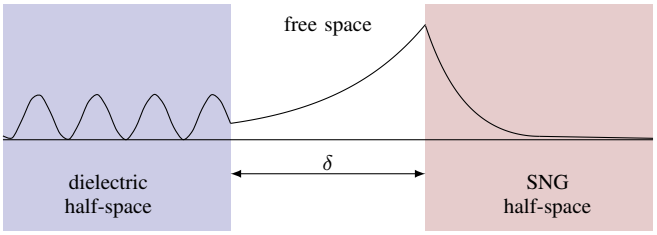

Figure 3.5: A one dimensional model of the three-layer free-space resonance geometry. A dielectric half-space is separated from an SNG half-space by a free-space gap of length δ. The black curve sketches a sample field envelope for a wave component with transverse wave vector $k_0 \leq \beta \leq nk_0$

Within the dielectric half-space, forward and backward travelling s-polarized plane waves

with $k_0 \leq \beta \leq nk_0$ have the form

$$\mathbf{E}(x,y) = (a_1 e^{-jk_{px}x - j\beta y} + b_1 e^{jk_{px}x - j\beta y})\hat{z}, \tag{3.15}$$

where a_1 and b_1 are the forward and backward wave coefficients for this region, respectively, and $k_p = \sqrt{n^2 k_0^2 - \beta^2}$ is the longitudinal wave-vector. Within the free-space region, forward and backward decaying s-polarized plane waves with $k_0 \leq \beta \leq nk_0$ have the evanescent form

$$\mathbf{E}(x,y) = (a_2 e^{-\alpha_0 x - j\beta y} + b_2 e^{\alpha_0 x - j\beta y})\hat{z}, \tag{3.16}$$

where a_2 and b_2 are the forward and backward wave coefficients for this region, respectively, and $\alpha_0 = \sqrt{\beta^2 - k_0^2}$ is the evanescent decay coefficient for free-space. Finally, within the SNG half-space, the s-polarized plane wave decays in the forward direction with the form

$$\mathbf{E}(x,y) = a_3 e^{-\alpha_L x - j\beta y}\hat{z}, \tag{3.17}$$

where a_3 is the forward wave coefficient for this region, and $\alpha_L = \sqrt{\beta^2 + k_0^2}$ is the SNG decay rate. Similar expressions exist for the magnetic fields of a p-polarized wave incident on an MNG half-space.

The transmission coefficient for s-polarized waves incident on an ENG half-space and p-polarized waves incident on an MNG half-space can be calculated by solving a 5×5 matrix using the method outlined in Sec. 3.3. For s-polarized waves incident on the ENG half-space, the magnitude of this field transmission coefficient squared is given by

$$|t_{\mathrm{s}}|^2 = \frac{\dfrac{16\alpha_0^2 k_{\mathrm{P}}^2}{(\alpha_0^2 n^4 + k_{\mathrm{P}}^2)}}{(\alpha_{\mathrm{L}} - \alpha_0)^2 X + 4k_0^2 \dfrac{(\alpha_0^2 n^4 - k_{\mathrm{P}}^2)}{(\alpha_0^2 n^4 + k_{\mathrm{P}}^2)} + \dfrac{(\alpha_0 + \alpha_{\mathrm{L}})^2}{X}} \tag{3.18}$$

and for p-polarized waves incident on the MNG half-space, the magnitude of this field trans-

mission coefficient squared is given by

$$|t_{\mathrm{p}}|^2 = \frac{\dfrac{16\alpha_0^2 k_{\mathrm{P}}^2}{(\alpha_0^2+k_{\mathrm{P}}^2)}}{(\alpha_{\mathrm{L}}-\alpha_0)^2 X + 4k_0^2\dfrac{(\alpha_0^2-k_{\mathrm{P}}^2)}{(\alpha_0^2+k_{\mathrm{P}}^2)} + \dfrac{(\alpha_0+\alpha_{\mathrm{L}})^2}{X}} \tag{3.19}$$

where

$$X = e^{2\alpha_0\delta}.$$

To find the maximum resonance field strength generated on the SNG interface, we look to optimize transmission over the gap-distance, δ, which can be done by optimizing (3.19) and (3.18) over X. Both of these field transmission equations follow the form

$$f(X) = \frac{C_0}{C_1 X + C_2 + C_3/X}.$$

The denominators of this form are convex functions (*i.e.* any line segment joining two points on its graph does not contain a point below the graph), with a single minimum at $X_{opt} = \sqrt{C_3/C_1}$. The overall function is therefore quasi-concave, (*i.e.* for any number, a, the set of points for which $f(X) \geq a$ is convex) with a single maximum at

$$X_{\mathrm{opt}} = e^{2\alpha_0\delta_{\mathrm{opt}}} = \frac{(\alpha_{\mathrm{L}}+\alpha_0)}{(\alpha_{\mathrm{L}}-\alpha_0)} = \frac{\beta^2}{k_0^2} + \sqrt{\frac{\beta^4}{k_0^4} - 1}. \tag{3.20}$$

Equation 3.20 defines the free-space gap resonance condition, and is notably similar to the slab resonance condition of (3.14). Plugging (3.20) into (3.19) and (3.18), the peak transmission coefficient corresponding to the resonant free-space gap length, δ_{opt}, can be simplified as,

$$|t_{\mathrm{p,opt}}| = \frac{1}{n^2}\sqrt{2\left(n^2 - \frac{\beta^2}{k_0^2}\right)}, \tag{3.21}$$

$$|t_{\mathrm{s,opt}}| = \sqrt{2\left(n^2 - \frac{\beta^2}{k_0^2}\right)}, \tag{3.22}$$

where the subscripts s and p denote the polarization. From (3.20), we see that the optimal cavity length does not depend on the specific properties of the dielectric region, and is therefore identical for both ENG and MNG configurations. The corresponding peak surface plasmon field intensity, however, is strongly dependent on both the refractive index of the dielectric region and polarization of the incident wave. When $\beta = k_0$, field transmission through the ENG lens reaches its peak. The refractive index for maximum field transmission can then be determined as

$$\begin{aligned} \frac{d}{dn}|t_{\mathrm{p,opt}}| &= 0 \\ 0 &= \frac{\sqrt{2}n^3/\sqrt{n^2-1} - 2n\sqrt{2(n^2-1)}}{n^4} \\ \therefore n &= \sqrt{2} \end{aligned} \tag{3.23}$$

Plugging equation (3.23) into (3.21), we find that maximum field transmission through the ENG system is $\sqrt{0.5}$ (71%). While the ENG surface plasmon is limited to a maximum strength of $\sqrt{0.5}$, limiting the amplification that can be provided by this mechanism for an ENG lens within a dielectric imaging system, However, comparing (3.21) and (3.22), we see that the MNG surface plasmon is excited with field intensities a factor of n^2 times larger than that of the ENG. This strong plasmon excitation indicates good potential for the free-space resonance to behave as a secondary amplification mechanism for incident evanescent waves through a dielectric-embedded MNG lensing system. In the next section, we will show how this resonant amplification mechanism affects five-layer lensing system field transmission.

3.6 Spectral Transmission Comparison Revisited

In Sec. 3.5, we showed that a polarization dependent secondary resonant amplification mechanism is introduced when dielectric object and detector half-spaces are used. To verify that this resonance is responsible for improving the MNG lens transmission response, we re-plot

our Fig. 3.4 spectral transmission graphs, but now include overlaid curves to indicate the free-space resonance gap length, δ_{opt}. These plots are shown in Fig. 3.6, where, as before, the rows present $\beta = 0.5k_0$ (top), $1.5k_0$ (middle), and $3k_0$ (bottom) components and the columns present (a) an ENG lens in free-space, (b) an ENG lens within a dielectric imaging system, and (c) an MNG lens within a dielectric imaging system. The overlaid white curve indicates the (3.14) slab resonance, and the gray curve indicates the (3.20) gap resonance.

The Fig. 3.6 plots support our secondary resonance hypothesis. Observing the $\beta = 1.5k_0$ and $\beta = 3k_0$ transmission plots of the MNG lensing configuration shown in Fig. 3.6(c) we see that the observed high transmission region bulging closely aligns with the gap-resonance condition, following it as it travels upwards and to the right of each plot. This is evidence that the secondary free-space gap resonance is a strong amplification mechanism for the MNG lens, as was predicted by (3.22). In Fig. 3.6 (b) we do not see a similar bulging of the high evanescent wave transmission regions along the gap resonance for the ENG lensing configuration. This result is also supported, this time by (3.21), which limits the maximum amplification of the ENG lens's p-polarized radiation within the free-space gap to $\sqrt{0.5}$.

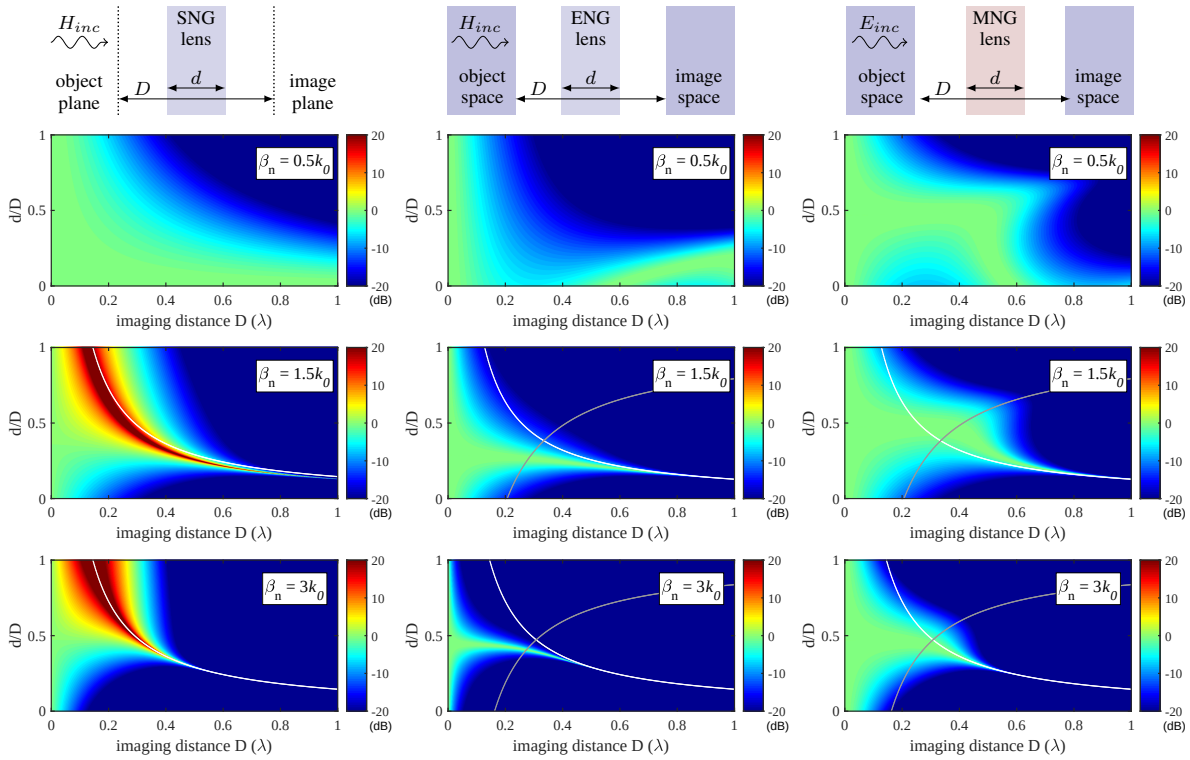

Figure 3.6: Transmission (dB) of wave components $\beta = 0.5k_0$, $\beta = 1.5k_0$, and $\beta = 3k_0$ through (a) an SNG lens placed in free-space, (b) an ENG lens placed between dielectric object and image regions, and (c) an MNG lens placed between dielectric object and image regions. Transmission is plotted as a function of relative lens thickness d/D and total imaging distance D. The overlaid white and grey lines indicate the slab resonance thickness of (3.14) and free-space gap resonance of (3.20), respectively.

3.7 Amplification Comparison

Let us now take a closer look at how the slab resonance and gap resonance provide evanescent wave amplification through the dielectric ENG and MNG imaging systems. To do this, we study field cross-sections through each lensing system at specific imaging distances and lens thicknesses chosen to separately satisfy the (3.14) slab resonance and (3.20) gap resonance conditions. Plotting these field cross-sections allows us to view how the different amplification mechanisms manifest in each imaging system.

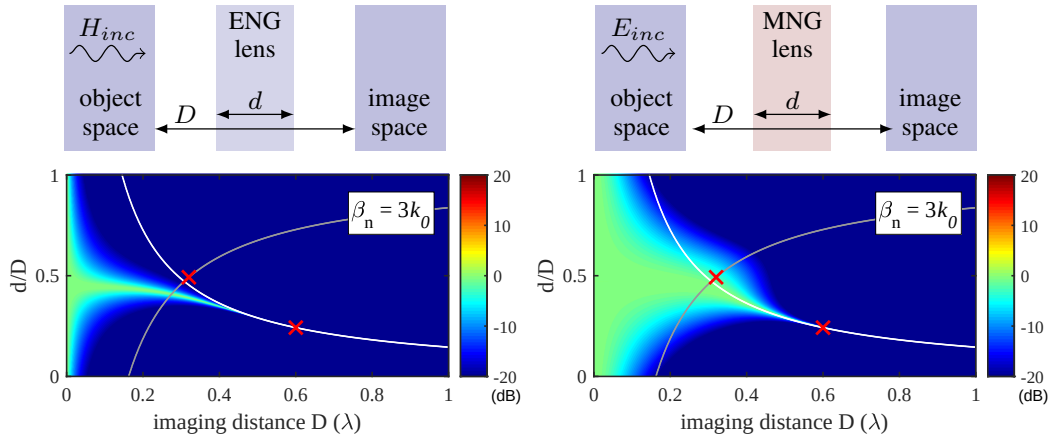

Figure 3.7: Transmission of a $\beta_n = 3k_0$ spectral component through a dielectric-embedded ENG lens (left) and dielectric-embedded MNG lens (right). Red markers indicate the imaging distances and lens thicknesses for which field cross-sections through the lensing system are plotted in Fig. 3.8.

Figure 3.8 plots cross-sections of the transverse field for two dielectric-embedded ENG lens configurations and two dielectric-embedded MNG lens configurations. The chosen lens thicknesses and imaging distances are highlighted by red markers that are shown in the Fig. 3.7 transmission plots for both systems. In each field cross-section plot, the transverse wave vector is set to $\beta = 3k_0$, and the transverse field is normalized with respect to the incident wave amplitude. A $\beta = 3k_0$ component is chosen for this analysis as its relatively high decay rate requires strong amplification to maintain high transmission. The high fields necessary to provide such strong amplification will emphasize field profile differences between each system's amplification mechanisms.

An imaging distance of $D = 0.6\lambda$ and relative lens thickness of $d/D = 0.2422$ provides an example of configurations which satisfy the slab resonance condition in (3.14), and correspond to the rightmost markers of the plots in Figs. 3.7. Here, we see two similar, symmetric field profiles that are consistent with the excitation of an even coupled-plasmon mode within the SNG slab (refer to Fig. 2.2). The MNG lens excites stronger surface plasmon waves than the ENG lens, generating a transmission profile that remains high over a wider range of imaging distances, which indicates that the MNG imaging system is more robust to perturbations away from the slab resonance condition. Still, the high transmission region for each configuration converges to the lens thickness predicted by (3.14), implying that evanescent wave amplification at longer imaging distances arises primarily from the excitation of resonant modes within the SNG slab itself.

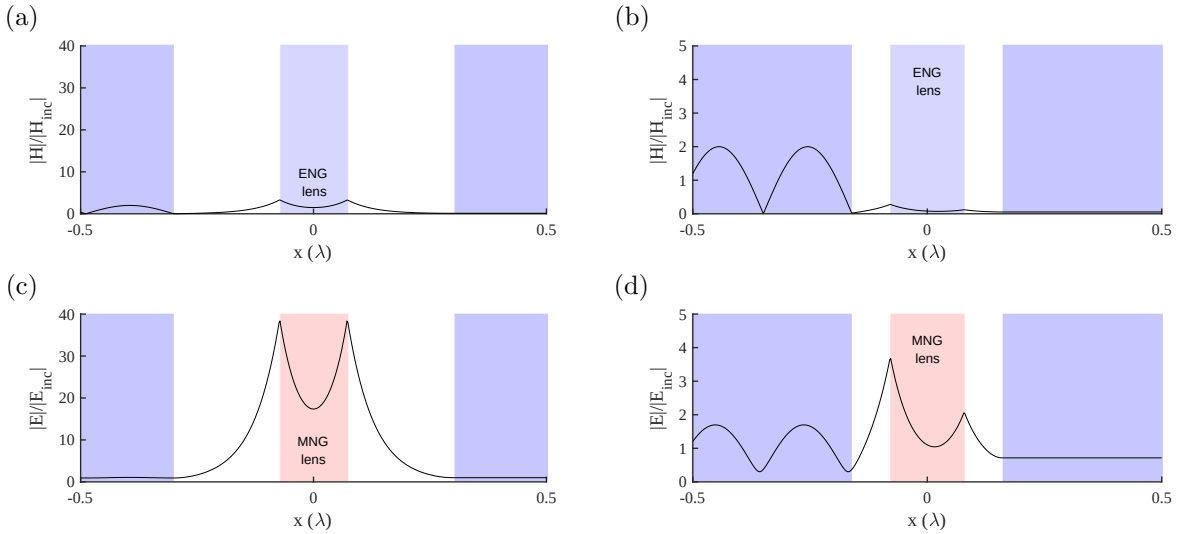

Figure 3.8: Normalized electric and magnetic field magnitude cross-section plots through the five-layer ENG and MNG configurations for spectral component $\beta = 3k_0$. Plots (a) and (c) show ENG and MNG configuration field cross-sections at a sample imaging distance of $D = 0.6\lambda$ and lens thickness of $d/D = 0.2422$ ($d = 0.1453\lambda$). This imaging configuration is chosen to satisfy the resonance condition in (3.14) for an isolated slab in free-space. Plots (b) and (d) show ENG and MNG configuration field cross-sections at a sample imaging distance of $D = 0.32\lambda$ and lens thickness of $d/D = 0.4925$ ($\delta = 0.0812\lambda$). This imaging configuration is chosen to satisfy the resonance condition in (3.20) for the air-gap between the dielectric and SNG lens in a three-layer system. Regions are distinguished by color: dark blue indicates the dielectric regions, light blue the ENG lens, and light red the MNG lens. Each lens configuration in this figure is marked with a red cross on the Fig. 3.6 surface plots.

Next, in Figs. 3.8(b) and 3.8(d) we compare field cross-sections through the ENG and MNG lensing configurations for an imaging distance and relative lens thickness of $D = 0.32\lambda$ and $d/D = 0.4925$, respectively. These dimensions correspond to the leftmost markers in Fig. 3.7, and are chosen to provide an example of configurations which satisfy the gap resonance condition in (3.20). Examining the field cross-sections, we see that both lenses display asymmetric field profiles, with a higher amplitude surface wave excited on the front lens interface. In addition, we can see that the MNG lens excites a much higher amplitude surface wave than the ENG lens, indicating, again, that evanescent wave amplification within the object-lens gap is polarization dependent. This is consistent with the polarization dependence predicted by (3.22) and (3.21).

Let us compare the plasmon amplitude of each five-layer imaging system with the amplitude predicted by the three-layer model using (3.21) and (3.22). The free-space gap length in Figs. 3.8(b) and 3.8(d) is $\delta = D/2 - d/2 = 0.0812\lambda$, which is the length that satisfies the resonance condition in (3.20) for the spectral component $\beta = 3k_0$. The field intensity at the first interface of the five-layer ENG lens system is $|H|/|H_{\text{inc}}| = 0.277$ while the field intensity at the first interface of the five-layer MNG lens system is $|E|/|E_{\text{inc}}| = 3.67$. By comparison, the field intensity of a plasmon excited through a three-layer system with the same gap can be calculated as $|t_{\text{s}}| = 0.234$ and $|t_{\text{p}}| = 3.74$ for the ENG lens and MNG lens, respectively. The MNG amplitudes agree within 1.9%, providing further evidence that the object-lens gap resonance is the driving mechanism for wave amplification for this imaging configuration. The higher amplitude plasmon on the first interface excites a higher amplitude plasmon on the second interface, ultimately increasing overall amplification at the image plane.

3.8 Imaging Analysis Results

To conclude our external resonance analysis, we investigate the imaging performance of dielectric-embedded ENG and MNG superlenses. A super-resolution image is generated by transmitting

spectral components beyond the free-space cut-off and restoring their amplitude and phase at the image plane. This requires the amplification of evanescent waves, whose high transverse spatial frequencies carry the small detail information. We have shown in Sec. 3.7 that modelling the object and detector interactions with dielectric half-spaces introduces a secondary amplification mechanism that has the potential to enhance imaging performance. This is particularly relevant for imaging systems using MNG lenses. In this section, we explore the feasibility of forming super-resolved images using such an MNG lens configuration and show that the MNG lens can operate over larger imaging distances and is more robust to loss than the ENG lens, whether the object and detector interactions are accounted for in the ENG lens system.

To better assess the superlensing capabilities of SNG lenses placed between dielectric object and image regions, we examine the mean and standard deviation of the transmission coefficient, $t(\beta, d, D)$, over a transverse spatial frequency range of $-4k_0 \leq \beta \leq 4k_0$ for both the ENG (Fig. 3.9(a)) and MNG (Fig. 3.9(b)) lens configurations. For a high performance superlens operating at a given lens thickness and imaging distance, these plots would exhibit a mean close to unity and a standard deviation close to zero, indicating restoration of each spectral component at the image plane. Furthermore, a region of unity mean and zero standard deviation that is located further to the right in the plot would indicate the capability for super-resolution imaging over longer imaging distances.

Figure 3.9(a) shows that ideal lens operation for the ENG system is confined to a thin vertical strip near $D = 0$ which protrudes outwards slightly around $d = 0.47D$. There does exist a narrow region of low standard deviation which extends towards 0.3λ, however the mean transmission drops off rapidly with increasing distance and is extremely sensitive to lens thickness. By contrast, Fig. 3.9(b) shows that the MNG lens system exhibits ideal lens operation over much larger imaging distances than the ENG lens system, with improved resiliency to variations in lens thickness. Here, the region of low standard deviation and high mean transmission

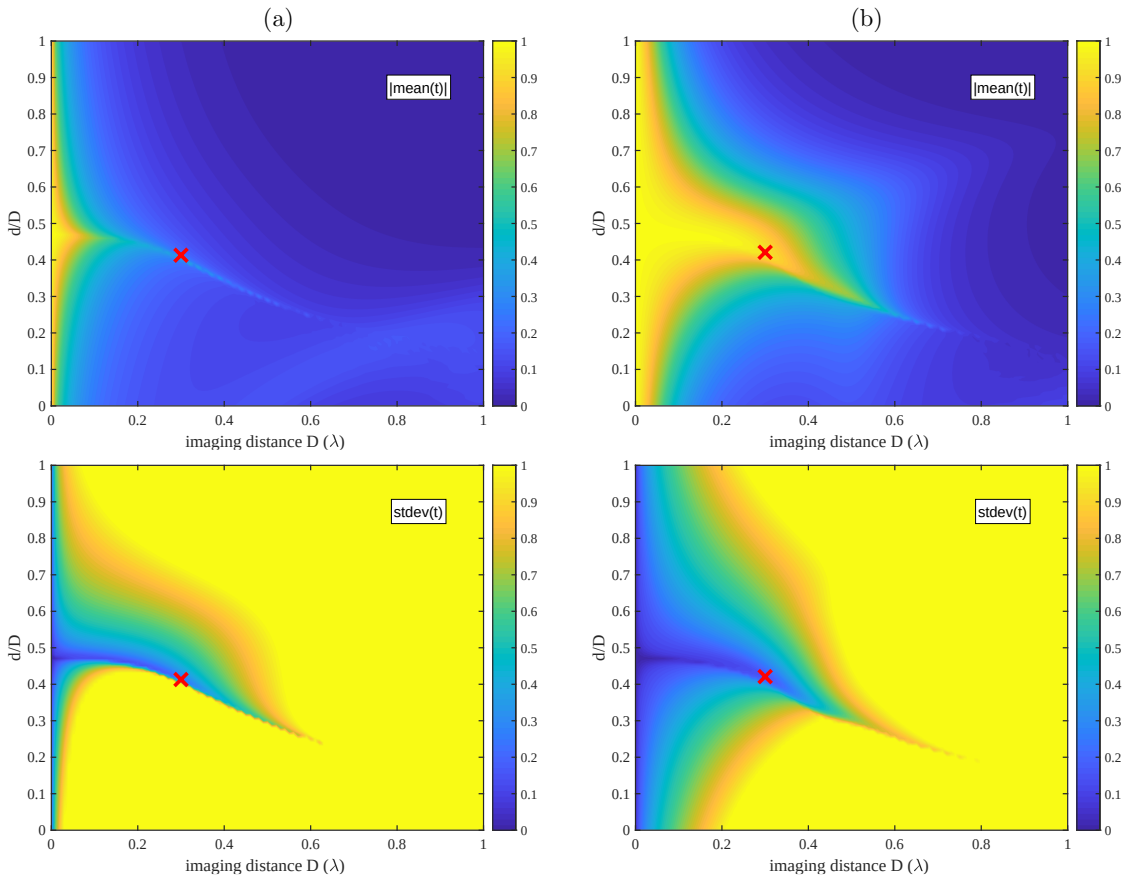

Figure 3.9: (The (top) mean and (bottom) normalized standard deviation (stdev) of transmission calculated over $-4k_0 \leq \beta \leq 4k_0$ for (a) the ENG lensing system and (b) the MNG lensing system. The red marker indicates the lens thickness for peak imaging performance at an imaging distance of $D = 0.3\lambda$. This corresponds to a lens thickness of $d = 0.4102D$ for the ENG lens and $d = 0.4202D$ for the MNG lens.

is much broader and extends out towards an imaging distance of 0.4λ. If we consider a specific demonstrative imaging distance of $D = 0.3\lambda$, we can select the optimal ENG and MNG lens thicknesses by choosing the point displaying the transmission coefficient with the minimum standard deviation. Given this optimization procedure, the optimal ENG and MNG lens thicknesses are $d = 0.4102D$ and $d = 0.4202D$, respectively (see the red markers in Figs. 3.9). For these lens configurations, the ENG system transmission has a mean of 0.28 and standard deviation of 0.24, while the MNG lens has a mean of 0.93 and standard deviation of 0.15. The higher mean and lower standard deviation of the MNG lens transmission response over the ENG lens implies a higher quality imaging performance.

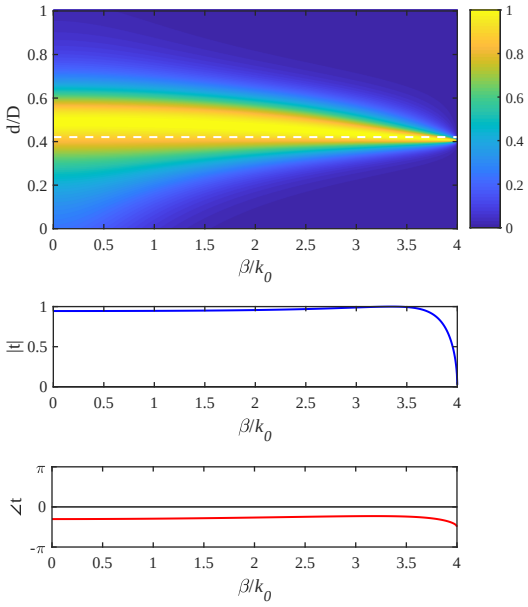

Figure 3.10: Transmission through an MNG lens ($\mu = -1$) placed between two dielectric regions ($n = 4$) separated by 0.3λ. The real part of the transmission coefficient is plotted as a function of slab thickness and transverse wave vector. The transmission magnitude and phase corresponding to the lens thickness $d/D = 0.421$ (indicated by the dashed white line) is plotted in the cross-sections below.

We further analyze the imaging capabilities of the MNG lens configuration by examining its performance at an imaging distance $D = 0.3\lambda$. In Fig. 3.10, we plot the transmission coefficient, t, as a function of the lens thickness over the spectrum $0 \leq \beta \leq 4k_0$. The optimal lens thickness for maximum transmission varies slightly for each individual spatial frequency, however as previously, we can choose an optimal imaging thickness by selecting $d/D = 0.4202$ which provides the minimum transmission standard deviation over the spectrum of interest. The magnitude and phase of the transmission coefficient at this lens thickness is plotted in the Fig. 3.10 cross-sections below the transmission surface to highlight the flat, near-unity transmission profile of the MNG lens system.

Let us now compare the super-resolution imaging capabilities of ENG and MNG lenses, where object and detector interactions are both accounted for and not accounted for. In Sec. 3.1, we introduced planar dielectric object and image half-spaces to model the presence of a source object and image detector. We also showed that these half-spaces ensure real power is

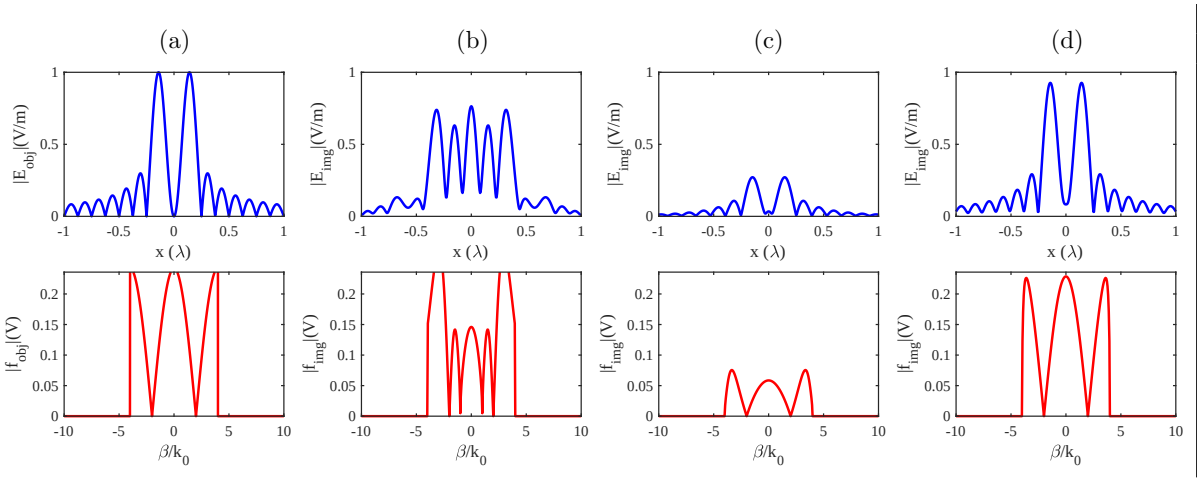

Figure 3.11: a) Two point sources with quarter wavelength separation imaged through b) an isolated ENG lens, c) an ENG lens placed between two dielectric half-spaces ($n = 4$), and d) an MNG lens placed between two dielectric half-spaces ($n = 4$). In all three cases the imaging distance is 0.3λ and the lens thickness is optimized to provide the flattest spectral transfer function.

transferred through the imaging system. In keeping with this principle of real power flow, we construct a band-limited object field from two sinc functions spaced a quarter wavelength apart (see Fig. 3.11(a)),

$$\mathbf{E}_{\text{obj}} = \text{sinc}((x - \text{s}/2)2\sigma) + \text{sinc}((x + \text{s}/2)2\sigma). \tag{3.24}$$

Here, $\text{sinc}(x) = \sin(x/(\pi x))$, $s = 0.25\lambda$ is the peak separation distance, and $\sigma \approx 0.4429$ designates a full-width half-maximum (FWHM) beam width of 0.1508λ which corresponds to a spectrum of $-4k_0 \leq \beta \leq 4k_0$ for each sinc function.

The object spectral distribution is multiplied by the system transfer function to get the image spectral distribution, which is converted to the image field using an inverse Fourier transform. Applying a spatial Fourier transformation to (3.24), the object spectrum (see Fig. 3.11(a)) can be expressed as

$$f_{\text{obj}} = \text{FFT}(E_{obj}) \\ = \frac{1}{\sigma}\cos\left(\frac{\beta s}{2}\right)\left(\left|\frac{\beta}{k_0}\right| < \sigma\right). \tag{3.25}$$

(E_{obj}), object spectrum (f_{obj}), image field (E_{img}) and image spectrum (f_{img}) are plotted for all three lensing systems in Fig. 3.11. In Fig. 3.11(b) we see that the fields from the isolated ENG lens are not resolved into two distinct peaks. Instead, spatial frequencies corresponding to the resonant mode of the lens are over-amplified, resulting in a standing-wave artefact that obscures the object image. In Fig. 3.11(c), the ENG lens is placed between two dielectric half-spaces representing the object and detector. The imaging artefacts from Fig. 3.11(b) disappear, however high attenuation through the lens results in low field intensity at the image. By contrast, if we examine Fig. 3.11(d), we see that placing an MNG lens between a dielectric object and detector generates a faithful reconstruction of the object field, with two well-resolved peaks confirming super-resolution imaging at a distance of 0.3λ. In this image, the difference between the object and image fields comprise a 7% drop in peak amplitude, a 2% increase in FWHM beam width, and an increase in the field minimum between the two peaks from 0% to 8% of the peak object field strength. Further reducing the two-object spacing, we find that the minimum resolvable separation distance by the dielectric-MNG lensing system is a gap of approximately 0.195λ. We define our resolution threshold where the minimum between image field peaks is $1/\sqrt{2}$ times the image peak value.

Let us continue our imaging analysis by investigating the effect of loss on lens performance to determine whether the presence of multiple independent amplification mechanisms increases the robustness of the system. A loss analysis also provides a more realistic evaluation of the potential resolution limits of a real-world SNG imaging system. Let us consider a similar imaging setup to the one used in the Fig. 3.11 simulations, but increase the object field complexity by observing now a three-source object represented by three sinc functions. The three sinc functions are once again given a FWHM of 0.1508λ, and are spaced at quarter

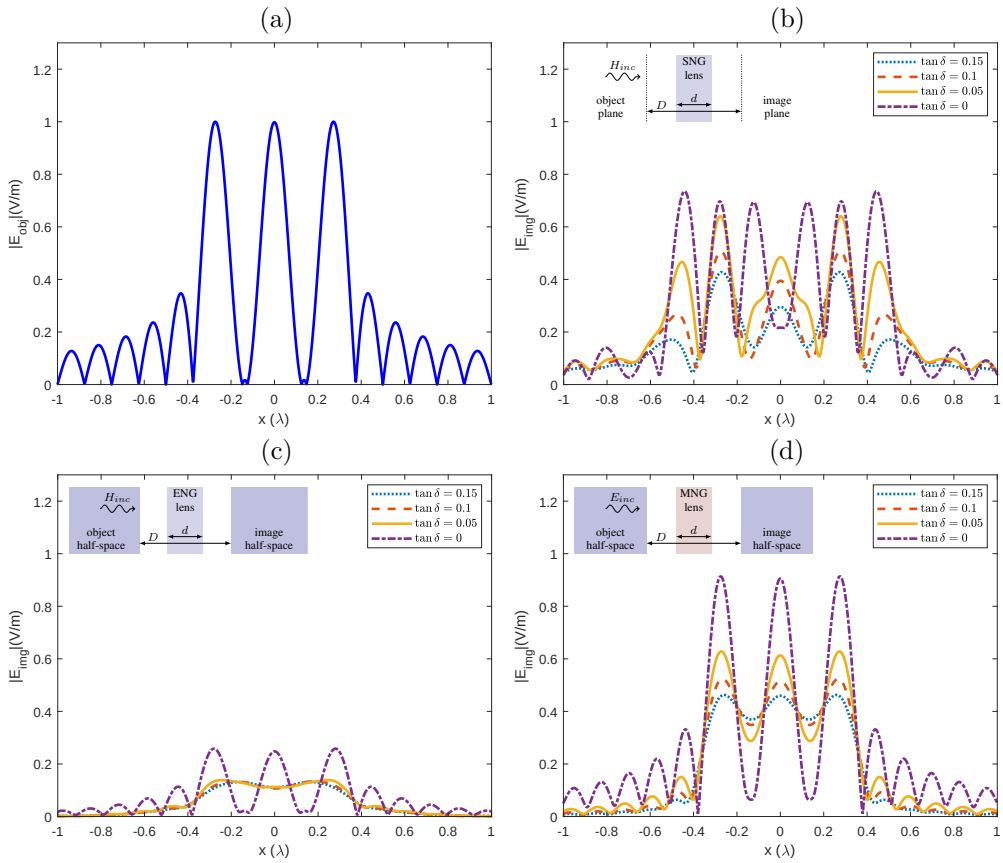

Figure 3.12: The imaging response of the single-negative lensing systems under conditions of increasing loss. a) Three point sources with an adjacent separation distance of 0.25λ imaged through b) an isolated ENG lens, c) an ENG lens placed between two dielectric half-spaces ($n = 4$) , and d) an MNG lens placed between two dielectric half-spaces ($n = 4$). For each lensing configuration the object and image are separated by a distance of 0.3λ. The imaging response is shown for loss tangents of 0, 0.05, 0.10, and 0.15.

wavelength intervals, as shown in Fig. 3.12(a). Figures 3.12(b), (c) and (d) show the imaging responses for an isolated ENG lens, an ENG lens embedded within a dielectric imaging system with $n = 4$, and an MNG lens embedded within a dielectric imaging system with $n = 4$, respectively. Furthermore, the imaging response of each lens is compared for the lossless case as well as loss tangents of $0.05, 0.1$, and 0.15. The upper end of this range is consistent with loss tangents reported in the recent metamaterial superlens literature [16, 15, 57]. As previously, the thickness of each lens is selected by minimizing the standard deviation of the spectral transfer function to provide the flattest response.

Examining Fig. 3.12(b) we see that once again spectral over-amplification from the isolated ENG lens generates additional field peaks that obscure the image. Here, imaging artefacts for the 0.05, 0.1, and 0.15 loss tangent cases manifest as side lobes with levels reaching 95%, 67%, and 58% of the center image peak field strength, respectively. This result demonstrates how imaging with an isolated SNG lens relies on loss; the lossless and low loss cases generate unresolved images, with only the 0.15 loss tangent case being capable of generating an image that resembles the object field. If we embed the ENG lens within a dielectric imaging system, as shown in Fig. 3.12(c), the imaging artefacts are eliminated, but overall transmission is again reduced such that the object-field peaks are no longer distinguishable at the image for any case other than the lossless case. The Fig. 3.12(d) imaging response shows that an MNG lens embedded within a dielectric imaging system provides the most reliable imaging response. While the inclusion of lens loss does reduce overall MNG lens transmission, the imaging configuration is still able to resolve the three object peaks for loss tangents below 0.15. (The 0.15 case does not meet our strict definition of resolution, however the peaks are still visually distinct.)

Our imaging results verify that resonant evanescent wave amplification within the free-space cavity not only boosts transmission across the imaging spectrum to improve the imaging performance of an MNG lens, but it also increases image resiliency to lens loss. The ability of the MNG lensing configuration to provide super-resolution imaging that is robust to loss can be attributed to the resonant amplification of evanescent waves that occurs within the free-space gap between object and lens. Since this amplification mechanism occurs prior to transmission through the lens, it is impacted less by the introduction of lens loss than the dominant, slab-resonance amplification mechanism.

Chapter 4

Finite Lens Effects

In this Chapter, we present the methods we developed to study the frequency characteristics of dispersive, finite transverse-width superlenses, and showcase how geometry tuning can be used to improve superlensing performance. In standard theoretical superlensing analysis, the lens is typically assumed to be a flat, planar slab with a finite-thickness, but an infinite width in both transverse directions. The consideration of a finite transverse dimension greatly complicates superlens analysis, requiring two-dimensional simulation techniques (as opposed to one-dimensional), and introducing corner interactions that can disrupt the lens response. In this section of the thesis, we develop methods to analyze how superlens geometry affects resonant surface plasmon excitation and superlensing performance.

Finite transverse-width superlensing research has been focused on improving finite-difference time-domain (FDTD) simulation techniques [33], exploring the imaging performance of non-dispersive superlenses with $\Re(\varepsilon_r) = \Re(\mu_r) = -1$ [32, 33], and investigating the temporal characteristics of double-Drude lenses [34]. In a 2019 study, authors Aghanejad et al. simulated a two-dimensional, dispersive, heterogeneous DNG superlens structure that had a finite thickness, and finite width in one transverse direction [39]. In this study, Aghanejad et al. observed that the continuous resonant modes of an infinite width superlens become discrete when the lens has a finite transverse width. By carefully choosing the width of the lens, its discrete resonances could be shifted to avoid excitation at the operating frequency. In our work, we develop simulation and processing techniques to study the dispersive characteristics of finite width DNG and SNG superlenses. We expand on previous work in the area by providing a framework for analyzing the finite width superlens response to individual Fourier components, and demonstrating how lens geometry tuning can modify resonances to improve the imaging

response of dispersive superlenses.

4.1 Simulation Model

To analyze finite width superlens characteristics, we propose a model to be simulated using COMSOL Multiphysics' frequency-domain electromagnetic wave solver. In this analysis, we normalize all lens geometries and frequency components by the wavelength at which $\varepsilon_r = -1$ and/or $\mu_r = -1$. This wavelength will be labeled λ_{op} and is typically used as the operating point for matched double-Drude lenses. Our simulation model, shown in Fig. 4.1, consists of a two-dimensional superlens slab with circularly shaped corners, that is placed within a free-space region, and bounded by a perfectly matched layer (PML). The superlens geometry is characterized by a thickness, d, a width, w, and a corner radius, r. To model dispersive lens material parameters, we use lossless Drude models in one or both of μ or ε. Here, it should be noted that it is not necessary to introduce material losses to the superlens for the purpose of avoiding singularities in the field amplitudes as scattering from the lens corners generates loss to the resonant modes.

In our simulations, we excite the lens with individual incident Fourier components of the form

$$E_z = 100e^{-jk_{xn}(x+d/2)-j\beta_n y}, \tag{4.1}$$

where $\beta_n = \beta/\beta_{op}$ is the normalized transverse spatial frequency of the wave and $k_{xn} = k_x/k_{op}$ is the normalized longitudinal spatial frequency. This wave equation is designed to have a unity amplitude at the first lens interface, located at $x = -d/2$, to minimize the impact of varying amplitude decay rates between spectral components. In other words, all incident evanescent waves have unity amplitude at the first lens interface, regardless of the component's decay rate.

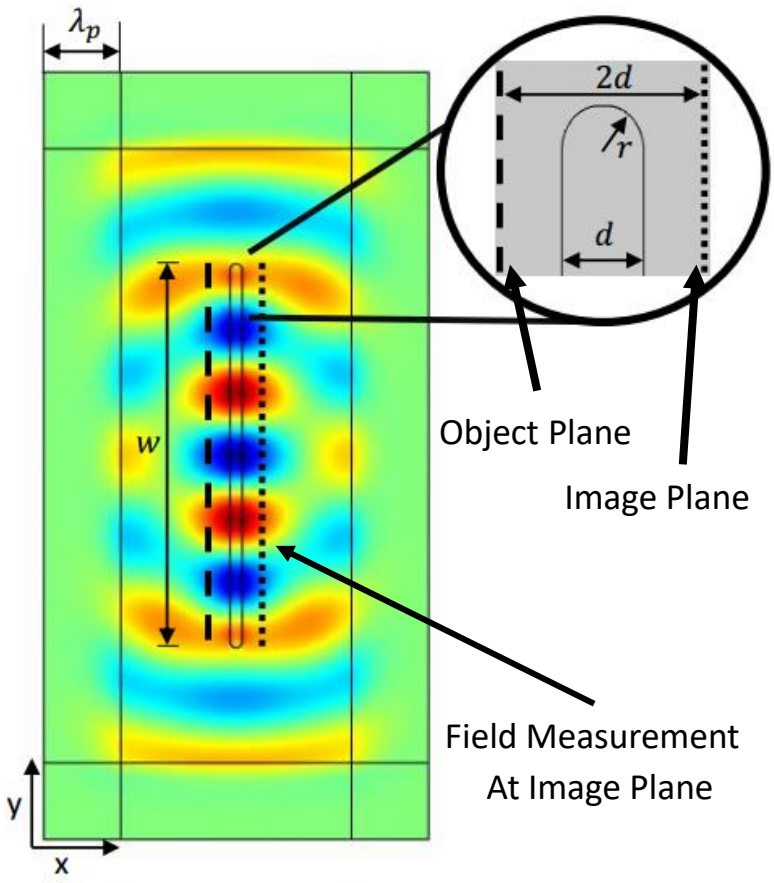

Figure 4.1: Simulation model of a curved corner, finite transverse width superlens within a free-space simulation region. Perfectly matched layers of width $\lambda_p = \lambda_{op}/\sqrt{2}$ bound the simulation space to absorb scattered radiation. The lens has a width w, thickness d, corner radius r. The object plane is shown as a vertical dashed line that is located at $x = -d$, and the image plane is a vertical, dotted line that is located at $x = d$. A sample scattered field is overlaid as a red and blue surface pattern.

4.1.1 Addressing Evanescent Wave Simulation Challenges

Simulation of the evanescent wave components required for superlensing comes with a number of challenges. First, the phase of evanescent waves rapidly vary in the direction transverse to their decay. The precise measurement of these rapidly varying fields requires implementation of a fine enough mesh grid to avoid aliasing. In our simulation, the spatial sampling of all electromagnetic wave components is kept well above the Nyquist rate, with dynamic meshing employed along the lens corners to effectively capture corner curvature detail. However, while increased spatial sampling enables higher transverse spatial frequency simulation, it also increases simulation time. Therefore, to avoid excessive simulation times, we also constrain our simulation range to a maximum transverse spatial frequency of $\beta_n = 2.27$.

Second, evanescent wave amplitude decay can introduce unwanted numerical artefacts to the simulation. In our system, we define the incident evanescent wave components such that their amplitude exponentially decays as they travel along the positive x direction. When the decay constant is large, the incident field at the left simulation boundary can be many orders of magnitude larger than that of the incident field at the right simulation boundary, with the field at the lens being somewhere in between. In such cases, scattering off of the left PML interface can dominate the scattered field. To mitigate this potential source of error, the left boundary is placed near to the lens, thereby reducing the dynamic range of incident evanescent wave components.

4.2 Evaluating Finite Width Superlens Spectral Transmission

4.2.1 Simulation and Processing Methods

With the simulation configured, we evaluate the spectral transmission characteristics of finite width superlenses. To begin, we define the incident electromagnetic wave as a background field in COMSOL Multiphysics, allowing the lens response to be isolated by directly measuring the simulated scattered field data. To gather lens transmission data over both temporal and spatial

frequency domains, we sweep the temporal frequency, $\omega_n = \omega/\omega_{op}$, and transverse spatial frequency, $\beta_n = \beta/\beta_{op}$, of the incident electromagnetic wave over a region of the evanescent regime, $\{\omega_n \in \Re \mid [0.73, 1.14]\}$, $\{\beta_n \in \Re \mid [1, 2.27]\}$. For each increment within this sweep, we sample the complex scattered field data at 4001 equally spaced points placed along the image plane between $y = -w$ and $y = w$. In this manner, we collect one-dimensional data representing the amplitude and phase of the transmitted field for each given incident spectral component (see Fig. 4.2(b)).

Once the real-space field data has been gathered, we generate the spectral response of the lens by converting to the spatial frequency domain using a fast Fourier transform (FFT). To increase spatial frequency domain signal resolution, we zero-pad the field data prior to applying this transformation, artificially boosting the number of spatial samples to 131072 points. To illustrate this step, we plot a sample real-space field signal and its corresponding amplitude spectrum for a $\beta_{ni} = 2$ incident wave component transmitted through an arbitrary finite width superlens in Figs. 4.2(a) and 4.2(c), respectively. Examining Fig. 4.2(c), we see that the maximum spectral peak of the transmitted spectrum is located at the transverse spatial frequency of the incident wave, β_{ni}. The plotted spectral transmission response also shows strong amplification of Fourier components other than that of the incident. After viewing the image fields for a number of different incident waves, we observed that there most often appears four main spectral peaks, centered around $\pm\beta_{ni}$ and $\pm k_0$, where k_0 is the spectral cut-off spatial frequency.

To simplify our analysis of finite width superlens transmission, we approximate the image plane spectrum by modelling its four main spectral peaks. Due to the finite extent of the lens, it can only act on the incident wave over a finite region. Since the incident wave is infinite in extent, we must therefore introduce a windowing function to our transmission model. Here, we show that the convolution between each main spectral component and a rectangular window function with a width equal to that of the lens can provide a good approximation for

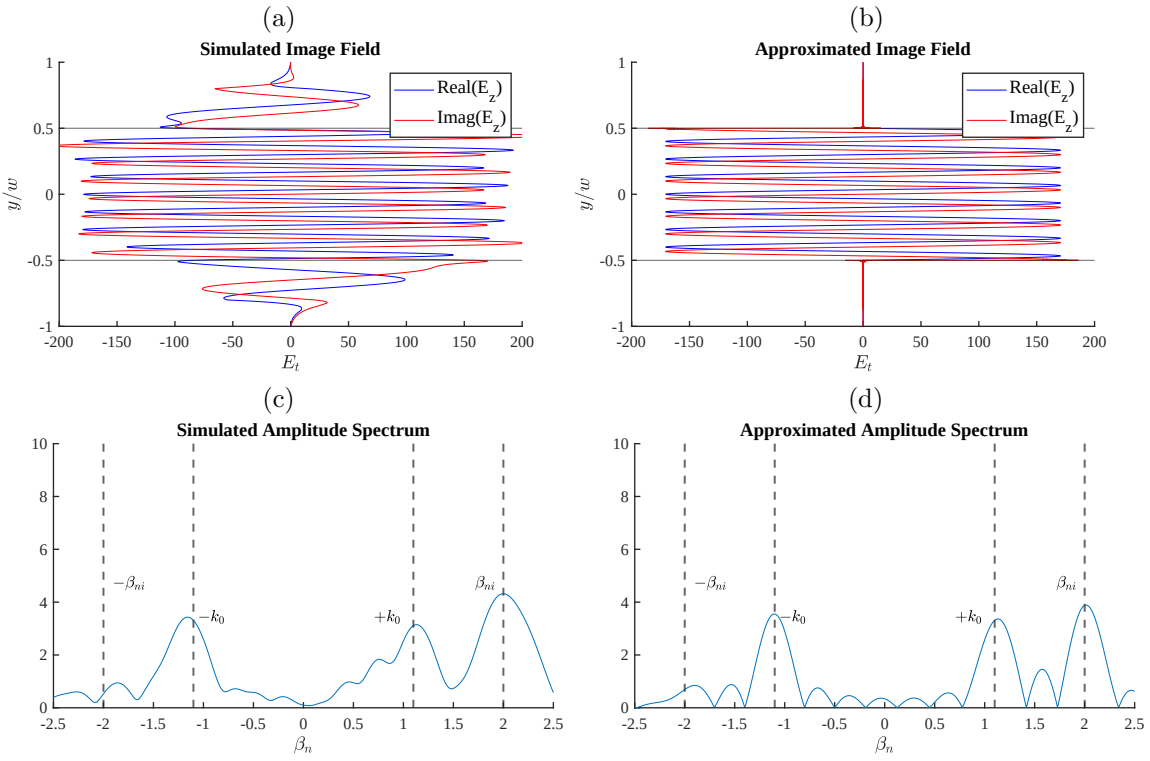

Figure 4.2: **Top row:** Sample simulation plots of the real (red) and imaginary (blue) components of (a) the transmitted electric field measured at the image plane and (b) an approximation of the transmitted electric field measured at the image plane. **Bottom row:** Sample amplitude spectrum of (c) the simulated electric field as measured at the image plane, and (d) an approximation of the four main spectral peaks of the simulated spectrum. All plots are for a single-Drude lens with a thickness of $d = \lambda_{op}/(2\sqrt{2}\pi)) \approx 0.11\lambda_{op}$, corner radius of $r = 0.45d \approx 0.051\lambda_{op}$. Vertical dashed lines indicate the locations of free-space cut off spatial frequencies $\pm k_0$, as well as the incident spectral component spatial frequency $+\beta_{ni}$ and the negative incident spectral component spatial frequency $-\beta_{ni}$.

the transmitted field spectrum. The lens defining window function can be expressed as

$$t_{model}(y) = \begin{cases} 0, & \text{if } |y| > w/2 \\ 1, & \text{if } |y| \leq w/2, \end{cases} \tag{4.2}$$

where the bounded transverse width, $|y| \leq w/2$ matches that of the lens. Performing a Fourier transformation on eq. (4.2), we convert this lens model to the spatial frequency domain, generating a weighted sinc function of the form,

$$T_{model}(\beta_n) = w \,\mathrm{sinc}\left(w\frac{\beta_n - \beta_{ns}}{2\pi}\right), \tag{4.3}$$

for each spectral component, where, T_{model} corresponds to the modelled spectrum, and β_{ns} is the normalized transverse spatial frequency of the considered spectral component. Applying this transmission model to the $\pm\beta_{ni}$ and $\pm k_0$ components, we generate four sinc functions that appear centered at their respective normalized spatial frequencies. Comparing Fig. 4.2(c) and 4.2(d) we show how the superposition of these four convolved spectral components can be used to model the simulated amplitude spectrum. Here, we observe that the spectral beamwidth of each simulated component appears consistent with that of the modelled lens convolution. By scaling the sinc functions to best fit our simulated spectrum data, we can approximate the height of each component's spectral transmission peak,

$$T_{sim} \approx T_{model} T_s, \tag{4.4}$$

where T_{sim} corresponds to the simulated transmitted spectrum, and T_s is the applied complex multiplier. Here, the modifier T_s represents amplification of each individual spectral component. We discretize T_{model} and T_{sim} into $[\mathrm{M} \times 1]$ matrices consisting of M spectral points, then, using a least squares algorithm to optimize for T_s [58], we convert the simulated lens transmission response into complex numbers corresponding to each spectral component's transmission,

$$T_s = (\mathbf{T_{model}}^T \mathbf{T_{model}})^{-1} (\mathbf{T_{model}}^T \mathbf{T_{sim}}). \tag{4.5}$$

4.2.2 Double-Drude Transmission Response

Applying the technique developed in Sec. 4.2.1 to each of the $\pm\beta_{ni}$ and $\pm k_0$ spectral components for a range of incident waves allows us to characterize the lens transmission response. In Fig. 4.3 we plot the magnitude of the transmission coefficient, $|T_s|$, corresponding to $\pm\beta_{ni}$ and $\pm k_0$ spectral components over spatial and temporal frequency for a sample finite width, matched double-Drude superlens. (See Figure caption for the geometry.) In each plot within this Figure, we see high transmission regions, shown in red, that closely align with the overlaid black curves representing the analytical surface plasmon resonances for an infinite width, double-Drude lens. These high transmission regions indicate that the surface plasmon resonances of a finite-width superlens are discretized along the resonant solutions for an infinite-width superlens. Next, for the incident, β_{ni} component, we see a horizontally aligned near-unity (0 dB) transmission region surrounding the matched frequency, ω_{op}. For the $-\beta_{ni}$, $+k_0$ and $-k_0$ spectral components, this horizontal frequency band shows low transmission, indicating that the operating frequency should provide a good imaging response for the incident component, with low amplification of unwanted additional spectral components. However, just below the matched frequency, at $\omega_n \approx 0.96$ we see a high transmission region for the three non-incident component plots. Operation near this temporal frequency would risk generating amplifying these components, generating artefacts that could obscure the image.

We now focus our investigation on transmission of the incident spectral component, $+\beta_{ni}$. We limit our investigation to this single component as it most clearly shows the resonances of the lens. To study how lens geometry affects resonance, let us first consider the matched double-Drude lens, defined by material parameters

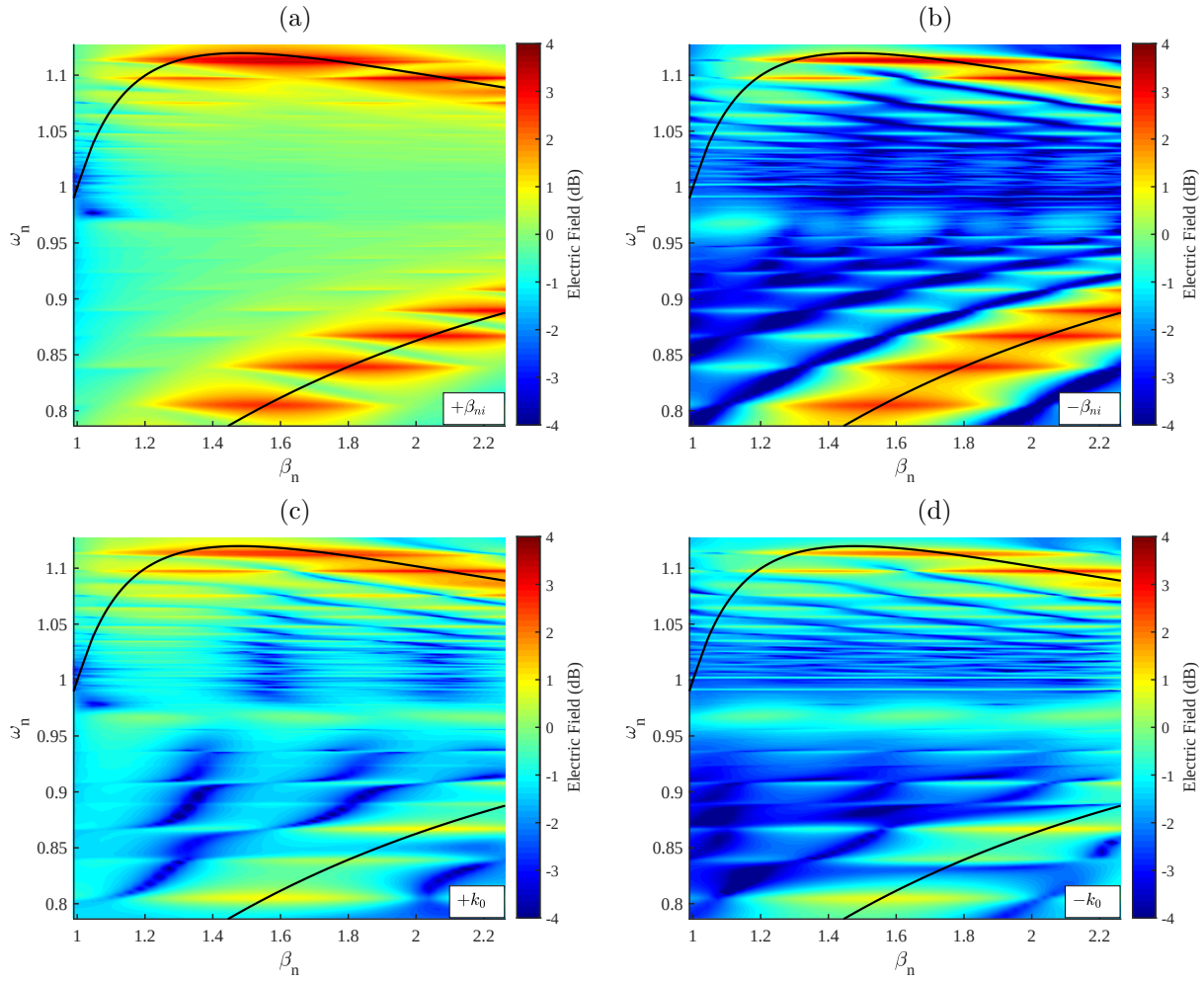

Figure 4.3: Plots in dB of the transmission of spectral components **(a)** $+\beta_{ni}$, **(b)** $-\beta_{ni}$, **(c)** $+k_0$ and **(d)** $-k_0$ through a sample double-Drude lens ($\omega_{p\varepsilon} = \omega_{p\mu}$) with a thickness of $d = \lambda_{op}/(2\sqrt{2}\pi) \approx 0.11\lambda_{op}$, corner radius of $r = 0.45d \approx 0.051\lambda_{op}$, and width of $w = 3\lambda_{op}/\sqrt{2} \approx 2.12\lambda_{op}$. The overlaid black curves present the resonant surface plasmon solutions for an infinitely wide superlens.

$$\varepsilon_r = \mu_r = 1 - \frac{(2\omega_{op})^2}{\omega^2}. \tag{4.6}$$

In Fig. 4.4 we plot incident spectral component transmission through two double-Drude lens geometries. Both lenses are defined by a thickness of $d = \lambda_{op}/(2\sqrt{2}\pi)) \approx 0.11\lambda_{op}$, and corner radius of $r = 0.45d \approx 0.051\lambda_{op}$, and differ only in width. In Fig. 4.4(a) we plot spectral transmission through a lens of width $w = 3\lambda_{op}/\sqrt{2} \approx 2.12\lambda_{op}$, while in Fig. 4.4(b) we plot spectral transmission through a lens of width $w = 5\lambda_{op}/\sqrt{2} \approx 3.53\lambda_{op}$. The chosen lens thickness of $d = \lambda_{op}/(2\sqrt{2}\pi))$ corresponds to $k_p d = 1$, where $k_p = 2\sqrt{2}\pi/\lambda_{op}$. This lens thickness is chosen both to be consistent with dimensions used in superlens designs [8, 39, 44], and to highlight individual resonance branch characteristics as at lens thicknesses above $d = 3\lambda_{op}/(4\pi\sqrt{2}) \approx 0.17\lambda_{op}$, the upper and lower resonance branches begin to merge, the individual branches becoming indistinguishable.

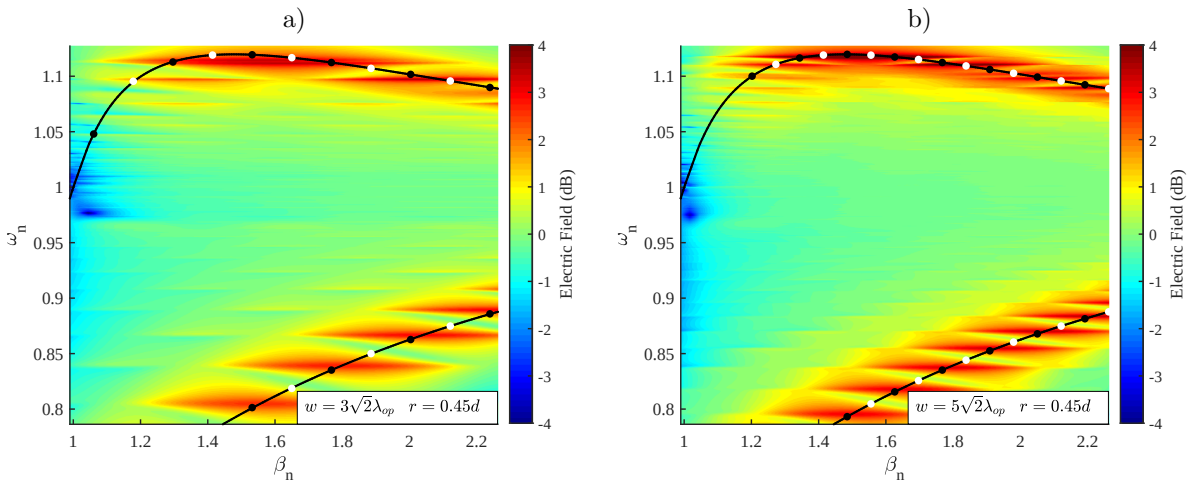

Figure 4.4: Plots in dB of the spectral transmission, $\log(|T_i|)$, through double-Drude lenses ($\omega_{p\varepsilon} = \omega_{p\mu}$) with a thickness of $d = \lambda_{op}/(2\sqrt{2}\pi) \approx 0.11\lambda_{op}$, corner radius of $0.45d \approx 0.051\lambda_{op}$, and a) a width of $w = 3\lambda_{op} \approx 2.12\lambda_{op}$, b) a width of $w = 5\lambda_{op} \approx 3.53\lambda_{op}$. Spectral transmission is calculated using the methods described in Sec. 3.5 over temporal frequency ($\omega_n = \omega/\omega_{op}$) and transverse spatial frequency ($\beta_n = \beta/\beta_{op}$). The overlaid black curves present the resonant surface plasmon solutions for an infinitely wide superlens, while the black and white markers locate the maxima and minima, respectively, of a one-dimensional cavity with a length matching that of the lens width.

Observing the transmission plot for a $w = 3\lambda_{op}/\sqrt{2} \approx 2.12\lambda_{op}$ wide lens in Fig. 4.4(a),

we see distinct resonant mode peaks, indicated by the high field regions in red, whose maxima closely align with the overlaid black curves representing analytical resonance dispersion for an infinite width, double-Drude lens. This observed resonant mode discretization is consistent with one-dimensional cavity model descriptions from prior finite width superlens studies [39, 34]. Under the cavity model description, partial standing surface waves are generated by reflections at the lens corners. These standing waves attain an amplitude maximum when the product of their transverse spatial frequency and the lens width is equal to an odd multiple of a quarter the transverse wavelength, and an amplitude minimum when the product of their transverse spatial frequency and the lens width is equal to an even multiple of a quarter the transverse wavelength,

$$\frac{\beta_n \omega_{op} w}{c} = \frac{\Gamma \pi}{2}, \tag{4.7}$$

where c is the speed of light in vacuum and Γ is a positive integer. Here, Γ specifies the maximum and minimum locations, for Γ odd and Γ even, respectively.

At the operating points where (4.7) is satisfied for odd Γ we expect to observe resonance maxima in our spectral transmission plots. Conversely, at the operating points where (4.7) is satisfied for even Γ we expect to see resonance minima. To observe how closely our finite width lenses follow this one-dimensional cavity description, we plot the predicted transmission maxima and minima locations as black and white markers, respectively, along the resonance branches in Fig 4.4. Observing these marker locations for Fig. 4.4(a), we see that the predicted maxima and minima locations closely align with the simulated spectral transmission modes of the lens. Comparing the spectral transmission response of the $w = 3\lambda_{op}/\sqrt{2} \approx 2.12\lambda_{op}$ wide lens in Fig. 4.4(a) with that of the $w = 5\lambda_{op}/\sqrt{2} \approx 3.53\lambda_{op}$ wide lens in Fig. 4.4(b), we see that increasing lens width result in a higher number of discrete resonance modes along each branch. The cavity model captures this increase in modal density, with the spacing of the predicted spectral maxima and minima similarly reducing along each resonance branch.

We now look to observe the effects of corner radius on resonant mode discretization. In Fig. 4.5 we plot spectral transmission through two $d = \lambda_{op}/(2\sqrt{2}\pi) \approx 0.11\lambda_{op}$, $w = 5\sqrt{2}\lambda_{op} \approx 3.53\lambda_{op}$ lenses. The lens in Fig. 4.5(a) is given a corner radius of $r = 0.45d \approx 0.051\lambda_{op}$ and the lens in Fig. 4.5(b) is given a corner radius of $r = 0.15d \approx 0.017$. Comparing these two plots, we see that the resonant modes of the Fig. 4.5(b) $r = 0.15d \approx 0.017$ lens are shifted down in both spatial and temporal frequency from those of Fig 4.5(a) $r = 0.45d \approx 0.051\lambda_{op}$ lens. This shift in modal placement results in closer alignment of the simulated resonances with the predicted maxima and minima locations from the one-dimensional cavity model. This result indicates that reducing lens corner radius increases the effective length of the one-dimensional cavity model for the lens. The sharper the lens corner, the closer the cavity model length is to the physical lens width. The resonances of lenses with rounder corners follow a distribution that better matches a shorter one-dimensional cavity.

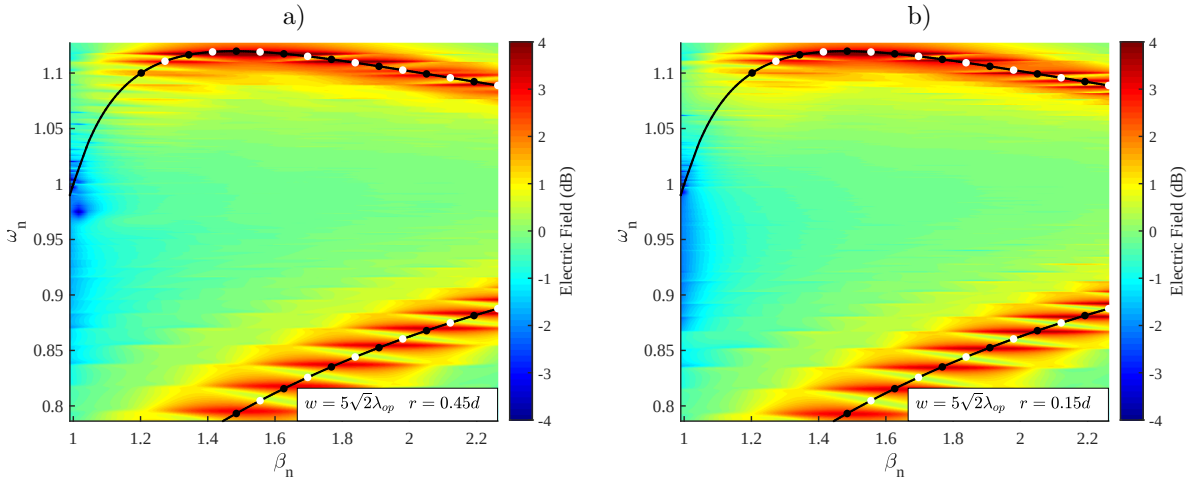

Figure 4.5: Plot in dB of the spectral transmission, $\log(|T_i|)$ of double-Drude lenses ($\omega_{p\varepsilon} = \omega_{p\mu}$) with a thickness of $d = \lambda_{op}/(2\sqrt{2}\pi)$, width of $w = 5\sqrt{2}\lambda_{op} \approx 3.53\lambda_{op}$ and (a) a corner radius of $0.45d \approx 0.051\lambda_{op}$, (b) a corner radius of $0.15d \approx 0.017\lambda_{op}$. Spectral transmission is calculated using the methods described in Sec. 3.5 over both temporal frequency and transverse spatial frequency. The overlaid black curves present the resonant surface plasmon solutions for an infinitely wide superlens, while the black and white markers locate the maxima and minima, respectively, of a one-dimensional cavity matching the lens width.

4.2.3 Double-Drude Transmission Performance

To gain an understanding of how lens geometry affects imaging performance, we study spectral transmission through a double-Drude lens operated at a normalized frequency of $\omega_n = 1$. By working at this perfect-lensing operating point, any deviation from a unity (0 dB) spectral transmission response can be directly attributed to finite width lens effects. In Fig. 4.6, the spectral transmission through three separate perfect lenses is plotted. All considered lenses are again given a thickness of $d = \lambda_{op}/(2\sqrt{2}\pi) \approx 0.11\lambda_{op}$, and differ only in lens width and corner curvature radius.

For this comparison, we plot the response of a $w = 3\sqrt{2}\lambda_{op} \approx 2.12\lambda_{op}$, $r = 0.45d \approx 0.051\lambda_{op}$ lens in blue, a $w = 5\sqrt{2}\lambda_{op} \approx 3.53\lambda_{op}$, $r = 0.45d \approx 0.051\lambda_{op}$ lens in red, and a $w = 5\sqrt{2}\lambda_{op} \approx 3.53\lambda_{op}$, $r = 0.15d \approx 0.017\lambda_{op}$ lens in yellow. All three lenses can be seen to display non-flat spectral transmission responses over the considered spatial frequency range. Here, the surface wave interference responsible for discretizing the surface plasmon resonances also adds transmission ripple to the perfect lens response. Comparing the transmission profiles of the $w = 3\sqrt{2}\lambda_{op} \approx 2.12\lambda_{op}$ and $w = 5\sqrt{2}\lambda_{op} \approx 3.53\lambda_{op}$ lenses, we see that increasing lens width generates more transmission fluctuation over the studied spatial frequency range. This observation is consistent with the cavity model description, which predicts more densely packed modes for longer one-dimensional cavities. In addition to transmission ripple, the lenses also exhibit upward sloping spectral amplification responses that increases from $T_i(\beta) \approx -1$dB near free-space cut off towards the left of the plot, to $T_i(\beta) \approx 0$dB at $\beta_n = 2.3$ visible towards the right of the plot.

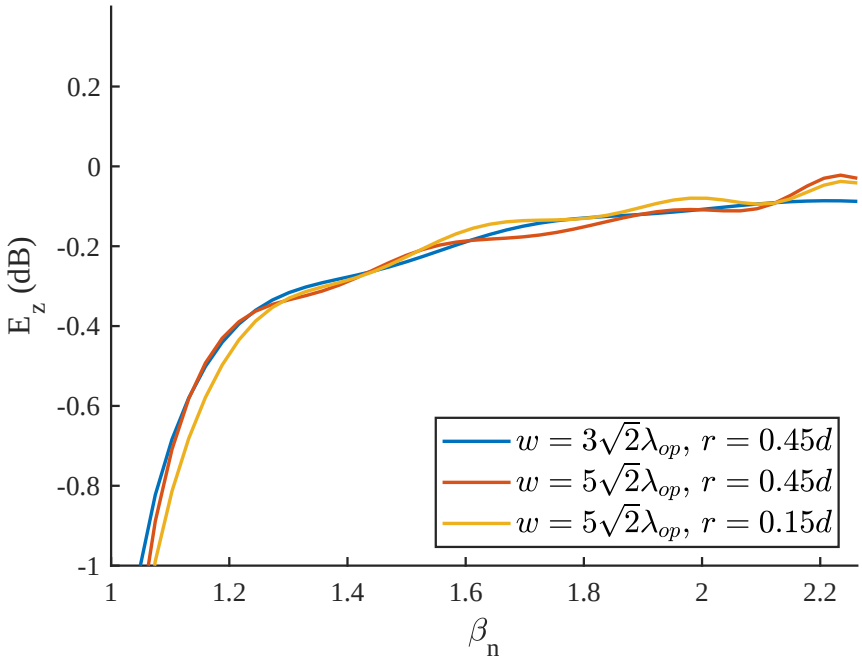

Figure 4.6: Spectral electric field transmission, $\log(|T_i|)$ (dB) along the ω_{op} matched frequency for the indicated double-Drude lens geometries. All lenses have thickness of $d = \lambda_{op}/(2\sqrt{2}\pi) \approx 0.11\lambda_{op}$ and differ only by width and corner curvature radius.

4.2.4 Single-Drude Lens Geometric Tuning

In their work, Aghanejad et al. observed that imaging artefacts could be avoided by adjusting the transverse width of heterogeneous, DNG, metamaterial lenses to avoid the excitation of resonant modes [39]. To expand on this work, we investigate the manner in which the geometric tuning of finite width superlenses modifies surface plasmon resonance to improve superlensing performance. To facilitate our analysis, we study field transmission through homogeneous, single-Drude lenses, defined by a dispersive permittivity and non-dispersive permeability. This homogeneous lens model provides a simpler response than that of the heterogeneous lens model used by Aghanejad et al. Additionally, as the single-Drude lens lacks a matched, $n = -1$ frequency point, any chosen operating frequency will necessarily intersect with a resonant branch (provided that the chosen operation frequency is below the maximum resonant temporal frequency of the lens). This necessary resonance excitation helps to better

showcase how geometric tuning can improve the superlens transmission response by reducing resonant component amplification.

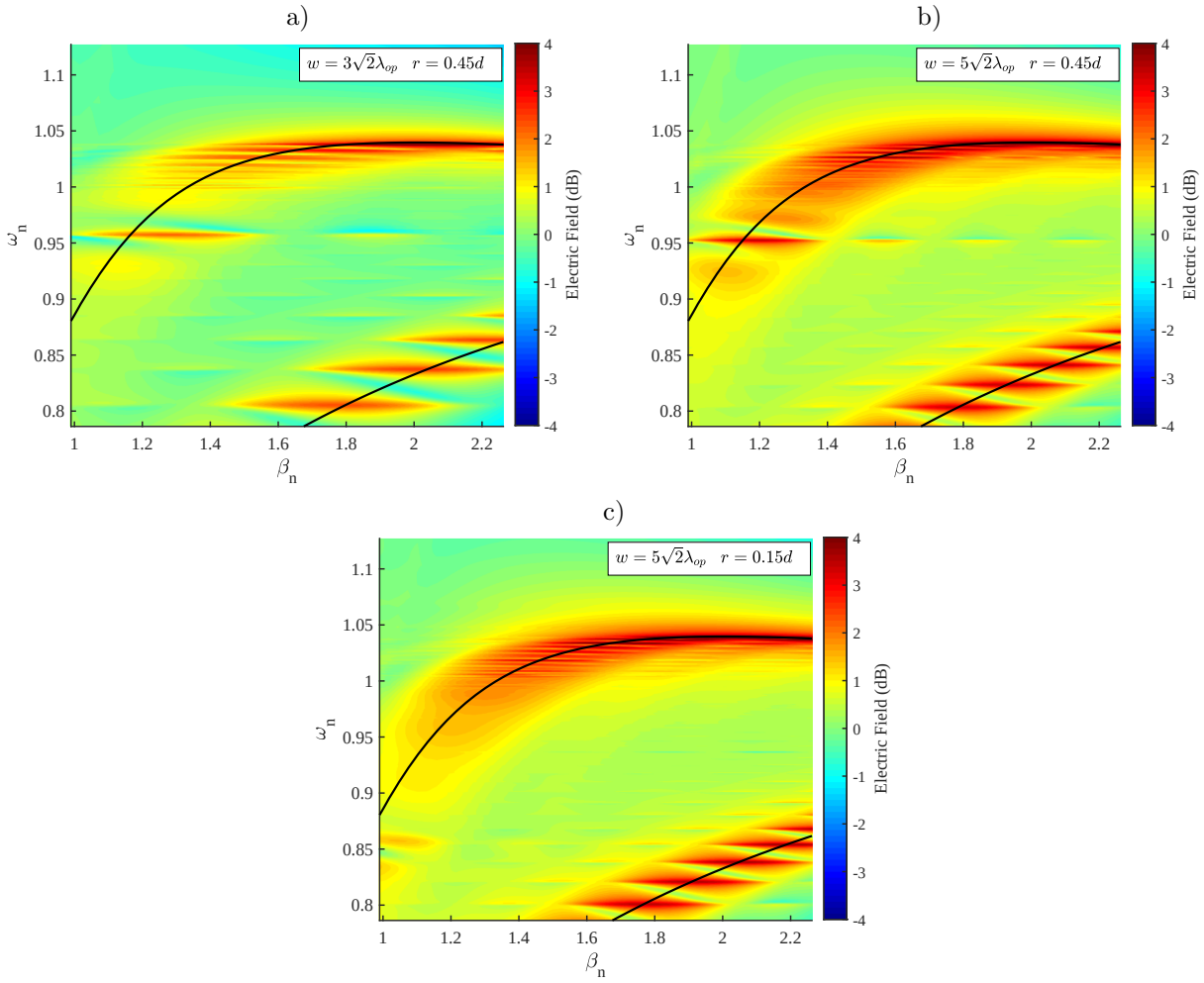

Figure 4.7: Electric field spectral transmission, $\log(|T_i|)$ (dB) along the ω_{op} matched frequency for the indicated double-Drude lens geometries. All lenses have thickness of $d = \lambda_{op}/(2\sqrt{2}\pi) \approx 0.11\lambda_{op}$ and differ only by width and corner curvature radius.

In Fig. 4.7 we plot spectral transmission surfaces for three separate single-Drude lens geometries. All considered lenses are again defined by a thickness $d = \lambda_{op}/(2\sqrt{2}\pi) \approx 0.11\lambda_{op}$, but differ in both lens width and corner curvature radius. Here, Fig. 4.7(a) plots the transmission through a $w = 3\sqrt{2}\lambda_{op} \approx 2.12\lambda_{op}$, $r = 0.45d \approx 0.051\lambda_{op}$ lens, Fig. 4.7(b) plots the transmission through a $w = 5\sqrt{2}\lambda_{op} \approx 3.53\lambda_{op}$, $r = 0.45d \approx 0.051\lambda_{op}$ lens, and Fig. 4.7(c) plots the transmission through a $w = 5\sqrt{2}\lambda_{op} \approx 3.53\lambda_{op}$, $r = 0.15d \approx 0.017\lambda_{op}$ lens. Ob-

serving each Fig. 4.7 plot, we first note that the discrete resonant modes of all three lens geometries, indicated by the high transmission regions in red, closely follow the overlaid black curves representing the resonant surface plasmon dispersion solutions for an infinitely wide lens. However, the nature of these resonances differ significantly between lens geometries. The lower branch resonances of each lens can be seen to manifest as individual modes. While these modes do become more densely packed over the lower resonance curve as lens width is increased, they still remain visually distinct for all lens geometries. In comparison, the resonant modes of the upper branch are much closer together, and appear to meld into a near-continuous high transmission region for the wider, $w = 5\sqrt{2}\lambda_{op}$ lens geometries.

Corner radius curvature also has a strong impact on the upper branch resonance. Comparing Figs. 4.7(a) and 4.7(b) to Fig. 4.7(c), we see that the $r = 0.45d \approx 0.051\lambda_{op}$ corner curvature lenses have a distinct upper branch resonance mode, centered at $\omega_n \approx 0.97$. To highlight the dependence of this mode on corner curvature, we separately plot transmission through the $d = \lambda_{op}/(2\sqrt{2}\pi) \approx 0.11\lambda_{op}$, $w = 3\sqrt{2}\lambda_{op} \approx 2.12\lambda_{op}$ lens for four separate corner curvatures in Fig. 4.8. Observing Figs. 4.8(a), (b), (c) and (d), we see that as corner-radius is decreased, so does the distinct upper branch resonance mode appear to shift downwards in temporal frequency along the resonance branch. Comparatively, the $r = 0.50d \approx 0.056\lambda_{op}$ lens shows this mode at $\omega_n \approx 0.96$, whereas for the $r = 0.35d \approx 0.039\lambda_{op}$ lens this mode appears at $\omega_n \approx 0.92$.

We can use these observed geometric tuning effects to suppress resonant mode amplification. In Figs. 4.9(a), 4.9(b) and 4.9(c) we plot transmission surfaces through three separate $d = \lambda_{op}/(2\sqrt{2}\pi) \approx 0.11\lambda_{op}$ single-Drude lenses geometries. For all three of these lens geometries, we examine spectral transmission along an operating frequency of $\omega_n = 0.974$. This chosen operating frequency is indicated by an overlaid dashed line on each transmission plot, and a spectral transmission cross-section along this operating frequency is plotted adjacent to each geometry in Figs. 4.9(b), 4.9(d) and 4.9(f).

Examining the Fig. 4.9 transmission plots, we see that while all three lens geometries have

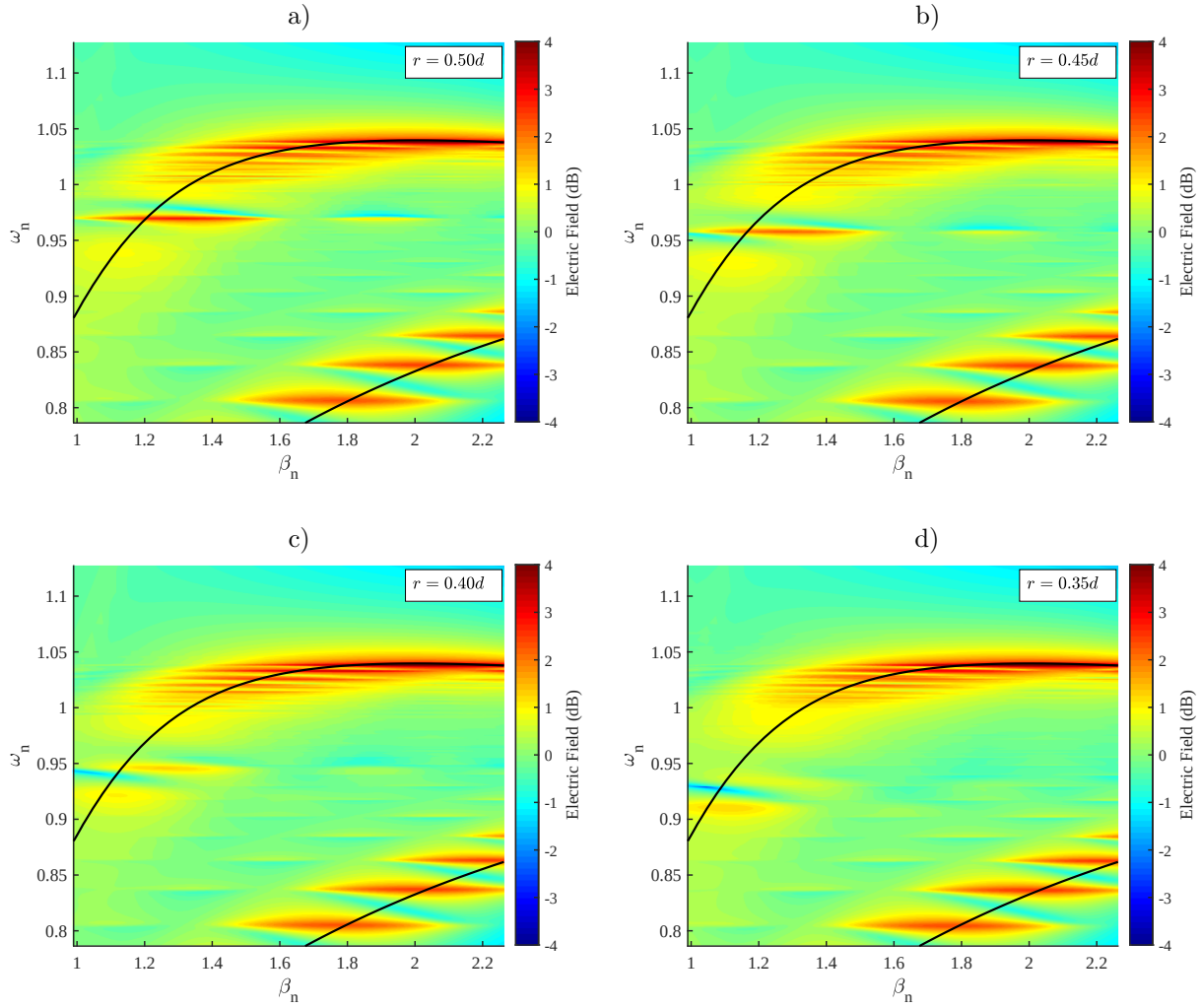

Figure 4.8: Spectral transmission plots, $\log(|T_i|)$ (dB) for $d = \lambda_{op}/(2\sqrt{2}\pi) \approx 0.11\lambda_{op}$, $w = 3\sqrt{2}\lambda_{op} \approx 2.12\lambda_{op}$ single-Drude lenses with radii of (a) $r = 0.50d \approx 0.056\lambda_{op}$, (b)$r = 0.45d \approx 0.051\lambda_{op}$, (c) $r = 0.40d \approx 0.045\lambda_{op}$, (d) $r = 0.35d \approx 0.039\lambda_{op}$.

an upper resonance branch crossing at $\omega_n = 0.974$, the resulting spectral amplification from this resonance crossing differs significantly between geometries. For the $w = 5\sqrt{2}\lambda_{op} \approx 3.53\lambda_{op}$, $r = 0.15d \approx 0.017\lambda_{op}$ lens, the operating frequency directly cross a high transmission region at $\beta_n \approx 1.2$. This generates above-unity (0 dB) amplification of spectral components between $\beta_n = 1.1$ and $\beta_n = 1.4$ as seen in Fig. 4.7(b). Increasing the radius of curvature of this lens to $r = 0.45d \approx 0.051\lambda_{op}$ in Fig 4.7(b) produces a distinct resonant mode at $\omega_n \approx 0.96$. However, despite this change in the upper branch resonance distribution, the operating frequency still intersects with the high transmission region, resulting in above-unity amplification of spectral components between $\beta_n = 1.1$ and $\beta_n = 1.4$. Finally, in Fig. 4.7(c) we reduce the width of the $r = 0.45d \approx 0.051\lambda_{op}$ lens to $w = 3\sqrt{2}\lambda_{op} \approx 2.12\lambda_{op}$. This width reduction increases the size of the low transmission region surrounding the distinct upper resonant mode at $\omega_n \approx 0.96$ such that the operating frequency no longer intersects with the high transmission region. As a result, spectral amplification between $\beta_n = 1.1$ and $\beta_n = 1.4$ is greatly reduced, as indicated by Fig. 4.9(f).

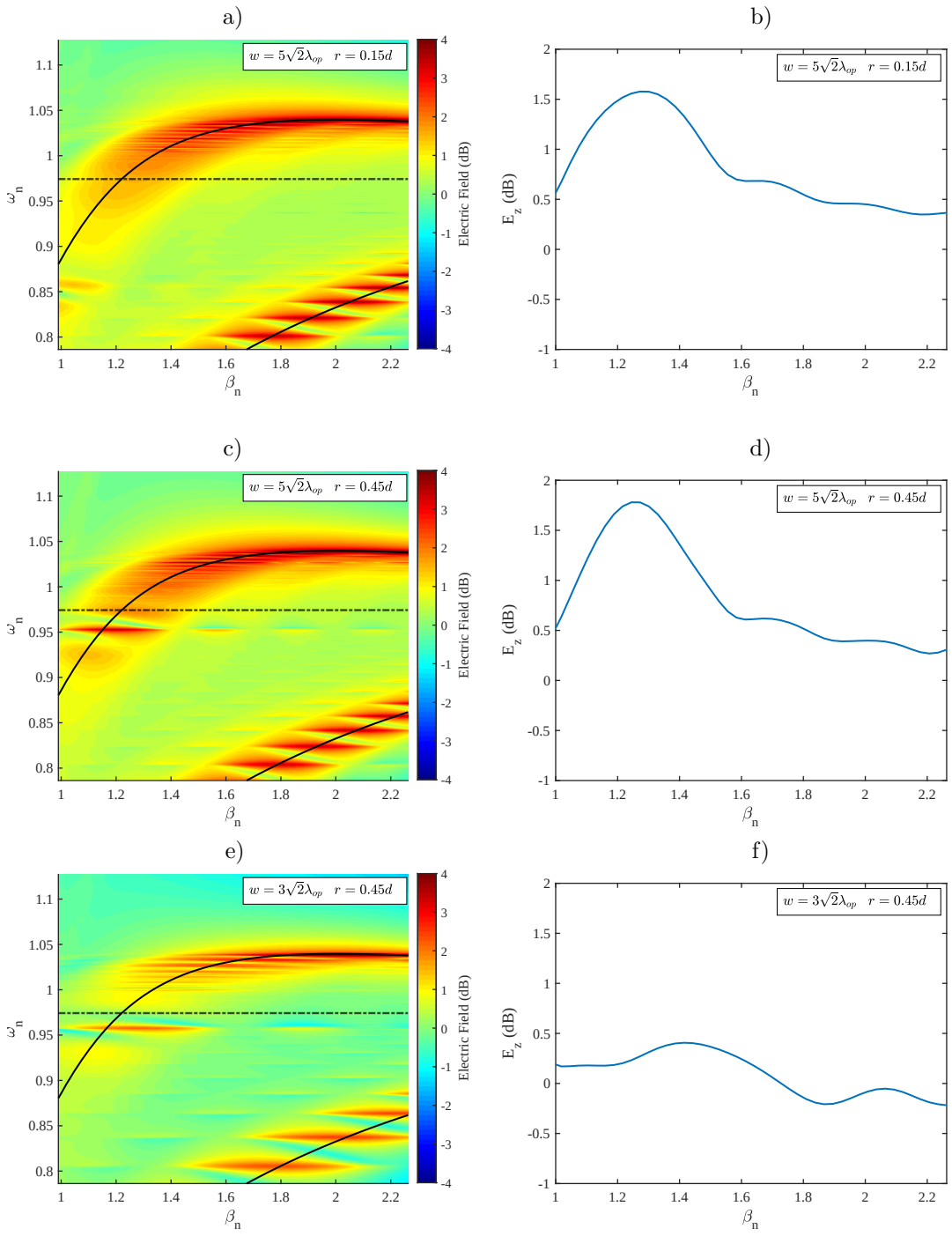

Figure 4.9: Spectral transmission plots (dB) for $d = \lambda_{op}/(2\sqrt{2}\pi) \approx 0.11\lambda_{op}$ single–Drude lenses with (a) a width of $w = 5\sqrt{2}\lambda_{op} \approx 3.53\lambda_{op}$ and corner curvature of $r = 0.15d \approx 0.017\lambda_{op}$, (c) a width of $w = 5\sqrt{2}\lambda_{op} \approx 3.53\lambda_{op}$ and corner curvature of $r = 0.45d \approx 0.051\lambda_{op}$, and (d) a width of $w = 3\sqrt{2}\lambda_{op} \approx 2.12\lambda_{op}$ and corner curvature of $r = 0.45d \approx 0.051\lambda_{op}$. The chosen operating frequency of $\omega_n = 0.974$ is plotted as an overlaid, dashed horizontal line. Spectral transmission along the operating frequency is plotted in (b) for the $w = 5\sqrt{2}\lambda_{op} \approx 3.53\lambda_{op}$, $r = 0.15d \approx 0.017\lambda_{op}$, (d) for the $w = 5\sqrt{2}\lambda_{op} \approx 3.53\lambda_{op}$, $r = 0.45d \approx 0.051\lambda_{op}$ lens, and (f) for the $w = 3\sqrt{2}\lambda_{op} \approx 2.12\lambda_{op}$, $r = 0.45d \approx 0.051\lambda_{op}$ lens.

4.3 Finite Width Lens Radiated Power Analysis

In addition to corner reflections, a finite transverse-width also introduces scattering effects. As was discussed in Sec. 2.4, surface plasmons travelling around bends can couple to free-space as propagating waves, leaking power from the lens [41]. In this section, we present a method to quantify scattering from a finite width superlens as a function of ω and β. We use this method to evaluate the geometric dependence of superlens radiation characteristics.

4.3.1 Radiated Power Methods

The power radiated by a three-dimensional object can be calculated by integrating the Poynting vector over a surface that fully encloses said object. For our two-dimensional simulation, this 2-D closed surface becomes a 1-D closed line that encircles the lens. An obvious location for this lens-encircling boundary would be along the PML interface, located at the edge of the simulation space. However, this is not the ideal boundary selection for our simulation, as along the PML interface there exist surface plasmons generated by interactions between the PML and the incident evanescent wave, the fields of which can indirectly impact the radiated power calculation by adding error to the scattered field formulation. To reduce this source of error, the lens-enclosing line is placed in between the lens and the PML boundary, providing distance for the PML surface plasmon fields to decay before reaching the radiated power calculation.

To calculate radiated power, we measure the scattered-field Poynting vector along the lens-bounding line and perform a closed-line integration of its dot product with the outward facing normal vector of the bounding curve,

$$P_{rad} = \oint_l \vec{S}\, dl \cdot \hat{n}_l. \tag{4.8}$$

Here, $\vec{S} = 0.5\,\Re\{\vec{E} \times \vec{H}^*\}$ is the real component of the scattered-field Poynting vector, and $\vec{n}_l$ is the normal vector (pointing in the outward direction) of the lens-bounding line. The result of

this integration is a scalar measure of the power radiated by the lens for excitation by a given incident spectral component.

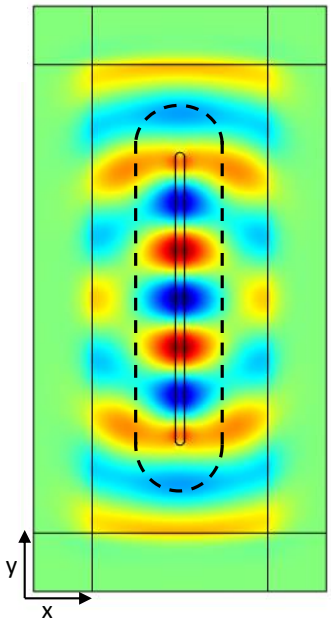

Figure 4.10: Finite width lens simulation model showing the fictitious lens-enclosing line (dashed) over which the scattered-field Poynting vector is integrated in order to calculate the power radiated by the lens.

4.3.2 Radiated Power Response

We now compare the radiated power and transmission characteristics of finite width, matched double-Drude superlenses ($\varepsilon_p = \mu_p$). In Fig. 4.11 we plot both transmission (left) and radiated power (right) surfaces for three separate $d = \lambda_{op}/(2\sqrt{2}\pi) \approx 0.11\lambda_{op}$ double-Drude lens geometries: a) $w = 3\sqrt{2}\lambda_{op} \approx 2.12\lambda_{op}$, $r = 0.45d \approx 0.051\lambda_{op}$, b) $w = 5\sqrt{2}\lambda_{op} \approx 3.53\lambda_{op}$, $r = 0.45d \approx 0.051\lambda_{op}$, and c) $w = 5\sqrt{2}\lambda_{op} \approx 3.53\lambda_{op}$, $r = 0.15d \approx 0.017\lambda_{op}$. Examining each plot, we see that radiated power manifests discrete resonant modes whose placement and appearance closely match those generated for the transmission surfaces. At resonance, surface plasmon amplitudes spike, generating strong fields that in turn radiate substantial power. Between resonances, the fields are weak, leading to low radiated power and resulting in a similar

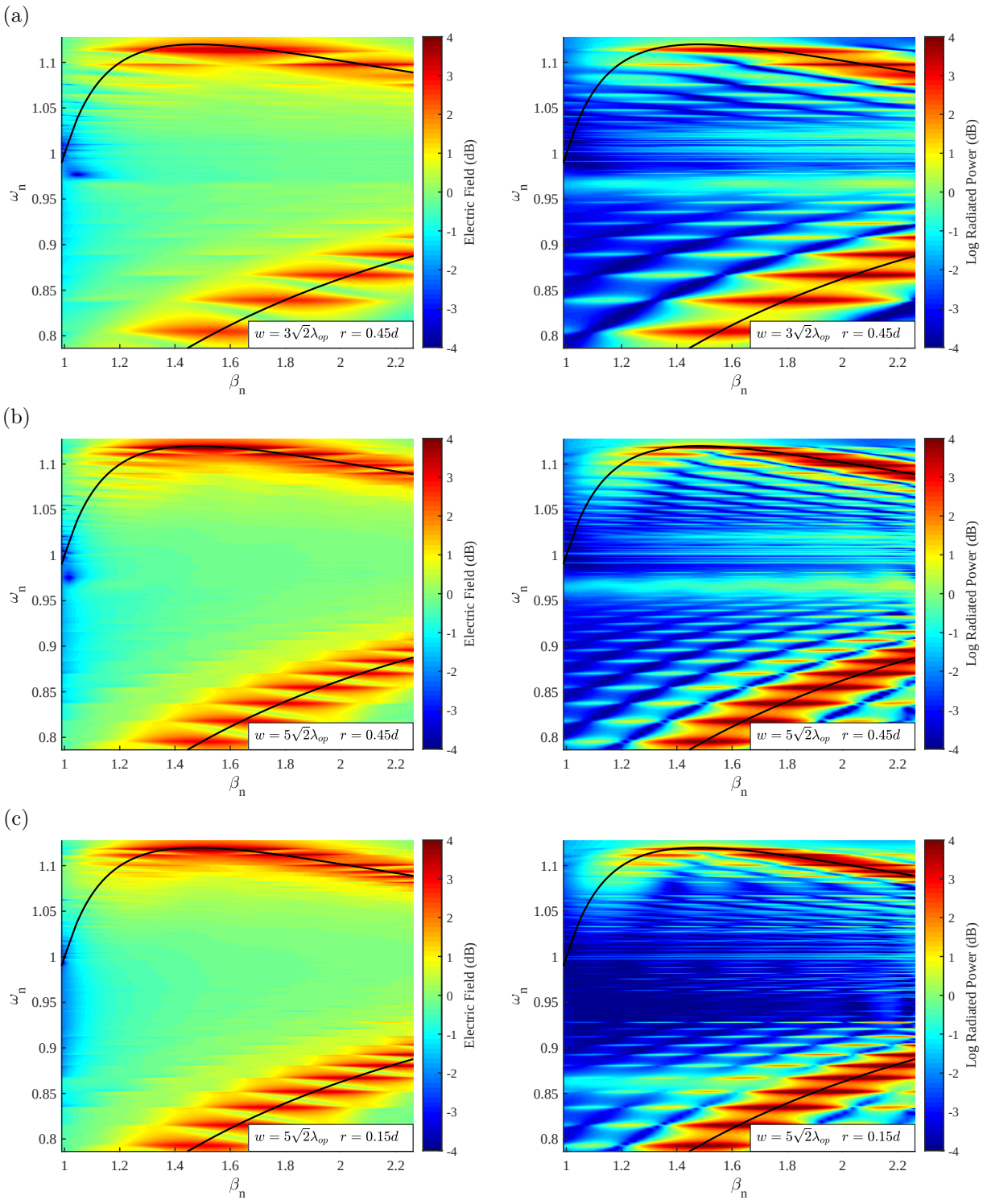

Figure 4.11: Side by side comparison of the spectral transmission, $\log(|T_i|)$ (dB, left) and radiated power, $\log(|P_{rad}|)$ (dB, right) of finite width, $d = \lambda_{op}/(2\sqrt{2}\pi) \approx 0.11\lambda_{op}$ thick matched double-Drude lenses ($\varepsilon_p = \mu_p$). Three separate lens widths and corner curvature radii combinations are considered: a) $w = 3\sqrt{2}\lambda_{op} \approx 2.12\lambda_{op}$, $r = 0.45d \approx 0.051\lambda_{op}$, b)$w = 5\sqrt{2}\lambda_{op} \approx 3.53\lambda_{op}$, $r = 0.45d \approx 0.051\lambda_{op}$ and c) $w = 5\sqrt{2}\lambda_{op} \approx 3.53\lambda_{op}$, $r = 0.15d \approx 0.017$

distribution of modes.

Examining each radiated power plot, we also see the manifestation of a high radiated power region, visible in Figs. 4.11(a), 4.11(b) and 4.11(c) as a horizontal blue/green stripe. For the $w = 3\sqrt{2}\lambda_{op} \approx 2.12\lambda_{op},\ r = 0.45d \approx 0.051\lambda_{op}$ and $w = 5\sqrt{2}\lambda_{op} \approx 3.53\lambda_{op},\ r = 0.45d \approx 0.051\lambda_{op}$ lenses, this region appears centered around $\omega_n \approx 0.96$, while it is shifted down to $\omega_n \approx 0.87$ for the $w = 5\sqrt{2}\lambda_{op} \approx 3.53\lambda_{op}$, $r = 0.15d \approx 0.017\lambda_{op}$ lens. Close examination of each corresponding transmission surface reveals similarly shaped $|T| \approx 0$ dB regions that are also visible as faint green stripes.

Let us further investigate this high transmission operating point by examining the radiated power and transmission characteristics of single-Drude lenses with varied corner-curvature. In Fig. 4.12 we plot transmission (left) and radiated power (right) surfaces for single-Drude lenses defined by a width $w = 3\sqrt{2}\lambda_{op} \approx 2.12\lambda_{op}$, thickness $d = \lambda_{op}/(2\sqrt{2}\pi) \approx 0.11\lambda_{op}$ and radii of (a) $r = 0.45d \approx 0.051\lambda_{op}$, (b) $r = 0.40d \approx 0.045\lambda_{op}$, (c) $r = 0.35d \approx 0.039\lambda_{op}$. Comparing first the Fig. 4.12(a) transmission and radiation surfaces of a $w = 3\sqrt{2}\lambda_{op} \approx 2.12\lambda_{op},\ r = 0.45d \approx 0.051\lambda_{op}$ single-Drude lens to those that were plotted for a double-Drude lens of the same geometry in Fig. 4.11(a), we see the similar manifestation of horizontally aligned high transmission/radiation region centered at $\omega_n \approx 0.97$. However, for the single-Drude case these transmission regions are not continuous, but instead appear as multiple, distinct resonant modes. This agreement in the placement of these transmission/radiation peaks indicates a strong corner-radius dependence, while variation over β indicate a material parameter/lens width dependence. Observing Fig. 4.12(a), 4.12(b) and 4.12(c) we see that as the radius of curvature is decreased, so is the position of the horizontally aligned high transmission/radiation region pushed to lower temporal frequency.

Finally, in Fig. 4.13 we compare radiated power to spectral transmission of the $+k_0$ component through a double-Drude lens. If we recall from Sec. 4.2.1, there were four main spectral components visible in the lens spectral transmission response: $\pm\beta_{ni}$ and $\pm k_0$. Comparing the

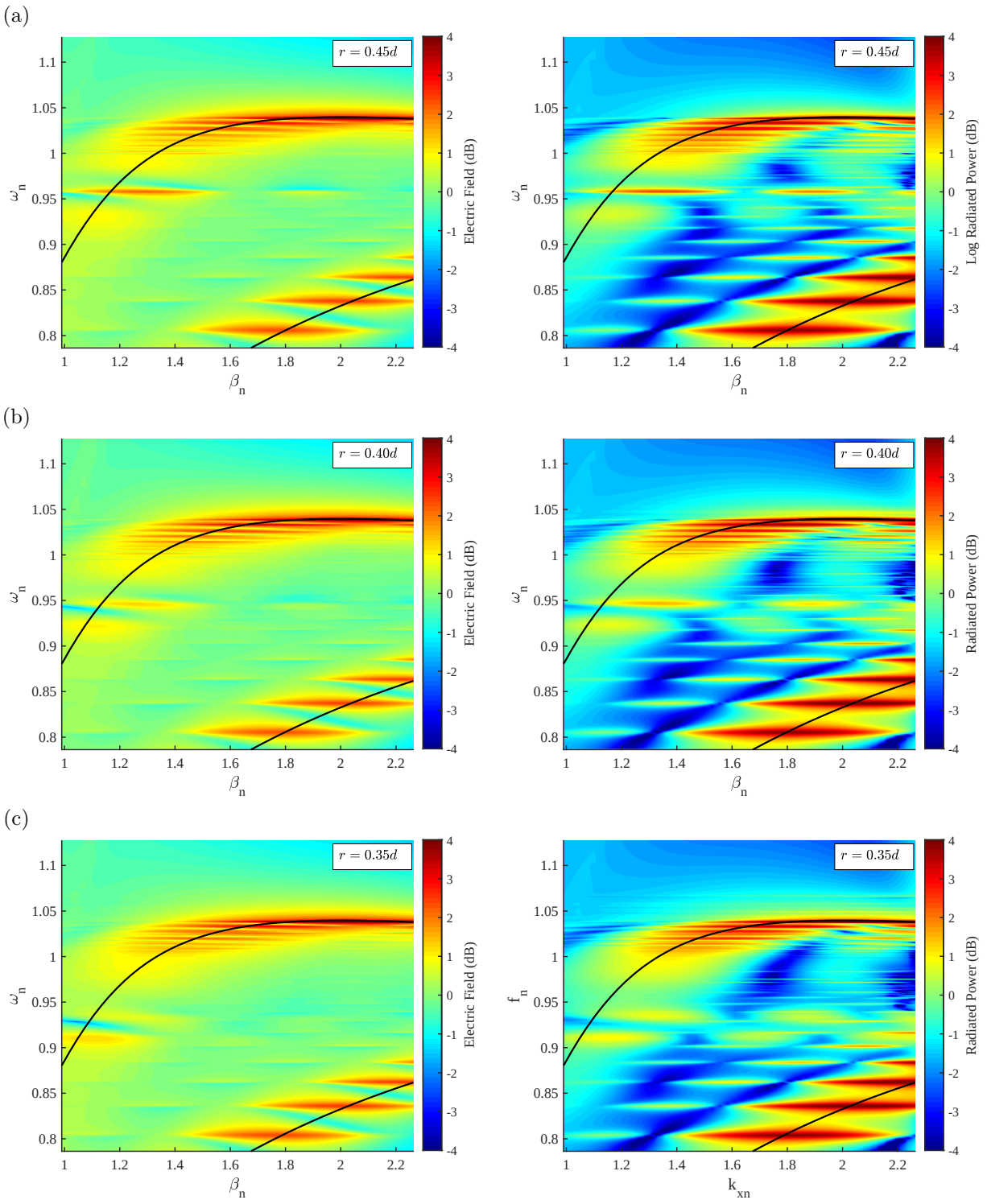

Figure 4.12: Side by side comparison of the spectral transmission, $\log(|T_i|)$ (dB, left) and radiated power, $\log(|P_{rad}|)$ (dB, right) of finite width, $d = \lambda_{op}/(2\sqrt{2}\pi) \approx 0.11\lambda_{op}$, $w = 3\sqrt{2}\lambda_{op} \approx 2.12\lambda_{op}$ single-Drude superlenses. From top to bottom results are plotted for corner radii of (a) $r = 0.45d \approx 0.051\lambda_{op}$, (b) $r = 0.40d \approx 0.045\lambda_{op}$, (c)$r = 0.35d \approx 0.039\lambda_{op}$.

transmission response of the $+k_0$ component in Fig 4.13(a) to radiated power in Fig. 4.13(b), we see that at $\omega_n \approx 0.96$ there exists a frequency band over which both transmission and radiated power are high. This indicates that the mechanism responsible for boosting radiated power along this operating frequency is connected to high amplification of the $+k_0$ spectral component.

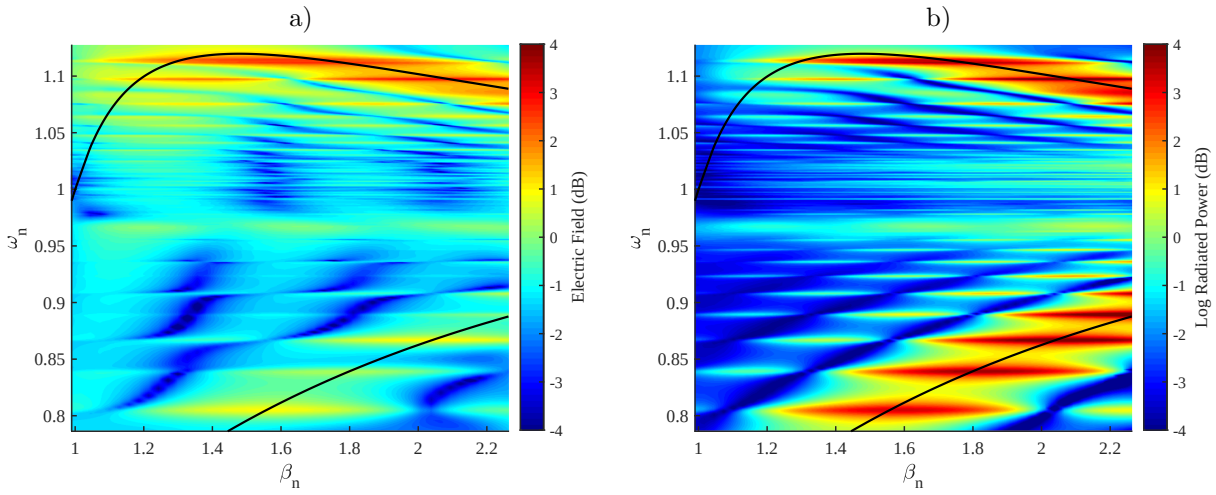

Figure 4.13: Side by side comparison of positive free-space cut-off transmission, $\log(|T_{k0}|)$ (dB, left) and radiated power, $\log(|P_{rad}|)$ (dB, right) of finite width, $d = \lambda_{op}/(2\sqrt{2}\pi) \approx 0.11\lambda_{op}$, $w = 3\sqrt{2}\lambda_{op} \approx 2.12\lambda_{op}$, $r = 0.45d \approx 0.051\lambda_{op}$ double-Drude superlenses.

Chapter 5

Conclusion

Future advancement of many contemporary light-based imaging and manufacturing techniques requires the development of lenses that are able to surpass the diffraction limit. To meet this industrial need, superlenses that are capable of generating sub-wavelength resolution images are under continued research. Superlensing relies on strong surface waves to amplify fine-detail carrying incident evanescent waves over the extent of a lens. These high surface wave amplitudes intensify minor electromagnetic interactions that are otherwise negligible in conventional lensing systems. In this thesis, we investigated two separate surface wave interaction phenomena to evaluate how they impact and may be used to enhance superlensing performance. First, we examined how near-field reflections between optical components impact imaging performance. Second, we present our method of investigating how modifying superlens width and corner radius can change the characteristics of resonant mode excitation to improve the performance of dispersive, homogeneous superlens slabs.

5.1 Summary of Evanescent Wave Simulation Guidelines

Special consideration must be given to the simulation of evanescent waves. In this thesis, evanescent wave simulation was performed using COMSOL Multiphysics' FEM-based, full-wave frequency-domain solver. An incident evanescent wave was applied in the form of a background field. As this evanescent wave was swept over a range of spatial and temporal frequencies, the exponential decay was spatially offset to ensure that all spectral components would have unity amplitude at the first lens interface. A simulation-space bounding PML was employed to absorb scattered radiation. To eliminate interactions between the incident evanescent wave and this PML, a total-field scattered-field formulation was used. Numerical noise

introduced by the subtraction of high background evanescent fields from the total field was minimized by carefully positioning the simulation-bounding PML. The PML had to be placed far enough away from the lens to limit interactions with scattered evanescent waves, while still being close enough to reduce the backward amplification of incident evanescent waves, and thereby minimize numerical noise generated by the scattered-field subtraction. Radiated power was calculated by integrating the scattered-field Poynting vector over a lens-enclosing line. This integration boundary was carefully placed between the lens and the PML in order to minimize numerical noise from high, non-radiative fields along the integration boundary. Despite these precautions, an upper transverse spatial frequency limit of $\beta_n = 2.27$ was still required, as the dynamic range of higher transverse spatial frequency components introduced excessive numerical noise to the simulation.

5.2 Summary of Research

To evaluate how near-field interactions between imaging components can affect superlensing performance, we studied transmission through a complete superlensing system. Using a 1-D imaging model to facilitate our analysis, we centered an SNG slab superlens between matched dielectric object and detector half-spaces, and evaluated spectral transmission over a range of lens thicknesses and imaging distances. Our multi-layer system transmission analysis revealed major differences in the transmission responses of ENG and MNG lenses. The MNG lens displayed a greatly improved transmission response when object-detector interactions were accounted for, maintaining higher, more uniform evanescent wave transmission over longer imaging distances.

We hypothesized this improved transmission response to be a result of a secondary mechanism for evanescent wave amplification outside the lens within the object-lens free-space cavity. To isolate the effect of this resonance from the internal resonance of the slab, we examined a three layer system consisting of a dielectric half-space and SNG half-space separated by a

free-space gap. The transmission response of this three-layer system supported our hypothesis, revealing a polarization dependent resonance condition whose additional amplification could predict the amplification observed in our 1-D imaging system response. To complete the study, we performed an imaging analysis to compare lossy ENG and MNG lensing performance. Our results showed that an MNG lens within a dielectric imaging system has the most reliable imaging performance, being able to resolve a three point source object field with a sub-wavelength adjacent peak separation distance of 0.25λ for loss tangents below 0.15. These results indicate that object-detector interactions are not necessarily deleterious to lensing, but can in fact improve imaging performance and robustness to loss by generating a secondary amplification mechanism in the form of an external resonance.

We then investigated the impact that surface wave interactions with finite transverse-width superlens geometry have on lensing performance. We developed a method to evaluate the frequency characteristics of finite transverse width superlenses with respect to incident evanescent plane waves of different transverse wave numbers. This was done using a full-wave simulation package supplied by COMSOL multiphysics. Our 2-D lensing model consisted of a suplerlens slab with finite thickness and finite width placed within free-space, and surrounded on all sides by a PML to absorb scattered radiation. The lens was excited by a monochromatic plane wave whose frequency and transverse wave number were swept over the evanescent regime.

To characterize superlens responses, we first examined spectral transmission through various lens geometries. For each incident Fourier component, the scattered electric field was measured along the image plane, then converted to the spectral domain using an FFT. The spectral response of the lens showed the primary transmission of the incident component, with significant spectral peaks located at $\pm k_0$ and $-\beta_{ni}$. We demonstrated how the majority of the transmission spectrum could be captured by decomposing the lens response into a superposition of these four main spectral peaks. We then focused on transmission of the $+\beta_{ni}$ component, using Fourier modelling of the lens response to simplify analysis by extracting a single

coefficient approximating its transmission.

Our generated incident spectral component transmission plots displayed discrete resonant modes that closely followed the upper and lower branch dispersion solutions for an infinitely wide superlens. Increasing lens width increased the density of resonant modes distributed along the dispersion solutions in a manner consistent with the one dimensional cavity model. Changing lens corner curvature radius shifted the position of resonant modes, the modal placement of lenses having larger corner radii being more consistent with a shorter effective one-dimensional cavity length. By varying lens width and corner geometry, we demonstrated how an operating frequency could be centered between resonant modes to reduce above-unity spectral amplification at resonance.

Finally, by integrating the Poynting vector over a lens-encircling line, we evaluated the power radiated by various superlens geometries. These radiated power plots proved consistent with the prior generated transmission plots. The high fields generated by strong surface waves at resonance were found to radiate substantial power, resulting resonant dispersion curves that closely matched those of the transmission plots. The radiated power plots highlighted a corner curvature dependent high field operating frequency that was consistent with high transmission of non-incident spectral components.

5.3 Future Work

The work described in Chapter 3 of this thesis has laid a good foundation for the future study of external resonance in superlensing systems. Integration of the described resonant amplification mechanism with other loss compensation techniques should be investigated to further reduce the impact of lens loss on imaging performance. In light of this work, the analysis of superlens designs within complete imaging systems should consider how object-detector interactions might be used to boost imaging performance. Multi-layer lens designs with alternating lens-air-dielectric layers could also be investigated to further improve the overall amplification of

incident evanescent components.

The work described in Chapter 4 of this thesis has raised a number of questions regarding superlens performance improvement through geometric tuning. The temporal and spatial frequency dependence of specific upper resonant modes on lens curvature radius was demonstrated to be a useful parameter for avoiding the above-unity amplification of resonant Fourier components. To provide a better understanding of this phenomenon, its underlying mechanism should be explored. The 1-D cavity model that was used to predict finite-width superlens resonance should be expanded so that it accounts for corner curvature radius to provide a more complete model. Finally, the methods described in this thesis should be applied to more complicated lens models to evaluate how geometric tuning could improve the response of contemporary superlens designs.

Bibliography

[1] T. Araki, "The history of optical microscope," *Mechanical Engineering Reviews*, vol. 4, no. 1, pp. 16–00242, 2017.

[2] B. Vohnsen, "A short history of optics," *Physica Scripta*, vol. 2004, no. T109, p. 75, 2004.

[3] G. B. Airy, "On the diffraction of an object-glass with circular aperture," *Transactions of the Cambridge Philosophical Society*, vol. 5, p. 283, 1835.

[4] E. Abbe, "Beiträge zur theorie des mikroskops und der mikroskopischen wahrnehmung," *Archiv für mikroskopische Anatomie*, vol. 9, pp. 413–418, Dec 1873.

[5] E. Synge, "Xxxviii. a suggested method for extending microscopic resolution into the ultra-microscopic region," *The London, Edinburgh, and Dublin Philosophical Magazine and Journal of Science*, vol. 6, no. 35, pp. 356–362, 1928.

[6] W. Adams, M. Sadatgol, and D. Ö. Güney, "Review of near-field optics and superlenses for sub-diffraction-limited nano-imaging," *AIP Advances*, vol. 6, no. 10, p. 100701, 2016.

[7] S. C. Kehr, Y. M. Liu, L. Martin, P. Yu, M. Gajek, S.-Y. Yang, C.-H. Yang, M. Wenzel, R. Jacob, H.-G. Von Ribbeck, *et al.*, "Near-field examination of perovskite-based superlenses and superlens-enhanced probe-object coupling," *Nature communications*, vol. 2, no. 1, pp. 1–9, 2011.

[8] T. Taubner, D. Korobkin, Y. Urzhumov, G. Shvets, and R. Hillenbrand, "Near-field microscopy through a sic superlens," *Science*, vol. 313, no. 5793, pp. 1595–1595, 2006.

[9] J. B. Pendry, "Negative refraction makes a perfect lens," *Physical review letters*, vol. 85, no. 18, p. 3966, 2000.

[10] V. G. Veselago, "The electrodynamics of substances with simultaneous negative values of permitivitty and permeability," *SOV PHYS USPEKHI*, vol. 10, pp. 509–514, 1968.

[11] R. Collin, "Frequency dispersion limits resolution in veselago lens," *Progress in Electromagnetics Research B*, vol. 19, pp. 233–261, 01 2010.

[12] V. A. Podolskiy and E. E. Narimanov, "Near-sighted superlens," *Optics letters*, vol. 30, no. 1, pp. 75–77, 2005.

[13] S. Linden, C. Enkrich, M. Wegener, J. Zhou, T. Koschny, and C. M. Soukoulis, "Magnetic response of metamaterials at 100 terahertz," *Science*, vol. 306, no. 5700, pp. 1351–1353, 2004.

[14] W. S. Hart, A. O. Bak, and C. C. Phillips, "Ultra low-loss super-resolution with extremely anisotropic semiconductor metamaterials," *AIP Advances*, vol. 8, no. 2, p. 025203, 2018.

[15] S. M. Rudolph, C. Pfeiffer, and A. Grbic, "Design and free-space measurements of broadband, low-loss negative-permeability and negative-index media," *IEEE Transactions on Antennas and Propagation*, vol. 59, no. 8, pp. 2989–2997, 2011.

[16] C. Scarborough, Z. Jiang, D. H. Werner, C. Rivero-Baleine, and C. Drake, "Experimental demonstration of an isotropic metamaterial super lens with negative unity permeability at 8.5 mhz," *Applied Physics Letters*, vol. 101, no. 1, p. 014101, 2012.

[17] M. A. Panah, O. Takayama, S. Morozov, K. Kudryavtsev, E. Semenova, and A. Lavrinenko, "Highly doped inp as a low loss plasmonic material for mid-ir region," *Optics express*, vol. 24, no. 25, pp. 29077–29088, 2016.

[18] D. Ye, B. Li, Z. Zhu, Y. Yang, and Z. Wang, "Achieving volumetric gain metamaterials," *AIP Advances*, vol. 9, no. 5, p. 055314, 2019.

[19] Y. T. Wang, B. H. Cheng, Y. Z. Ho, Y.-C. Lan, P.-G. Luan, and D. P. Tsai, "Gain-assisted hybrid-superlens hyperlens for nano imaging," *Optics express*, vol. 20, no. 20, pp. 22953–22960, 2012.

[20] S. A. Ramakrishna and J. B. Pendry, "Removal of absorption and increase in resolution in a near-field lens via optical gain," *Physical Review B*, vol. 67, no. 20, p. 201101, 2003.

[21] M. P. H. Andresen, A. V. Skaldebø, M. W. Haakestad, H. E. Krogstad, and J. Skaar, "Effect of gain saturation in a gain compensated perfect lens," *JOSA B*, vol. 27, no. 8, pp. 1610–1616, 2010.

[22] M. Sadatgol, Ş. K. Özdemir, L. Yang, and D. Ö. Güney, "Plasmon injection to compensate and control losses in negative index metamaterials," *Physical review letters*, vol. 115, no. 3, p. 035502, 2015.

[23] W. Adams, A. Ghoshroy, and D. O. Güney, "Plasmonic superlens image reconstruction using intensity data and equivalence to structured light illumination for compensation of losses," *J. Opt. Soc. Am. B*, vol. 34, pp. 2161–2168, Oct 2017.

[24] W. Du, W. Kong, H. Liu, K. Liu, C. Wang, and X. Luo, "Design of a structured bulk plasmon illumination source for enhancing plasmonic cavity superlens imaging," *Plasmonics*, vol. 13, 08 2017.

[25] D. O. Melville and R. J. Blaikie, "Super-resolution imaging through a planar silver layer," *Optics express*, vol. 13, no. 6, pp. 2127–2134, 2005.

[26] N. Fang, H. Lee, C. Sun, and X. Zhang, "Sub–diffraction-limited optical imaging with a silver superlens," *Science*, vol. 308, no. 5721, pp. 534–537, 2005.

[27] A. Pimpin and W. Srituravanich, "Review on micro-and nanolithography techniques and their applications," *Engineering Journal*, vol. 16, no. 1, pp. 37–56, 2012.

[28] F. Wang, L. Liu, H. Yu, Y. Wen, P. Yu, Z. Liu, Y. Wang, and W. J. Li, "Scanning superlens microscopy for non-invasive large field-of-view visible light nanoscale imaging," *Nature communications*, vol. 7, no. 1, pp. 1–10, 2016.

[29] P. Weber, M. Wagner, and H. Schneckenburger, "Fluorescence imaging of membrane dynamics in living cells," *Journal of biomedical optics*, vol. 15, no. 4, p. 046017, 2010.

[30] M. F. Shirazi, K. Park, R. E. Wijesinghe, H. Jeong, S. Han, P. Kim, M. Jeon, and J. Kim, "Fast industrial inspection of optical thin film using optical coherence tomography," *Sensors*, vol. 16, no. 10, p. 1598, 2016.

[31] L. Fu, K. Frenner, H. Li, and W. Osten, "A silicon superlens with a simple design working at visible wavelengths," in *Optical Micro-and Nanometrology VI*, vol. 9890, p. 98900I, International Society for Optics and Photonics, 2016.

[32] L. Chen, S. He, and L. Shen, "Finite-size effects of a left-handed material slab on the image quality," *Physical review letters*, vol. 92, no. 10, p. 107404, 2004.

[33] Y. Zhao, P. Belov, and Y. Hao, "Accurate modeling of the optical properties of left-handed media using a finite-difference time-domain method," *Physical Review E*, vol. 75, no. 3, p. 037602, 2007.

[34] D. L. Sounas, N. V. Kantartzis, and T. D. Tsiboukis, "Temporal characteristics of resonant surface polaritons in superlensing planar double-negative slabs: Development of analytical schemes and numerical models," *Physical Review E*, vol. 76, no. 4, p. 046606, 2007.

[35] D. R. Smith, W. J. Padilla, D. Vier, S. C. Nemat-Nasser, and S. Schultz, "Composite medium with simultaneously negative permeability and permittivity," *Physical review letters*, vol. 84, no. 18, p. 4184, 2000.

[36] W. Rotman, "Plasma simulation by artificial dielectrics and parallel-plate media," *IRE Transactions on Antennas and Propagation*, vol. 10, no. 1, pp. 82–95, 1962.

[37] J. B. Pendry, A. J. Holden, D. J. Robbins, and W. Stewart, "Magnetism from conductors and enhanced nonlinear phenomena," *IEEE transactions on microwave theory and*

techniques, vol. 47, no. 11, pp. 2075–2084, 1999.

[38] R. Ruppin, "Surface polaritons of a left-handed material slab," *Journal of Physics: Condensed Matter*, vol. 13, no. 9, p. 1811, 2001.

[39] I. Aghanejad, K. J. Chau, and L. Markley, "Avoiding imaging artifacts from resonant modes in metamaterial superlenses," *Physical Review B*, vol. 100, no. 3, p. 035137, 2019.

[40] K. Hasegawa, J. U. Nöckel, and M. Deutsch, "Surface plasmon polariton propagation around bends at a metal–dielectric interface," *Applied physics letters*, vol. 84, no. 11, pp. 1835–1837, 2004.

[41] K. Hasegawa, J. U. Nöckel, and M. Deutsch, "Curvature-induced radiation of surface plasmon polaritons propagating around bends," *Physical Review A*, vol. 75, no. 6, p. 063816, 2007.

[42] M. Ahmadi, K. Forooraghi, R. Faraji-Dana, and M. Ghaffari-Miab, "Two-dimensional sub-diffraction-limited imaging by an optimized multilayer superlens," *Journal of the Optical Society of Korea*, vol. 20, no. 6, pp. 653–662, 2016.

[43] J. Ma and K. Yuan, "Optimum structure of multi-layer silver superlenses for optical lithography," in *Proceedings of the 2nd International Conference on Computer Science and Electronics Engineering*, pp. 1318–1321, Atlantis Press, 2013.

[44] C. P. Moore, M. D. Arnold, P. J. Bones, and R. J. Blaikie, "Image fidelity for single-layer and multi-layer silver superlenses," *JOSA A*, vol. 25, no. 4, pp. 911–918, 2008.

[45] S. A. Ramakrishna, J. Pendry, M. Wiltshire, and W. Stewart, "Imaging the near field," *Journal of Modern Optics*, vol. 50, no. 9, pp. 1419–1430, 2003.

[46] E. Shamonina, V. A. Kalinin, K. H. Ringhofer, and L. Solymar, "Imaging, compression and poynting vector streamlines for negative permittivity materials," *Electronics Letters*, vol. 37, pp. 1243–1244, Sep. 2001.

[47] S. A. Ramakrishna, J. B. Pendry, M. C. K. Wiltshire, and W. J. Stewart, "Imaging the near field," *Journal of Modern Optics*, vol. 50, no. 9, pp. 1419–1430, 2003.

[48] J. T. Shen and P. M. Platzman, "Near field imaging with negative dielectric constant lenses," *Applied Physics Letters*, vol. 80, no. 18, pp. 3286–3288, 2002.

[49] W. T. Lu and S. Sridhar, "Near-field imaging by negative permittivity media," *Microwave and Optical Technology Letters*, vol. 39, no. 4, pp. 282–286, 2003.

[50] D. O. S. Melville, R. J. Blaikie, and C. R. Wolf, "Submicron imaging with a planar silver lens," *Applied Physics Letters*, vol. 84, no. 22, pp. 4403–4405, 2004.

[51] N. Fang, H. Lee, C. Sun, and X. Zhang, "Sub-diffraction-limited optical imaging with a silver superlens," *Science*, vol. 308, no. 5721, pp. 534–537, 2005.

[52] P. A. Belov and Y. Hao, "Subwavelength imaging at optical frequencies using a transmission device formed by a periodic layered metal-dielectric structure operating in the canalization regime," *Phys. Rev. B*, vol. 73, p. 113110, Mar 2006.

[53] M. J. Freire, R. Marques, and L. Jelinek, "Experimental demonstration of a $\mu = -1$ metamaterial lens for magnetic resonance imaging," *Applied Physics Letters*, vol. 93, no. 23, p. 231108, 2008.

[54] A. Grbic and G. V. Eleftheriades, "Overcoming the diffraction limit with a planar left-handed transmission-line lens," *Phys. Rev. Lett.*, vol. 92, p. 117403, Mar 2004.

[55] S. J. Mason, "Feedback theory-further properties of signal flow graphs," *Proceedings of the IRE*, vol. 44, pp. 920–926, July 1956.

[56] E. Shamonina and L. Solymar, *Waves in Metamaterials*. Oxford University Press, 2009.

[57] T. Xu, A. Agrawal, M. Abashin, K. J. Chau, and H. J. Lezec, "All-angle negative refraction and active flat lensing of ultraviolet light," *Nature*, vol. 497, no. 7450, pp. 470–474,

2013.

[58] E. Simoncelli and N. Daw, “Least squares optimization,” *Lecture Notes, http://www. cns. nyu. edu/eero/teaching. html*, 2003.